UNIVERSITY OF CALIFORNIA, SAN DIEGO

From Nanoparticles to Non-Covalent Interactions: Electron Transfer in Inorganic Supramolecular Mixed Valence Systems

A dissertation submitted in partial satisfaction of the requirements for the degree of

Doctor of Philosophy

in

Chemistry

by

Gabriele Canzi

Committee in charge:

Professor Clifford P. Kubiak, Chair
Professor Joseph M. O'Connor
Professor Kimberly A. Prather
Professor Michael J. Tauber
Professor Joseph Wang

2014

The dissertation of Gabriele Canzi is approved, and it is acceptable in quality and form for publication on microfilm.

Chair

University of California, San Diego

2014

DEDICATION

to my parents, Patrizia and Adriano

for their unconditional love and admirable courage

to my sister for her wisdom and patience

to my friends for making this journey fun and worthwhile

EPIGRAPH

There is no supermarket where you can buy determination:

either you have it or you don't.

Marco Pantani

TABLE OF CONTENTS

LIST OF FIGURES

LIST OF TABLES

ACKNOWLEDGEMENTS

I'm not known as a great communicator, therefore I don't think I have ever taken the opportunity to personally thank the people responsible for helping me making it this far. There are so many individuals that were involved in this journey, and I am thankful for each and every one of you.

Cliff, what can I say about Cliff that is not already known? I will be forever indebted to him not only for taking a chance and believing in me, but also for allowing me to forge my own path during my graduate studies. This thesis would have not been completed without his input and ideas. Cliff is a great person to work for and a great person to have a beer and share stories with. I have never met someone as passionate and knowledgeable about chemistry as Cliff, and I thank you for sharing with me some of that knowledge and instilling confidence in me and my abilities by respecting me as a scientist. Cliff gave me the freedom to be myself and fail on my own terms during grad school, but most importantly though, he taught me to always be ready and have a plan B because you don't know what life will throw at you next.

Thank you to all of the great people I was fortunate enough to work with. To my labmates, I will always remember each and every one of you for all the good times and great memories. I know that the experience I've had in the Kubiak lab will never be duplicated. Jesse, you are very much like a big brother to me, and I thank you for your drive and attention to detail in every aspect of research, I strive to be more like you in the workplace. Mike, you are a friend that I will miss dearly once I leave the Kubiak family, you have shown me to never give up and be honest and genuine. And I almost forgot, you

taught me that cone angles affect energetics. Matt, although you are quiet you have the work ethic and determination of a true leader. I know that you'll be extremely successful in your every endeavor. I truly enjoyed our time working together. I will miss fighting for the bear with you. Jane, thank you for your honesty and help throughout the time we've worked and lived together. You have pushed me to be a better individual and a better scientist. I could not be here if it wasn't for the Kubiak lab members that I worked with in the beginning of this adventure. Thank you Candace for being the kindest person I've ever worked with. Thank you for your generosity and quiet leadership. Eric, with you I was able to experience many great bike rides, and a common love for music. You taught me that you can learn a lot more from working in lab than from a book. Smeej, I am so happy to have met you and to have been able to work with you. We shared a lot of good times together. I think you are an extremely kind man and talented scientist. To the two individuals that taught me everything I know in lab. Goeltz and Starla. There are no words to describe the gratitude I have for you both. I am so proud to be and have been a member of Team Self Exchange. You welcomed me in the lab with open arms and I will never forget that. Goeltz, you are the smartest person I have even known. I was in constant awe everytime we exchanged ideas. I will be forever indebted to what you were able to teach me. You made work harder than ever to strive to have the same impact as you had in the Kubiak lab. Starla, Thank you, thank you, thank you, for all that you did for me. You probably helped me more in my personal life than in lab. And you really helped me a lot in lab. You are the most positive and energetic person I've ever met in my life. My graduate school experience would have been a lot less fun and fulfilling had I

not worked alongside you. Thank you from the bottom of my heart for everything, I look forward to continuing our amazing friendship.

Thank you to the three undergrads that I've been so fortunate to work with. I was supposed to mentor you, but I probably learned as much from you as you did from me. Roger, you reinstalled a love for music and metal that I hadn't had since my high school days. You single handedly pushed me to care less about what others think and to just be myself. I thank you so much for showing me that. Chiara, you are like a little sister to me. Having met you when you were just 17 and now you are in medical school, it makes me so proud so have contributed to your success. You really showed me what determination means and achieving what seems impossible from the start. David, with you I've been able to share two of my passions, chemistry and cycling. I am and always will be thankful for the time we've had working together. I think you'll do great at anything you'll set your mind to.

Thank you to my best friend in San Diego, Travis. You are the most intriguing and charismatic person I know. From the first day that we've met, we've clicked. You started a business from scratch when everyone was telling you how crazy of an idea that was and you made it work. It worked because of you and your personality. I am thankful I was part of the beginnings of the Secret Cookie Service, and thankful to be your friend and partner in crime.

Thank you to Austin (my twin brother), Rick, Enak, Chino, Ale, Viva, Mayra and all my friends in LA and those from LMU. I will always cherish our friendship. Austin, you deserve a special mention for what our friendship has meant to me all these years. I really do think of you as a brother and I cannot imagine what my life would be like have I

had not met you. Thank you to the best coach I've ever had. Coach Rapp, you have been incredible in shaping me as man and as a player. You have incredible compassion and I will always be thankful for the opportunities you gave me, even when I might have not deserved them. You are truly an inspiration for me and for the thousands of players you have coached and mentored throughout the years. I would also like to thank my friend and guitar teacher Warren. Despite our age difference, I consider you a good friend and you have taught me a lot more than just how to play a guitar.

To my family in Milan, thank you for all the love throughout the years and I hope to have made everyone proud. I cannot be forget to mention my dearest friend Stefano G. We have shared the best friendship anyone can ask for since elementary school. The experiences we've had together will always be with me. I am thankful that I was able to race bikes with you and I am really fortunate to have you as my friend when I crashed and you had to pick me up from the hospital and babysit me for a week. To Stefano L., Leo, Gianluca, and all the rest of my Italian friends, you are far away but everytime we see each other it is as if I had never left.

As silly as it may sound, I would like to take the time to thank Ernesto Colnago and the Wilier company for making the greatest bicycles in the world. Without my EPS and Zero.7 graduate school would have been very different, because my bicycles helped me enjoy even the darkest days of my graduate career.

To Katherine, very few people in the world know me and understand me the way you do. You love me for who I am and you have not tried to change me one bit. You have given me unflappable support from day 1 and I thank you for that. There are not enough

words to describe my love and appreciation for you. Although we enter a chapter of our lives with a lot of unknowns I know this, I have never loved someone like I do love you.

I cannot write this without thanking my sister, Chiara. She's the best sister I've ever had, and the best anyone could ask for. You somehow managed to put up with me picking on you all these years. You have always given me the best support through the good and the bad times. You're my voice of reason and the first person I consult for any advice.

Finally, I would like to thank my parents. Thank you for your unwavering love, support, and courage. Thank you for giving me the opportunities that I have been so fortunate to have. Thank you for allowing me to find my way and giving me the freedom to learn from my mistakes and have the experiences that I've had in my life. This dissertation is just as much your doing as it is mine. You are my idols, my best friends, and words are not enough to describe the immense gratitude I feel today. I strive everyday to make you even a little bit as proud as I am proud to be your son. For all you have done for me, all I can say is GRAZIE e sopratutto grazie per avermi fatto interista!

SPECIFIC CHAPTER ACKNOWLEDGMENTS

Chapter 2: Much of the material for this chapter comes directly from a manuscript entitled “Mixed Valence Nanoclusters: Fast Electron Transfer in Mixed Valence Systems with a Gold Nanoparticle as the Bridge” by Gabriele Canzi and Clifford P. Kubiak, which has been published in *Small*, **2011**, *7* (14), 1967-1971. DOI: 10.1002/smll.201100483 The dissertation author is the primary author of this manuscript.

Chapter 3: Much of the material for this chapter comes directly from a manuscript entitled “Ultrafast Electron Transfer Across a Gold Nanoparticle: Ancillary Ligand and Solvent Influences” by Gabriele Canzi and Clifford P. Kubiak, which has been published in *Journal of Physical Chemistry C,* **2012**, *116* (11), 6560-6566. The dissertation author is the primary author of this manuscript.

Chapter 4: Much of the material for this chapter comes directly from a manuscript entitled “Controlling the Rate of Electron Transfer Between QDs and Ru3O Clusters by Tuning the Chemistry of the Interface” by Adam J. Morris-Cohen, Kenneth O. Aruda, Andrew M. Rasmussen, Gabriele Canzi, Tamar Seideman, Clifford P. Kubiak, and Emily A. Weiss which has been published in *Physical Chemistry Chemical Physics* ***2012***, 14, pp.13794-13801 The dissertation author is a contributing author of this manuscript.

Chapter 5: Much of the material for this chapter comes directly from a manuscript entitled “On the Observation of Intervalence Charge Transfer Bands in Hydrogen-Bonded Mixed-Valence Complexes” by Gabriele Canzi, John C. Goeltz, Jane S. Henderson, Roger E. Park, Chiara Maruggi, and Clifford P. Kubiak, which has been published in *Journal of the American Chemical Society,* **2014**, *136* (5), 1710-1713. The dissertation author is the primary author of this manuscript.

Chapter 6: Much of the material for this chapter comes directly from a manuscript in preparation entitled: "Spectroscopic and Electrochemical Studies of Ru_3O clusters with

π-stacking ligands" by Gabriele Canzi, David Ung, and Clifford P. Kubiak. The dissertation author is the primary author of this manuscript.

Chapter 7: Much of the material for this chapter comes directly from a manuscript entitled “Diffusion-Ordered NMR Spectroscopy as a Reliable Alternative to TEM for Determining the size of Gold Nanoparticles in Organic Solution” by Gabriele Canzi, Anthony A. Mrse, and Clifford P. Kubiak, which has been published in *Journal of Physical Chemistry C,* **2011**, *115* (16), 7972-7978. The dissertation author is the primary author of this manuscript.

VITA

2008 Bachelor of Science, Loyola Marymount University

2010 Master of Science, University of California, San Diego

2014 Doctor of Philosophy, University of California, San Diego

PUBLICATIONS

Canzi, G., Goeltz, J.C., Henderson, J.S., Park, R.E., Maruggi, C., Kubiak, C. P. "On the observation of intervalence charge transfer (IVCT) bands in hydrogen-bonded mixed valence complexes." *J. Am. Chem. Soc.* **2014**,*136(5),* 1710-1713

Garcia, M., Aguirre M.J., Canzi G**.,** Kubiak C.P., Isaacs M. "Electro and Photoelectrochemical reduction of carbon dioxide on multimetallic Porphyrins/Polyoxotungstate modified electrodes" *Electrochim. Acta,* **2014,** *115,* 146-154

Morris-Cohen, A.J., Aruda, K.O., Rasmussen, A., Canzi, G., Seidemann, T., Kubiak, C.P., Weiss, E.A. "Controlling the rate of electron transfer between a quantum dot and a tri-ruthenium molecular cluster by tuning the chemistry of the interface." *Phys. Chem. Chem. Phys*., **2012**, *14*, 13794-13801

Canzi, G., Kubiak, C.P. "Ultrafast electron transfer across a gold nanoparticle: A study of ancillary ligand and solvent influences."*J. Phys. Chem. C* , **2012**, *166(11),* 6560-6566.

Canzi, G., Kubiak, C.P. "Mixed valence nanoclusters: Fast electron transfer in mixed-valence systems with a gold nanoparticle as the bridge." *Small ,* **2011**, *7* (14), 1967-1971

Canzi, G., Mrse, A.A., Kubiak, C.P. "Diffusion-ordered NMR spectroscopy as a reliable alternative to TEM for determining the size of gold nanoparticles in organic solutions." *J. Phys. Chem. C* , **2011**, *115(16),* 7972-7978.

Baumgart, P., Canzi, G., Hanashiro, T., Doezema, L.A., Siniawski, M.T. "Influence of fatty acid additives on the tribological performance of sunflower oil" *Lubrication Science*, **2010**, 22 (9), 393-403

Doezema, L.A., Bigley, C., Canzi, G., Chang, K., Hirning, A.J., Lee, J., Von der Ahe N. “The influence of sampling protocol on nonmethane hydrocarbon mixing ratios.” *Atmospheric Environment*, **2010**, *44* (7), 900–908.

ABSTRACT OF THE DISSERTATION

From Nanoparticles to Non-Covalent Interactions: Electron Transfer in Inorganic Supramolecular Mixed Valence Systems

by

Gabriele Canzi

Doctor of Philosophy in Chemistry

University of California, San Diego, 2014

Professor Clifford P. Kubiak, Chair

Understanding the intricacies of inner sphere electron transfer has been a challenge for nearly 50 years. Since the preparation of the Creutz-Taube ion extensive research in inorganic mixed valence systems has been performed. We employ coalescence of ν(CO) bandshapes observed in the 1-D infrared (IR) spectra of mixed valence complexes to determine rate constants of electron transfer (ET). Herein we report synthesis, characterization, and spectroscopy of Ru_3O clusters bound to metallic

nanoparticles, and report ET rates in the "ultrafast" regime. We observe that ET rates are faster when there is favorable electronic alignment between the Ru clusters and the Au nanoparticle. In addition, results show that ground state ET rate constants that are in the "ultrafast" regime depend on the pre-exponential term within the frequency factor, ν_N, not the activation energy as expected in a system undergoing ergodic electron transfer.

We extended our knowledge of these complexes by studying ET at a semiconducting nanoparticle interface. Working in collaboration with Prof. Emily Weiss at Northwestern University, a complementary view of the parameters that govern ET in such systems has been developed by investigating ET rates between the triruthenium clusters and QDs. The photoinduced electron transfer rate from photoexcited CdSe QDs to triruthenium clusters having either a pyridine-4-carboxylic acid or a 4-mercaptopyridine linkage are reported. Results show that the intrinsic charge separation rate constant ($k_{CS,int}$), is approximately seven times faster for a thiol linked cluster compared to a nicotinic acid bound cluster. Thus the charge transfer rates between colloidal quantum dots and redox-active ligands adsorbed to their surfaces can be tuned through the choice of the coordinating headgroup of the ligand.

We report that exchange of electrons across hydrogen bonds can increase the strength of typically weak interactions. A thermodynamically stable mixed valence dimer is obtained upon the one electron reduction of a Ru_3O cluster with a isonicotinic acid ancillary ligand. Observed intervalence charge transfer bands (IVCT) indicate significant coupling between the two Ru centers through linked by a hydrogen bonding interaction. The IVCT bands are found to be best explained by a semi-classical 3-state model, further highlighting the importance of the bridging interaction in these systems. Additionally, we

report that the electronic coupling between two metal centers can be modulated by simple ancillary ligand substitution. The wavefunction overlap of two metal centers bridged by a hydrogen bond is found to be non-zero.

We report a series of new Ru_3O clusters with ancillary ligands capable of pi-stacking in solution upon a single electron reduction. Large splittings are observed berween the reductions in the electrochemical responses of these newly synthesized systems. The effects on the electrochemical splitting of the reduction waves by donating and withdrawing ligands on the “bridge” are compared. A crystal structure of the ground state shows no significant evidence of pi-pi interaction between clusters in solution.

The major themes of this thesis are the role of electronic coupling, H_{ab}, on long range ET in supramolecular mixed valence systems, and the importance of the bridging interaction in modulating H_{ab} in these systems.

Chapter 1

Introduction to electron transfer and its theory

1.1 Introduction

Electron Transfer (ET) is everywhere: it is arguably the most important reaction in nature. Despite its beautiful simplicity, much is yet to be understood about this elementary reaction, due in part to its fast nature. The advent of the study of ET reactions dates back to the early 1950s, when theoretical work could first be supported by experimental observations, thanks in large part to the introduction of new instrumentation capable of dealing with the timescales required to study ET (lasers).[1-3]

One of the most exciting aspects of studying ET reactions has been the constant intertwining of theory and experiment that helped define what we know today. Although, by self admission, theory is above and beyond the scope of my work (and way over my head), some of the results in the upcoming chapters would not have the same impact and resonance in the chemical community if it weren't for

the theoretical models used to explain some of the phenomena that I have observed experimentally.

This thesis is not only about the fundamentals of electron transfer in inorganic mixed valence complexes, but also about the importance of donor-bridge-acceptor systems (DBA) in general. In fact, this thesis is as much about electron transfer as it is about the importance of the bridging interaction in supramolecular donor-bridge-acceptor mixed valence systems. The bridging ligand plays and has played a vital role in the systems that will be presented in this introduction and the following chapters. After 20 years of research on molecularly bridged Ru_3O clusters, we wanted to expand our knowledge of these very important complexes by adding layers of complexity to these already intricate supramolecular systems.

Ben Lear, with whom I wish I could have worked with during my graduate career, wrote in his thesis that the bridge is able to mediate electronic coupling between the redox sites within the molecule, thus electronic coupling is dependent on the bridge. With this in mind, we approached this work with the intent of looking into more complex bridges to better understand the chemistry around us and in nature's systems.

There is a natural separation in this thesis due to the nature of the systems I worked with. The first section concerns the investigation of ET and ET parameters between Ru_3O clusters attached to a Au nanoparticle surface, as well as photoinduced ET between Ru_3O clusters with different linking groups and semiconducting quantum dots (QDs) (CdS and CdSe). The second section aims to

describe ET between metal centers bridged by a non-covalent interaction. Of particular interest are hydrogen bonds and π-stacking systems for their importance as natural system mimics.

1.2 History and introduction to Marcus-Hush theory

This initial chapter serves as an introduction to the underlying concepts that will follow throughout this thesis. Although most of the information presented here will be re-emphasized and dispersed in following chapters, this is the most fitting way to give a very abridged version of the general theory of ET and inorganic mixed valence systems. Before we can start a complex discussion of the intricacies of electron transfer theory, we need to look at its history. There are two types of electron transfer in nature: intermolecular and intramolecular electron transfer. The original electron transfer theory, developed by Marcus in the early 1950s, focused on the first type of electron transfer, where two metal ions exchange an electron in solution.[1,3] Marcus developed his famous theory by envisioning potential energy surfaces for both the reactant (donor) side and product (acceptor) side of an electron exchange reaction.[1-3] These potential energy surfaces are derived from simple harmonic oscillator approximations along a reaction coordinate, and hold true for both inter and intramolecular ET. The donor and acceptor parabolas are placed with their minima on the reaction coordinate, representing the most stable configuration if an electron were to be localized on either the donor or acceptor site.[1] It is amazing

that most of the theory that has stimulated a half century of research in electron transfer is wholly based on two intersecting parabolas!

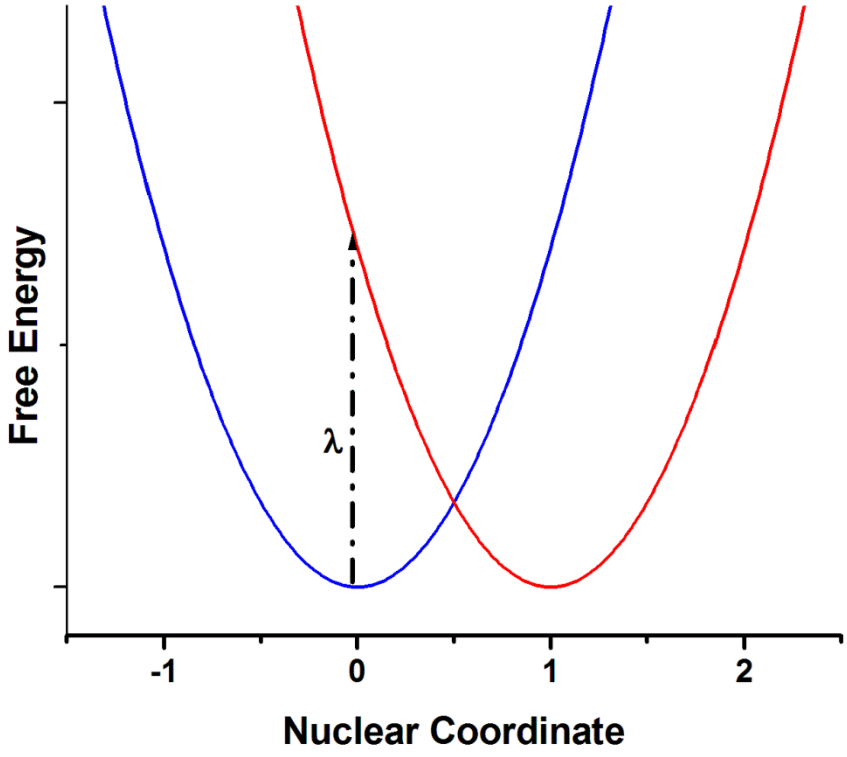

Figure 1.1. Potential energy curves for the donor (blue) and acceptor (red) sites of a diabatic system undergoing electron transfer. The reorganization energy, λ (dashed line), represents the energy required for optical electron transfer.

In subsequent years Hush, Newton, and Sutin added to classical Marcus theory to develop the Marcus-Hush theory that we know today.[4-8] In particular Noel Hush made the most prominent addition to Marcus theory by predicting two interacting metal centers should exhibit an intervalence charge transfer band (IVCT). Additionally, he predicted that this IVCT band would either be observed in

the UV, visible or near infrared region, and that the electronic coupling matrix element, H_{ab}, can be calculated directly from it.[5] A short time after Marcus and Hush laid out their theory of electron transfer, Henry Taube and his group, most notably Carol Creutz, successfully synthesized a bridged ruthenium complex to investigate intramolecular electron transfer.[9] The preparation of the Creutz-Taube ion finally allowed for in-depth investigations of the process and energetics of electron transfer in solution. This simple ion has single handedly sparked 50 years of research on the mechanisms and theory of electron exchange between two covalently linked interacting metal centers. As stated earlier, there has always been a synergistic effect stemming from the close interrelation between theory and experimental work on electron transfer. This was particularly apparent in the case of the Creutz-Taube ion. In fact, a major breakthrough of the early papers on the electronic spectra of the Creutz-Taube and biferrocenium mixed valence ions[10-14] was the validation of Noel Hush's model for electron transfer and the confirmation of Hush's bold prediction that mixed valence complexes that display reasonable electronic coupling should exhibit intervalence charge transfer bands, and that H_{ab} can be estimated from the IVCT band.[5,9]

Generally the rate constant of a reaction that is dependent on temperature is given in the Arrhenius form by[15];

$$k = A\exp\left[-\frac{E_a}{RT}\right]$$

Where A is the pre-exponential factor, E_a is the activation energy, R is the gas constant, and T is the temperature of the system. In the case of an electron transfer,

the activation energy Ea is generally described by ΔG*, which is the energy required for a thermal electron transfer event. Ultimately this gives k_{et} as[16,17];

$$k_{et} = \kappa \nu_N \exp\left[-\frac{\Delta G^*}{RT}\right]$$

In the Marcus treatment, which became known simply as "Marcus Theory", ΔG* is the point at which the donor and acceptor potential energy surfaces intersect. In optical electron transfer, light can be used to promote the electron from the reactant side to the products side. The energy required for promoting the electron is given by the reorganization energy, expressed as λ.

Marcus theory derives a simple relationship between ΔG^* and λ, the vertical reorganization energy, as[16]:

$$\Delta G^* = \frac{\lambda}{4}\left(1 + \frac{\Delta G^0}{\lambda}\right)^2$$

The reorganization energy is composed of two terms, an outer sphere component (λ_o) related to the solvent and an inner sphere component (λ_i) related to the complex itself to give:

$$\lambda = \lambda_o + \lambda_i$$

The inner sphere component is derived from equilibrium structural differences between product and reactant states and is expressed as[18]:

$$\lambda_i = \frac{1}{2}\sum_i f_i\,(r_D^{eq} - r_A^{eq})^2$$

where f_i is the reduced force constant for the *ith* vibration, r_D^{eq}, r_A^{eq} are the equilibrium bond lengths of products and reactants summed over all intramolecular vibrations. The outersphere reorganization is given by[4]:

$$\lambda_o = \frac{(\Delta e)^2}{8\pi}\left(\frac{1}{\varepsilon_{op}} - \frac{1}{\varepsilon_s}\right)\int (D_D - D_A)^2 d\tau$$

where Δe is the charge transferred, ε_{op} and ε_s are the optical and static dielectric constants of the solvent, and D_D and D_A represent the distance of the electron transfer.

The term $(\frac{1}{\varepsilon_{op}} - \frac{1}{\varepsilon_s})$, known as the Pekar factor[19], assumes that the solvent is treated as a dielectric continuum and is the only solvent dependent factor.[3] The Pekar factor represents the change in orientation polarization rather than nuclear and electronic polarization of the solvent. The orientation polarization and the electronic polarization are the two major contributions to the reorganization free energy of the solvent upon ET. The electronic polarization is much too fast to contribute to λ_o and remains in equilibrium in the timescale of the ET event. The orientation polarization, on the other hand, is on the time scale of 10^{-13} - 10^{-11} s and greatly contributes to the activation energy of ET by being accounted in the only solvent dependent term for the outer-sphere reorganization energy.[20]

Returning to the equation for k_{et}, the pre-exponential factor is of extreme importance to ET, as it depends on the nature of the transfer reaction. It is represented as $\kappa\nu_N$ where κ is the adiabaticity factor, also known as the transmission coefficient, which represents the frequency at which an electron will hop from the reactant to the product potential energy curve, and ν_N which is the nuclear frequency factor and is dependent on the nuclear coordinate frequencies.[21] The transmission coefficient tells us if an electron will transfer from the reactant

parabola to the product parabola. In uncoupled systems, where the adiabaticity factor is <<1, the system is diabatic, or made up of two distinct "baths." In bridged systems the electronic wavefunctions can have significant overlap and can readily mix. This mixing is quantified by the electronic coupling matrix element, $H_{ab} = \langle \Psi_R | H | \Psi_P \rangle$. As electronic coupling increases so does the adiabiaticity factor. As κ approaches 1 the system shifts from diabatic to adiabatic. This means that when significant electronic coupling, H_{ab}, is present, and the donor-acceptor wavefunctions overlap. In this case, the potential energy surfaces shift towards having a common single minimum rather than two distinct minima, as shown in Figure 1.2. When κ=1 the system is fully adiabatic and is no longer described by two "baths" but rather a single "bath" represented by a common potential energy surface.

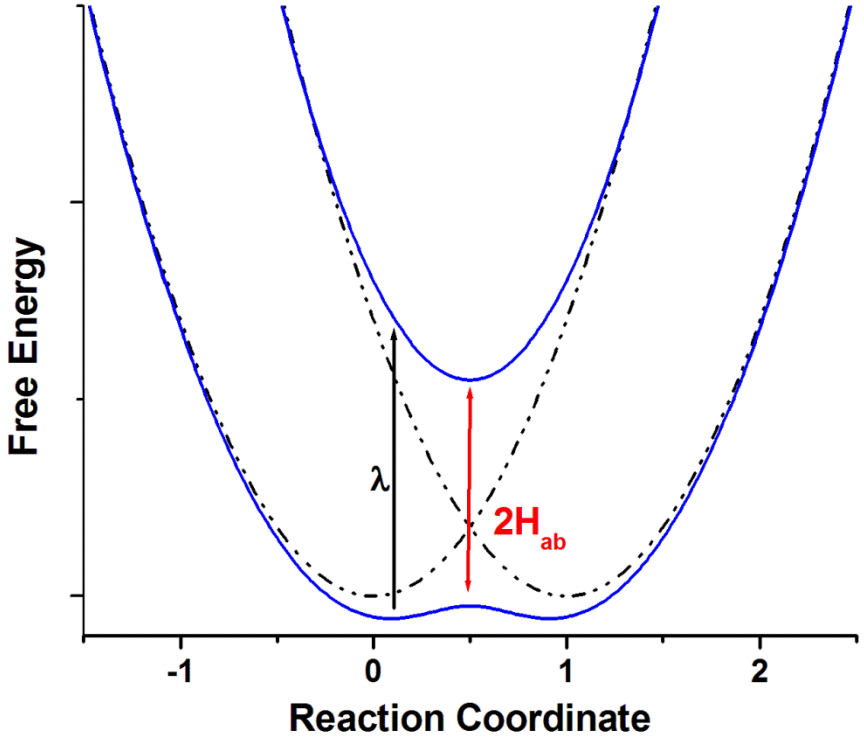

Figure 1.2. Diabatic (black dashed lines) and adiabatic (blue lines) potential energy surface for a two-state mixed valence system. λ is the energy required for an optical excitation from the donor to acceptor. H_{ab} is the electronic coupling.

1.3 Robin Day classification of mixed valence complexes

In 1967 Robin and Day published a ground breaking study attempting to classify mixed valence systems based on the extent of electronic coupling present.[22] By thoroughly investigating the spectroscopic, magnetic, and electrical properties of a number of transition metal mixed valence complexes, the authors created three distinct classes in the what is now called the Robin-Day classification of mixed valence compounds.[17,22-24]

In Class I there is no or negligible electronic coupling and the system is considered diabatic, with the products and reactant sides being represented by two distinct parabolas. As the electronic coupling increases it becomes moderate. Moderate electronic coupling causes a system to shift from diabatic to weakly adiabatic. A system with moderate H_{ab} is classified as Class II. When the electronic coupling is large, the potential energy surfaces for the products and reactants are represented by a single minimum and the now fully delocalized system is classified as Class III. In a Class III system, one that is strongly adiabatic, an electron can freely transfer between products and reactants in a barrierless manner.

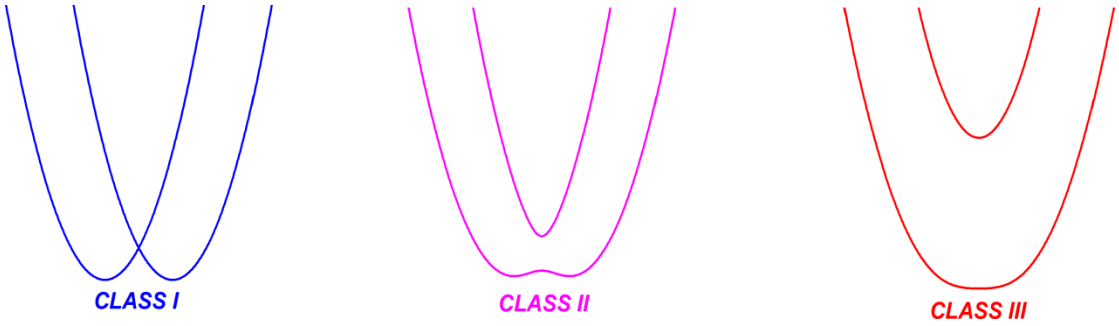

Figure 1.3. Potential energy curves of the three Robin Day classes of mixed valence with increasing electronic coupling energy going from left to right. Class I (left) represents a diabatic system, Class II (center) represents a weakly adiabatic system, and Class III (right) represents a strongly adiabatic system.

1.4 Abridged history of Ru_3O complexes

Most of the inorganic mixed valence systems that have been studied in the Kubiak laboratory and that will be presented in the following chapters are based on ruthenium, specifically oxo-centered tri-nuclear ruthenium clusters, Ru_3O. Mixed valence systems are mostly composed of ruthenium because of the stability of Ru^{II} and Ru^{III} oxidation states, and in our specific case, ligands coordinated to the

available coordination sites are typically not labile whem compared to other oxo-centered clusters.[12,25]

The story of oxo-centered tri-nuclear ruthenium clusters started in the 1970s when Spencer and Wilkinson synthesized and isolated the first $Ru_3O(OAc)_6L_3$ cluster and actively studied its magnetic and redox processes.[26-28]. In 1972 Cotton and Norman reported the first crystal structure of an oxo-centered ruthenium cluster.[26] In 1974 Spencer and Wilkinson again revisited the reactivity of the previously isolated $Ru_3O(OAc)_6L_3$ clusters with π-acids.[29] Spencer and Wilkinson investigated species formed from the parent complex by reduction with carbon monoxide, methyl isocyanide, and sulfur dioxide.[29] Of particular interest to this thesis is the reaction with carbon monoxide, *vide infra*. Years after the synthesis and characterization of the monomeric forms of these trinuclear ruthenium clusters, Thomas Meyer from the University of North Carolina, Chapel Hill synthesized the first dimeric and trimeric form of these Ru_3O clusters systems using pyrazine (pz) as the bridging ligand.[30-32] The Kubiak lab started working with ruthenium mixed valence complexes in the late 1990s.[33,34] As Cliff recounted in his recent ACS Inorganic Award paper,[33] it all started with an encounter with Professor Tasuku Ito from Tohoku Univeristy, in Sendai Japan. Professor Ito knew Cliff had access to the necessary equipment, in particular a custom made IR reflectance spectroelectrochemical cell,[35] to study and calculate electron transfer rates from the dynamic coalescence of the ν(CO) using Bloch lineshape analysis.

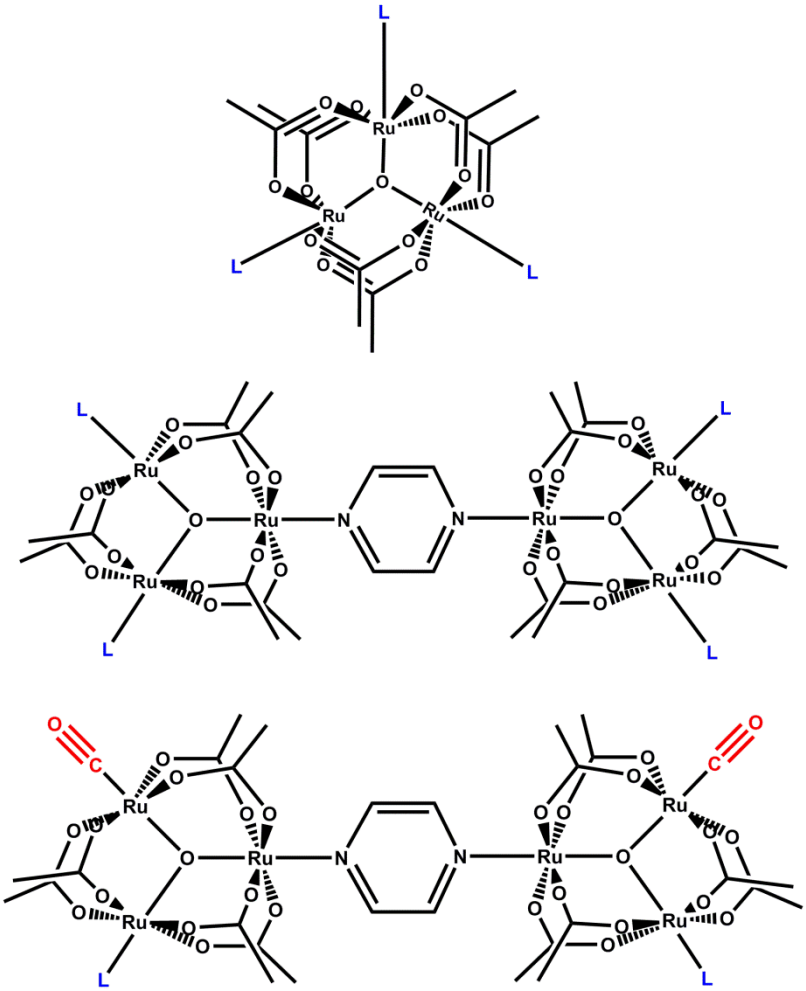

Figure 1.4. Drawings of mixed valence ruthenium systems illustrating the original Spencer and Wilkinson framework (top), the Meyer dimeric systems (center), and Ito and Kubiak dimeric systems with carbonyls coordinated to one of the three available rutheniums.

The Ito and Kubiak groups worked closely together on studying the molecularly bridged mixed valence ions of the form $[Ru_3(\mu_3\text{-}O)(OAc)_6(CO)(py)\text{-}(\mu_2\text{-}BL)\text{-}Ru_3(\mu_3\text{-}O)(OAc)_6(CO)(py)]^{-1}$, where L = a pyridyl ligand and BL = pyrazine or bipyridine. In 1997 Kubiak and Ito successfully reported, using the dynamic coalescence of ν(CO) in IR, the first calculated ground state intramolecular

rate of ET for a mixed valence ion.[34] The collaborative work between the Ito and Kubiak group continued until Prof. Ito's retirement. The Kubiak group continues its efforts in studying the electron dynamics of Ru_3O mixed valence ions. This research has expanded considerably throughout the last two decades, and has touched on many of the fundamental aspects of physical and inorganic chemistry, from synthesizing mixed valence isomers, to host-guest interactions, to measuring self exchange ET rates from NMR and redefining the models used to describe mixed valence behavior and its classification.[25,36-59]

1.5 References

(1) Marcus, R. A. *Annu. Rev. Phys. Chem.* **1964**, *15*, 155.

(2) Marcus, R. A. *Angew. Chem. Int.- Ed.* **1993**, *32*, 1111.

(3) Marcus, R. A. *The Journal of Chemical Physics* **1956**, *24*, 966.

(4) Sutin, N. J. *Prog. Inorg. Chem.* **1983**, *30*, 441.

(5) Hush, N. S. *Prog. Inorg. Chem.* **1967**, *8*, 391.

(6) Newton, M. D.; Sutin, N. *Annual Review of Physical Chemistry* **1984**, *35*, 437.

(7) Hush, N. S. *Transactions of the Faraday Society* **1961**, *57*, 557.

(8) Marcus, R. A.; Sutin, N. *Comments on Inorganic Chemistry* **1986**, *5*, 119.

(9) Creutz, C.; Taube, H. *J. Am. Chem. Soc.* **1969**, *91*, 3988.

(10) Cowan, D. O.; Kaufman, F. *Journal of the American Chemical Society* **1970**, *92*, 219.

(11) Hillman, M.; Kvick, A. *Organometallics* **1983**, *2*, 1780.

(12) Creutz, C. *Prog. Inorg. Chem.* **1983**, *30*, 1.

(13) Creutz, C.; Taube, H. *J. Am. Chem. Soc.* **1973**, *95*, 1086.

(14) Ford, P. C.; Rudd, D. P.; Gaunder, R.; Taube, H. *Journal of the American Chemical Society* **1968**, *90*, 1187.

(15) Logan, S. R. *Journal of Chemical Education* **1982**, *59*, 279.

(16) Brunschwig, B. S.; Sutin, N. *Coordination Chemistry Reviews* **1999**, *187*, 233.

(17) Brunschwig, B. S.; Creutz, C.; Sutin, N. *Chem. Soc. Rev.* **2002**, *31*, 168.

(18) Bolton James, R.; Archer Mary, D. In *Electron Transfer in Inorganic, Organic, and Biological Systems*; American Chemical Society: 1991; Vol. 228, p 7.

(19) Pekar, S. *Zhurnal Eksperimentalnoi Teor. Fiz.* **1946**, *16*, 335.

(20) Astruc, D. *Electron Transfer and Radical Processes in Transition-Metal Chemistry*; Wiley-VCH: New York, 1995.

(21) Weaver, M. J. *Chemical Reviews* **1992**, *92*, 463.

(22) Robin, M. B.; Day, P. *Adv. Inorg. Chem. Radiochem.* **1967**, *10*, 247.

(23) Day, P.; Hush, N. S.; Clark, R. J. H. *Philosophical Transactions of the Royal Society A: Mathematical, Physical and Engineering Sciences* **2008**, *366*, 5.

(24) Demadis, K. D.; Hartshorn, C. M.; Meyer, T. J. *Chem. Rev.* **2001**, *101*, 2655.

(25) Goeltz, J. C.; Hanson, C. J.; Kubiak, C. P. *Inorganic Chemistry (Washington, DC, United States)* **2009**, *48*, 4763.

(26) Cotton, F. A.; Norman Jr, J. G. *Inorganica Chimica Acta* **1972**, *6*, 411.

(27) Spencer, A.; Wilkinson, G. *Journal of the Chemical Society, Dalton Transactions* **1972**, 1570.

(28) Stephenson, T. A.; Wilkinson, G. *Journal of Inorganic and Nuclear Chemistry* **1966**, *28*, 2285.

(29) Spencer, A.; Wilkinson, G. *Journal of the Chemical Society, Dalton Transactions* **1974**, 786.

(30) Baumann, J. A.; Salmon, D. J.; Wilson, S. T.; Meyer, T. J. *Inorganic Chemistry* **1979**, *18*, 2472.

(31) Baumann, J. A.; Salmon, D. J.; Wilson, S. T.; Meyer, T. J.; Hatfield, W. E. *Inorganic Chemistry* **1978**, *17*, 3342.

(32) Baumann, J. A.; Wilson, S. T.; Salmon, D. J.; Hood, P. L.; Meyer, T. J. *Journal of the American Chemical Society* **1979**, *101*, 2916.

(33) Kubiak, C. P. *Inorganic Chemistry* **2013**, *52*, 5663.

(34) Ito, T.; Hamaguchi, T.; Nagino, H.; Yamaguchi, T.; Washington, J.; Kubiak, C. P. *Science (USA)* **1997**, *277*, 660.

(35) Zavarine, I. S.; Kubiak, C. P. *J. Electroanal. Chem.* **2001**, *495*, 106.

(36) Canzi, G.; Goeltz, J. C.; Henderson, J. S.; Park, R. E.; Maruggi, C.; Kubiak, C. P. *Journal of the American Chemical Society* **2014**, *136*, 1710.

(37) Canzi, G.; Kubiak, C. P. *Small* **2011**, *7*, 1967.

(38) Canzi, G.; Kubiak, C. P. *The Journal of Physical Chemistry C* **2012**, *116*, 6560.

(39) Glover, S. D.; Goeltz, J. C.; Lear, B. J.; Kubiak, C. P. *Eur. J. Inorg. Chem.* **2009**, 585.

(40) Glover, S. D.; Goeltz, J. C.; Lear, B. J.; Kubiak, C. P. *Coord. Chem. Rev.* **2010**, *254*, 331.

(41) Glover, S. D.; Kubiak, C. P. *J. Am. Chem. Soc.* **2011**, *133*, 8721.

(42) Glover, S. D.; Lear, B. J.; Salsman, C.; Londergan, C. H.; Kubiak, C. P. *Phil.Trans. Roy. Soc. A.* **2008**, *366*, 177.

(43) Goeltz, J. C.; Benson, E. E.; Kubiak, C. P. *Journal of Physical Chemistry B* **2010**, *114*, 14729.

(44) Goeltz, J. C.; Glover, S. D.; Hauk, J.; Kubiak, C. P.; Putman, R. D.; Rauchfuss, T. B. In *Inorg. Synth.* 2010; Vol. 35, p 156.

(45) Goeltz, J. C.; Kubiak, C. P. *J. Phys. Chem. C* **2008**, *112*, 8114.

(46) Goeltz, J. C.; Kubiak, C. P. *J. Am. Chem. Soc.* **2010**, *132*, 17390.

(47) Lear, B. J.; Glover, S. D.; Salsman, J. C.; Londergan, C. H.; Kubiak, C. P. *J. Am. Chem. Soc.* **2007**, *129*, 12772.

(48) Lear, B. J.; Kubiak, C. P. *Inorganic Chemistry (Washington, DC, United States)* **2006**, *45*, 7041.

(49) Lear, B. J.; Kubiak, C. P. *Journal of Physical Chemistry B* **2007**, *111*, 6766.

(50) Londergan, C. H.; Kubiak, C. P. *J. Phys. Chem. A.* **2003**, *107*, 9301.

(51) Londergan, C. H.; Kubiak, C. P. *Chemistry--A European Journal* **2003**, *9*, 5962.

(52) Londergan, C. H.; Rocha, R. C.; Brown, M. G.; Shreve, A. P.; Kubiak, C. P. *J. Am. Chem. Soc.* **2003**, *125*, 13912.

(53) Londergan, C. H.; Salsman, J. C.; Lear, B. J.; Kubiak, C. P. *Chemical Physics* **2006**, *324*, 57.

(54) Londergan, C. H.; Salsman, J. C.; Ronco, S.; Dolkas, L. M.; Kubiak, C. P. *J. Am. Chem. Soc.* **2002**, *124*, 6236.

(55) Londergan, C. H.; Salsman, J. C.; Ronco, S.; Kubiak, C. P. *Inorganic Chemistry (Washington, DC, United States)* **2003**, *42*, 926.

(56) Morris-Cohen, A. J.; Aruda, K. O.; Rasmussen, A. M.; Canzi, G.; Seideman, T.; Kubiak, C. P.; Weiss, E. A. *Physical Chemistry Chemical Physics* **2012**, *14*, 13794.

(57) Salsman, J. C.; Kubiak, C. P. In *Spectroelectrochemisty*; Kaim, W., Klein, A., Eds.; Royal Society of Chemistry: Cambridge, 2008, p 123.

(58) Salsman, J. C.; Kubiak, C. P.; Ito, T. *J. Am. Chem. Soc.* **2005**, *127*, 2382.

(59) Salsman, J. C.; Ronco, S.; Londergan, C. H.; Kubiak, C. P. *Inorganic Chemistry (Washington, DC, United States)* **2006**, *45*, 547.

Chapter 2

Mixed valence nanoclusters: fast electron transfer in mixed valence systems with a gold nanoparticle as the bridge

2.1 Introduction

This story begins as my graduate career did. It was 2008 when I walked into Cliff's office to talk about possible projects for me to work on. As physical/analytical student I was obviously drawn to the electron transfer project. I always have had a passion for nanotechnology too, so the idea was to investigate the possibility of using a nanoparticle as the bridge to a donor-bridge-acceptor system. Combining a chromophore and a nanoparticle wasn't such a novel idea as described, but observing and calculating the ground state electron transfer in these systems was. In fact, intramolecular electron transfer (ET) within mixed valence complexes, has been an area of considerable interest for nearly fifty years.[1,2] The breadth of mixed valence research and the complexity of systems studied has increased substantially.[1-5] Recently, our interest has turned to mixed valence systems linked to

nanomaterials. As stated before gold nanoparticles combined with molecular chromophores in supramolecular systems have been studied previously for their material, photochemical, and catalytic applications.[6-8] The study of charge transport across gold nanoparticles has been reported, but the available chromophores precluded direct measurement of the electron transfer rate constant, k_{ET}.[9]

Trinuclear ruthenium clusters of the form $(Ru_3O(OAc)_6(CO)(L)(L'))$, where L = 4-cyanopyridine ancillary ligand and L'= 4-4′ dipyridyldisulfide, were covalently bound to Au nanoparticles under reducing conditions. The surface coverage of the decorated nanoparticles was calculated to be approximately 20 clusters per nanoparticle, or $5x10^{10}$ clusters/cm^{-2}. The electron transfer properties of these mixed valence nanoclusters were probed by electrochemistry, electronic absorption spectroscopy, and IR spectroscopy.[5,10-12] The ruthenium bound carbonyls are an essential component in the estimation of electron transfer rates, and they serve as powerful probes of the oxidation states of the cluster to which they are bound.[5,10-14] Ru_3O cluster orbital energies can be electronically tuned by substituting ancillary pyridyl ligands with varying degrees of electron donor strengths, which in turn tunes the Ru_3O cluster energy relative to the π^* orbitals of the bridging ligands.[14] Previous work has established that ultrafast intramolecular electron transfer rate constants for ET within dimers of Ru trimers where pyrazine is the bridging ligand can be determined from the degree of ν(CO) coalescence in the mixed-valence state.[5,10-23] We report measurements of ultrafast electron transfer

across gold nanoparticles determined by spectrally coalesced ν(CO) lineshapes. At the time of writing this study was the first of its kind.

2.2 Results and discussion

The nanoparticles (NPs) were synthesized using a modified Brust-Schiffrin method,[24] using 1-dodecanethiol, 1-hexanethiol, and 1-octanethiol (full details in Supporting Information). The nanoparticles are dissolved in chloroform for storage, and no aggregation is observed over several weeks. The NPs are then characterized by UV-Vis, TEM, and diffusion ordered NMR spectroscopy (DOSY).[25] The average nanoparticle size ranges between 2-5 nm.

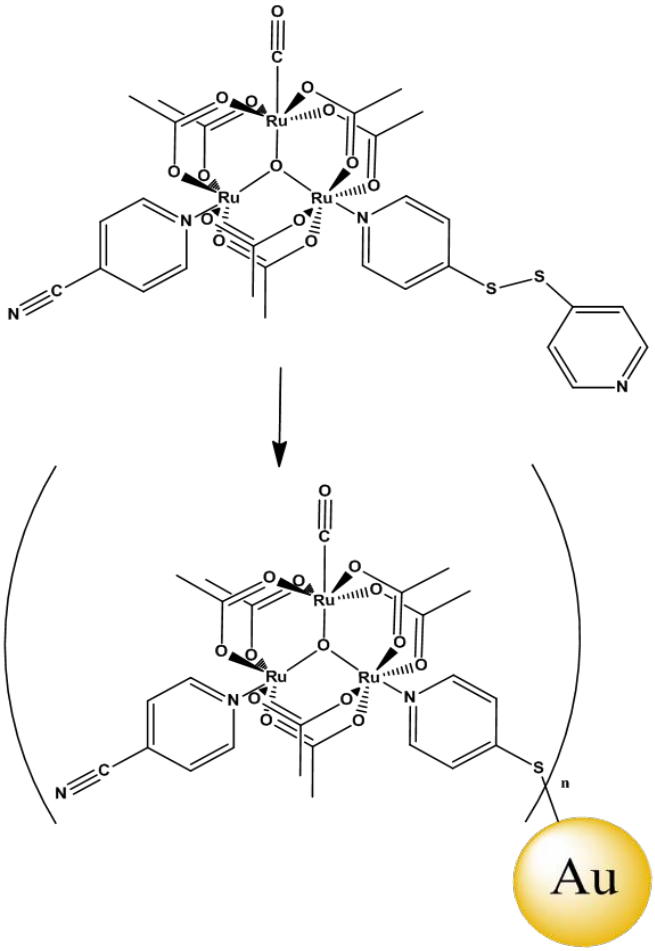

Figure 2.1. Drawing of the system used in this study: Free Ru monomer (top) and Ru monomer covalently bound to the surface of a Au nanoparticle as described in the text.

The electrochemistry of freely diffusing Ru_3O clusters shows two reversible oxidations in the anodic region, and one reversible reduction in the cathodic region. When a cluster binds to the nanoparticle, a second more cathodic irreversible single electron reduction is apparent, indicating the presence of a new multiply charged state.

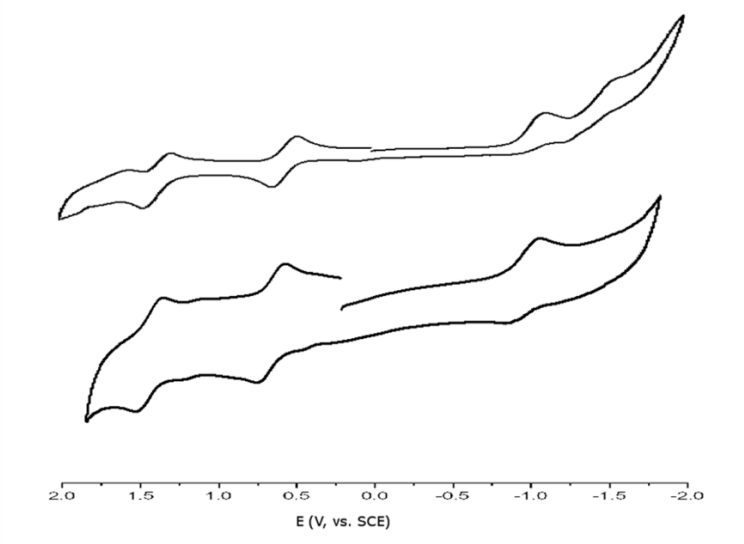

Figure 2.2. Electrochemistry of Au-$(Ru_3O)_n$ (cpy) at 50 mV/s (top) and unbound $Ru_3O(OAc)_6(CO)(cpy)_2$ at 200 mV/s (bottom). 1 mM with 0.1M TBAH as electrolyte, Pt working electrode, Pt counter electrode, AgCl reference under nitrogen atmosphere in CH_2Cl_2.

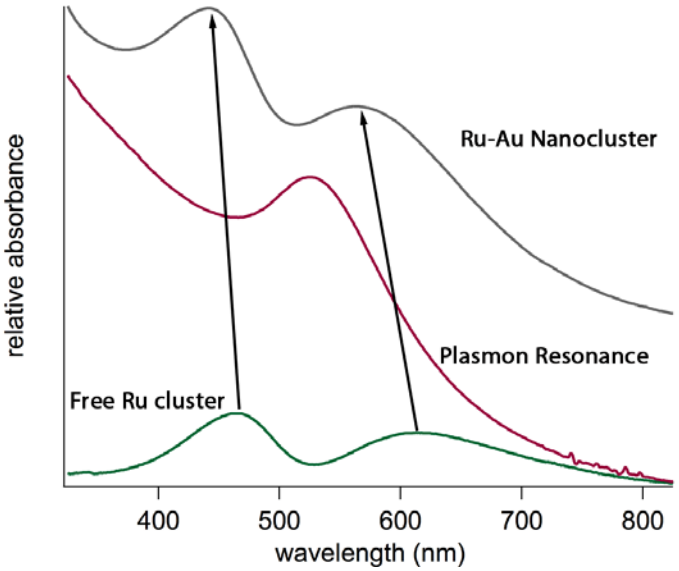

Figure 2.3. Absorption spectrum in $CHCl_3$ of the Au plasmon resonance of the free nanoparticles (red), Au/Ru nanocluster (grey), and unbound Ru monomer (green) with arrows pointing to the shifts of the band maximas upon covalent attachment to the NP surface. The spectra was offset for clarity.

Electronic absorption spectroscopy was utilized to provide information about the electronic structure of these new nanocluster assemblies. The free neutral Ru_3O monomer shows two distinct absorptions in the visible region, which have been previously assigned for similar systems.[5,10,14] The intensity at 450 nm is assigned as metal to ligand charge transfer (MLCT) and the lower energy peak at 615 nm is assigned as an intracluster charge transfer (ICCT) which is consistent with other known Ru_3O monomers.[14] The ICCT is relatively insensitive to ancillary and bridging ligand substitution[14] while the higher energy MLCT band responds to the electron donor ability of the pyridyl ancillary ligands.[14] The plasmon resonance band is a distinctive feature characteristic of gold nanoparticles, denoted by the red line in Figure 2.3. The resonance band, located at 520 nm in the absorption spectrum, shifts to a lower energy upon the attachment of the ruthenium clusters. Such a change in the plasmon resonance band of the gold NPs is evidence that the nanoparticles are increasing in size and the interparticle separation is decreasing, as dictated by the increasing ligand size, as described by Schiffrin et al.[26]

The bound nanoclusters show two distinct bands as well. Upon attachment of the Ru clusters to the Au nanoparticle, a shift to higher energies of both band maximas is observed. The MLCT is shifted to 430 nm and the lower energy ICCT shifts to 560 nm. The shift of the MLCT band to a higher energy is expected and represents the pyridine disulfide linkers becoming reduced to thiolate upon addition to the surface of the Au NPs. The ICCT band's large shift in energy is also predicted

as it represents the addition of the NP plasmon resonance to the ruthenium cluster ICCT band.

Valuable information concerning the electronic structure of Ru_3O clusters can be obtained from electronic absorption spectra, but electron transfer rates are best probed by dynamically coalesced lineshapes of ν(CO) band in infrared spectroscopy.[5,10-14,17-23] The infrared reflectance spectroelectrochemical responses (IR-SEC) show well defined carbonyl ν(CO) stretching vibration between 1940-1950 cm^{-1}. Upon electrochemical reduction of the Ru_3O clusters on the nanoparticle, the carbonyl ν(CO) band shifts to a lower frequency by ~40 cm^{-1} due to increased π-backbonding. Reducing half of the clusters on the nanoparticle gives rise to the mixed valence state, where marked coalescence of the ν(CO) is observed. This behavior is quite analogous to the studies of dynamical coalescence ν(CO) band shapes arising from ultrafast ET in molecular donor-bridge-acceptor mixed valence ions.[5,10-14,17-23]

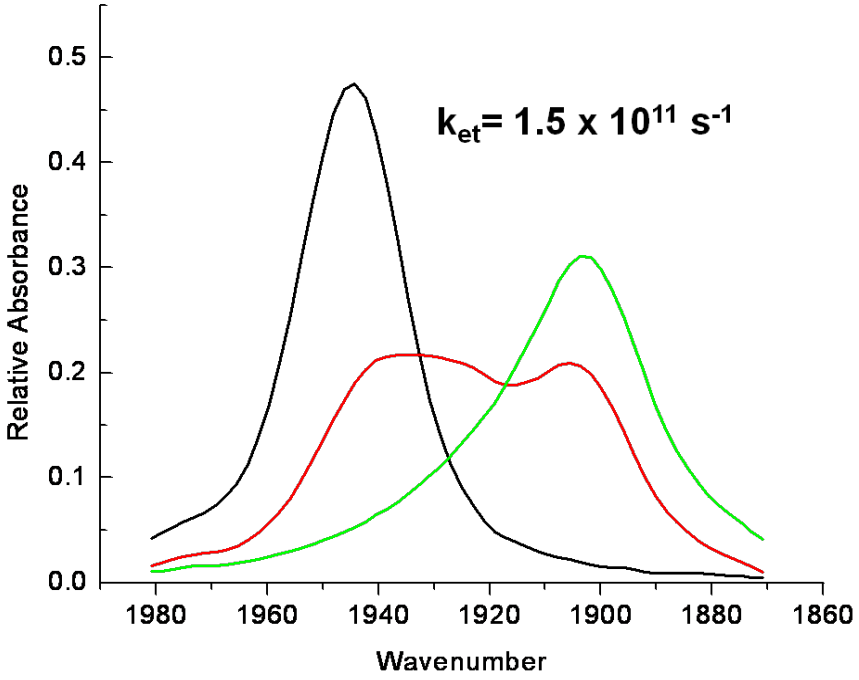

Figure 2.4. IR-SEC bandshapes for the non-reduced (black), mixed valence (red) and fully reduced state (green) in dichloromethane of the 4-cyanopyridine nanocluster.

In order to observe dynamic lineshape coalescence in the IR, the exchange process must be very fast, on the order of 10^{11}-10^{13} s^{-1}. Simulated rate constants[27] for the IR-SEC spectra of partially reduced ruthenium clusters on NPs indicate that the electron transfer rate is on the picosecond timescale, as reflected by the marked coalescence in the IR of the carbonyl ν(CO) bandshapes.

To ensure that the coalesced lineshapes observed were not due to intramolecular ET in a disulfide dimer found in solution, a disulfide-bridged Ru dimer was independently prepared. We know that ancillary ligand substitution will

influence electron transfer rates.[14,17,18] As previously stated, more electron donating ancillary ligands were shown to raise the overall cluster d-orbitals relative to those of the bridging ligand. This effect improves electronic communication between clusters and the bridge via a more favorable energetic alignment, yielding faster ET rates in the Ru "dimers of trimers." 4-dimethylaminopyridine (DMAP), a considerably more electron donating ancillary ligand than 4-cyanopyridine used in this study, was used in conjunction with a pyridyl disulfide bridge and the resulting IR-SEC response of this system in CH_2Cl_2 is shown in Figure 2.5.

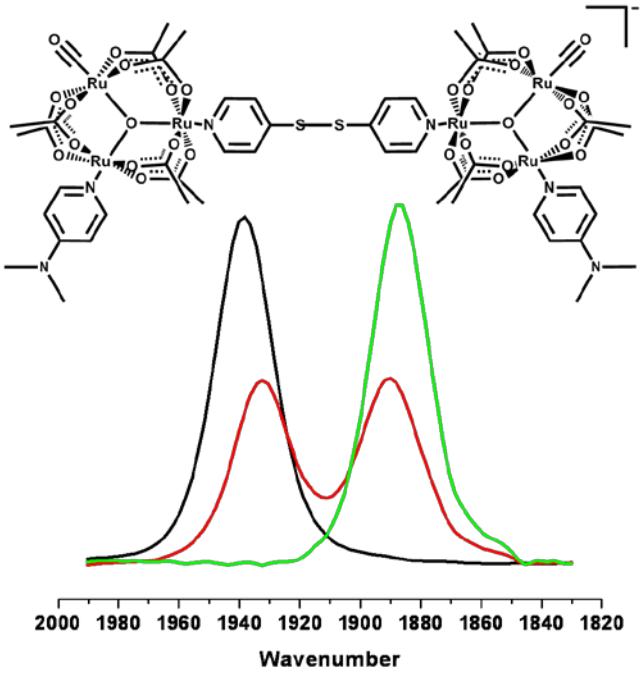

Figure 2.5. IR-SEC bandshapes for the non-reduced (black), mixed valence (red) and fully reduced state (green) in dichloromethane of the 4-dimethylaminopyridine disulfide dimer. The band coalescence in the mixed valence state is evidence that the electron transfer rate is slower in the disulfide dimers than the Au NP bridged clusters.

Clearly the degree of coalescence of the ν(CO) in the mixed valence state of the freely diffusing dimer is less compared to the nanoclusters reported here, despite having a more electron donating ancillary ligand. This is compelling evidence that the electron exchange in the IR spectra shown in Figure 3 *is not* between freely diffusing dimers in solution. 2D DOSY NMR also showed the absence of a freely diffusing mixed valence dimer in solution as the reducing conditions used in this study again indicate that the formation of a dimer is unlikely.

The ground state electron transfer rates of previously studied mixed valence "dimers of trimers" systems are highly solvent dependent.[5] A study of many dimers in various solvents showed that ET rates were under pre-exponential control and were particularly dependent on the solvent dipolar reorientation time, (t_{1e}).[11,17,18,28] To further probe the mixed valence behavior of the nanoclusters, IR-SEC responses of the cluster-nanoparticle assemblies were performed in dichloromethane, 1,2-dichloroethane, and 1,2-dimethoxyethane.

Table 2.1. Electron transfer rate constants and fundamental solvent parameters for the solvents used in this study.

Solvent	Rate (s^{-1})	I_x (PMIX)	Pekar Factor[a]
Dichloromethane	$1.5x10^{11}$	16.2	0.381
1,2 Dichloroethane	$1.3x10^{11}$	17.6	0.386
1,2 Dimethoxyethane	$0.8x10^{11}$	29.1	0.384

[a] $(1/\varepsilon_{OP} - 1/\varepsilon_S)$, where ε_{OP} is the optical dielectric and ε_S is the static dielectric

Vibrationally fast exchange was observed in all three solvents, with varying degrees of ν(CO) band coalescence, indicating that solvent dependence of ET is also present in the Ru complexed nanoclusters as well. A strong solvent dependence is

expected in the cluster-nanoparticle systems as the pyridine thiol acts as a bridge to the nanoparticle, much like a pyrizine bridge in the dimer systems. Various solvent parameters were considered and those that show strongest correlation with ET lifetimes correspond to the fast movement of solvent in response to a change in the dipole. In particular, a strong correlation was found between Maroncelli's solvent relaxation time (t_{1e}) and the electron transfer lifetimes for the mixed valence nanoclusters.[11,17,28] This indicates electron transfer rates for these nanoclusters are controlled by the pre-exponential nuclear frequency factor, ν_n, serving as further evidence that ET rates are in fact on the picosecond timescale.[11,17,28]

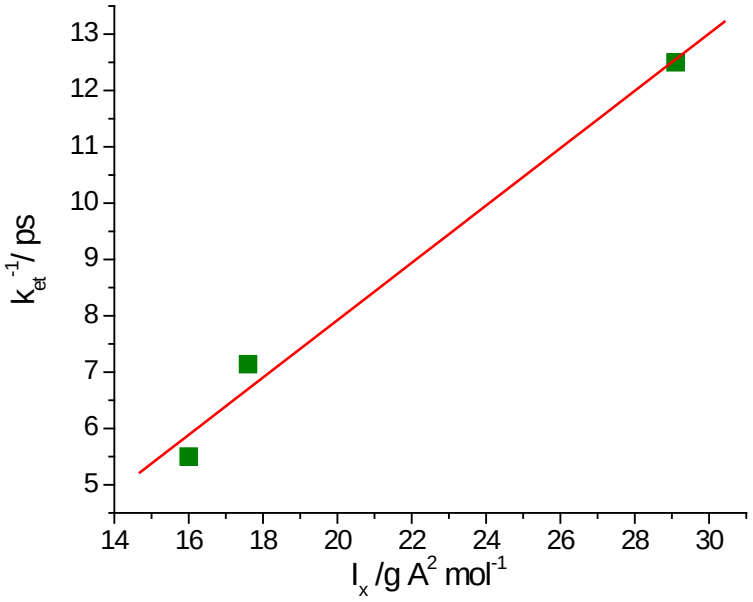

Figure 2.6. Graph of principal moment of inertia in the x-direction (PMIX) of the solvents used versus electron transfer lifetime in dichloromethane, 1,2 dichloroethane, and 1,2 dimethoxyethane.

2.3 Conclusions.

The mixed valence nanoscluster system presented here is the first example of a picosecond ground state electron transfer reaction through a gold nanoparticle, as evidenced by IR coalescence dynamic analysis. The rate at which ET is proceeding is remarkable considering the size of these nanoclusters and large distances between surface bound electron donors and acceptors. Gold is a ballistic conductor with a Fermi velocity of 1.4×10^6 m/s, and ultrafast ET across Au NPs is not to be unexpected. IT will be interesting to compare transport across various semiconductor and metallic NPs. Further studies elucidating the behavior of these systems with varying pyridyl ancillary ligand pKa and temperature are forthcoming. A most relevant study is one in which the effect of bridge state nanoparticle charging affects the ET mechanism.[29]

2.4 Experimental

General

All chemicals were used as received unless otherwise noted. CD_3CN was distilled under nitrogen from CaH_2. Electrochemistry and spectroscopy solvents were sparged with argon and dried over alumina and dispensed by a custom made solvent system. Elemental analysis was performed by Numega Labs in San Diego, CA.

Synthesis and characterization

The Ru_3O monomer was synthesized by a well known method, and purified by chromatography.[12,14,19,20] Briefly, $Ru_3O(OAc)_6(CO)(S)(S)$ where S = coordinated solvent, was obtained from reduction of the parent solvento complex, $Ru_3O(OAc)_6(S)_3$, by adding 0.8 equivalents of a reducing agent ($NaBH_4$) and pressurizing the vessel with CO (25 psi). $Ru_3O(OAc)_6(CO)(cyanopyridine)(H_2O)$ (118 mg, 0.148 mmol) was stirred in 25 mL CH_2Cl_2. 4-4'-dipyridyldisulfide (10 eq.) was added as a solid and the reaction was allowed to stir for 24-48 hours. The reaction was rotavapped at 35 ºC. The cluster was dissolved in 10 mL CH_2Cl_2 and filtered through celite to remove excess solid 4-4'-dipyridyldisulfide. More CH_2Cl_2 was added, and the product was precipitated with excess hexanes and collected on a frit. It was washed several times with hexanes and dried under vacuum overnight.

^{1}H NMR (500 MHz, δ): ppm 9.04 (d, J = 8.00 Hz, 2 H), 8.78 (d, J = 8.00 Hz, 2 H), 8.46(d, J = 7.50 Hz, 2 H), 8.21 (d, J = 7.50 Hz, 2 H), 7.63 (d, J = 9.50 Hz, 2 H), 7.11 (td, J=9.50, 2H), 1.95 (s, 6 H), 1.91 (s, 6 H), 1.70 (s, 6 H). UV/vis ($CHCl_3$) nm 280, 460, 625. IR cm^{-1} (CH_2Cl_2): 2241(m), 1951, 1711 (s), 1602, 1569, 1450 (s), 1420, 1350. Elemental analysis: Calc. for $Ru_3O(OAc)_6(CO)(cpy)(4\text{-}4'$ disulf) $C_{29}H_{30}N_2O_{14}Ru_3S_2$ C 35.22; H 3.05; N 5.48. Found 35.41; 3.23; 5.76 .

Spectroscopy

IR spectra were collected on a Bruker Equinox 55 FTIR spectrometer. IR-SEC was performed with a custom built reflectance cell mounted on a specular

reflectance unit.[30] UV/vis data were collected on a Shimadzu UV-3600 UV/vis/NIR spectrophotometer. Samples were enclosed in a Specac sealed liquid IR cell with CaF_2 windows with 0.5 mm and 1.0 mm path lengths.

Electrochemistry

Electrochemistry was performed with a BAS Epsilon potentiostat in dried deoxygenated CH_2Cl_2 with 0.1 M tetrabutylammonium hexafluorophosphate (TBAH, recrystallized from MeOH and dried under vacuum at 80 ºC) and 1 mM sample concentration at a scan rate of 100 mV/s in a glovebox. The working electrode was a 1.6 mm diameter gold disk. The counter electrode was a platinum wire, and the reference was a AgCl wire.

TEM imaging

TEM images were taken using a FEI Tecnai G2 Sphera equipped with a LaB_6 filament operating at an accelerating voltage of 200 kV. The Tecnai G2 Sphera is equipped with a GatanUltrascan 1000 UHS CCD camera. The samples were prepared by evaporating one drop (3.5μL) of a dilute $CHCl_3$ solution of the nanoclusters onto a 3x3 mm carbon coated copper grid. Images were analyzed using Image J software, available from NIH.

2D DOSY NMR sample preparation and acquisition

DOSY NMR samples were prepared using a previously reported method modified for use with the nanoclusters. 5mL of a 0.1 mM nanocluster solution was vacuum dried, 1mL of the preferred deuterated solvent was added, and then transferred to a 5mm medium walled NMR tube. Ferrocene was added, serving as the internal reference (approximately 0.1 mg). All data were acquired using a JEOL ECA 500 MHz spectrometer equipped with an inverse-geometry broadband NMR probe and processed using JEOL's Delta software. Exponential decays in the acquired DOSY data sets were fit using the CONTIN method.[31]

Note: Much of the material for this chapter comes directly from a manuscript entitled "Mixed Valence Nanoclusters: Fast Electron Transfer in Mixed Valence Systems with a Gold Nanoparticle as the Bridge" by Gabriele Canzi and Clifford P. Kubiak, which has been published in *Small,* **2011**, *7* (14), 1967-1971. DOI: 10.1002/smll.201100483 The dissertation author is the primary author of this manuscript.

2.5 References

(1) Hush, N. S. *Electrochim Acta* **1968**, *13*, 1005.

(2) Marcus, R. A. *Annu Rev Phys Chem* **1964**, *15*, 155.

(3) Demadis, K. D.; Hartshorn, C. M.; Meyer, T. J. *Chem. Rev.* **2001**, *101*, 2655.

(4) Demadis, K. D.; Neyhart, G. A.; Kober, E. M.; White, P. S.; Meyer, T. J. *Inorg. Chem.* **1999**, *38*, 5948.

(5) Ito, T.; Hamaguchi, T.; Nagino, H.; Yamaguchi, T.; Washington, J.; Kubiak, C. P. *Science* **1997**, *277*, 660.

(6) Daniel, M. C.; Astruc, D. *Chem Rev* **2004**, *104*, 293.

(7) Hu, M.; Chen, J. Y.; Li, Z. Y.; Au, L.; Hartland, G. V.; Li, X. D.; Marquez, M.; Xia, Y. N. *Chem Soc Rev* **2006**, *35*, 1084.

(8) Thomas, K. G.; Kamat, P. V. *Accounts of Chemical Research* **2003**, *36*, 888.

(9) Muller, C. I.; Lambert, C.; Steeger, M.; Forster, F.; Wiessner, M.; Scholl, A.; Reinert, F.; Kamp, M. *Chem Commun* **2009**, 6213.

(10) Ito, T.; Hamaguchi, T.; Nagino, H.; Yamaguchi, T.; Kido, H.; Zavarine, I. S.; Richmond, T.; Washington, J.; Kubiak, C. P. *Journal of the American Chemical Society* **1999**, *121*, 4625.

(11) Lear, B. J.; Glover, S. D.; Salsman, J. C.; Londergan, C. H.; Kubiak, C. P. *Journal of the American Chemical Society* **2007**, *129*, 12772.

(12) Londergan, C. H.; Salsman, J. C.; Lear, B. J.; Kubiak, C. P. *Chemical Physics* **2006**, *324*, 57.

(13) Londergan, C. H.; Salsman, J. C.; Ronco, S.; Dolkas, L. M.; Kubiak, C. P. *Journal of the American Chemical Society* **2002**, *124*, 6236.

(14) Salsman, J. C.; Ronco, S.; Londergan, C. H.; Kubiak, C. P. *Inorg Chem* **2006**, *45*, 547.

(15) Glover, S. D.; Goeltz, J. C.; Lear, B. J.; Kubiak, C. P. *Eur. J. Inorg. Chem.* **2009**, 585.

(16) Glover, S. D.; Goeltz, J. C.; Lear, B. J.; Kubiak, C. P. *Coord. Chem. Rev.* **2010**, *254*, 331.

(17) Glover, S. D.; Kubiak, C. P. *J. Am. Chem. Soc.* **2011**, *133*, 8721.

(18) Glover, S. D.; Lear, B. J.; Salsman, C.; Londergan, C. H.; Kubiak, C. P. *Phil.Trans. Roy. Soc. A.* **2008**, *366*, 177.

(19) Goeltz, J. C.; Benson, E. E.; Kubiak, C. P. *Journal of Physical Chemistry B* **2010**, *114*, 14729.

(20) Goeltz, J. C.; Glover, S. D.; Hauk, J.; Kubiak, C. P.; Putman, R. D.; Rauchfuss, T. B. In *Inorg. Synth.* 2010; Vol. 35, p 156.

(21) Goeltz, J. C.; Hanson, C. J.; Kubiak, C. P. *Inorg. Chem.* **2009**, *48*, 4763.

(22) Goeltz, J. C.; Kubiak, C. P. *J. Phys. Chem. C* **2008**, *112*, 8114.

(23) Goeltz, J. C.; Kubiak, C. P. *J. Am. Chem. Soc.* **2010**, *132*, 17390.

(24) Brust, M.; Walker, M.; Bethell, D.; Schiffrin, D. J.; Whyman, R. *J Chem Soc Chem Comm* **1994**, 801.

(25) Canzi, G.; Mrse, A. A.; Kubiak, C. P. *J. Phys. Chem. C* **2011**, *115*, 7972.

(26) Sendroiu, I. E.; Mertens, S. F. L.; Schiffrin, D. J. *Phys Chem Chem Phys* **2006**, *8*, 1430.

(27) McClung, R. E. D., VIBEX GL: A Program for the simulation of IR spectra of exchanging systems.

(28) Horng, M. L.; Gardecki, J. A.; Papazyan, A.; Maroncelli, M. *J Phys Chem* **1995**, *99*, 17311.

(29) Sardar, R.; Funston, A. M.; Mulvaney, P.; Murray, R. W. *Langmuir* **2009**, *25*, 13840.

(30) Zavarine, I. S.; Kubiak, C. P. *J. Electroanal. Chem.* **2001**, *495*, 106.

(31) Provencher, S. W. *Comp. Phys. Comm.* **1982**, *27*, 229.

Chapter 3

Ultrafast electron transfer across a gold nanoparticle: ancillary ligand and solvent influences.

3.1 Introduction

The simplest, yet most important reaction in nature is electron transfer (ET).[1] Years of research in physical, inorganic, and organic chemistry have been dedicated to understanding the fundamentals of this elementary reaction type.[2-4] Of particular interest to many in these fields are mixed valence complexes [5-8], which have been subjects of intense study since the preparation of the Creutz-Taube ion in the late 1960's.[9] Of these synthetic mixed valence ions the vast majority contain ruthenium because of the stability of the Ru^{II} and Ru^{III} states.[10]

Donor-bridge-acceptor (DBA) mixed valence systems of the type $[Ru_3O(OAc)_6(CO)L\text{-}pz\text{-}\ Ru_3O(OAc)_6(CO)L]^{-1}$ have been particularly revealing, since they show ground intermolecular ET on the picoseconds time scale. These complexes have unique ν(CO) stretching absorptions in the infrared (IR) spectrum

which have been indispensible in characterizing the complexes' mixed valence behavior.[11,12] The ν(CO) frequency is informative because of its ability to report on the electronic environment of Ru_3O cluster. Many of these complexes exhibit coalesced ν(CO) bands, indicating rates of ET on the vibrational timescale, $10^{11}s^{-1}$ to $10^{13}s^{-1}$.[11-16] With growing understanding of the fundamentals of ultrafast mixed valency we have been able to study more complex and sophisticated systems, especially the mixed valence properties of supramolecular structures that may find applications as solar energy catalysts, chemical sensors, and nanoswitches.[17,18] An example of the growing complexity of mixed valence interactions studied is mixed valency across hydrogen bonded Ru_3O clusters,[19] and our work on mixed valency across gold nanoparticles that was presented in chapter 2.[20]

In this chapter we expand on the concepts presented in chapter 2 to report ET rates, and how they are affected by ancillary ligand substitution, as well as solvent dependence of ET in mixed valence systems nanoclusters. Trinuclear ruthenium clusters of the type $[Ru_3O(OAc)_6(CO)(L)(pyS)]$, where L= 4-cyanopyridine (cpy), pyridine (py) and 4-dimethylaminopyridine (dmap), bound to a gold nanoparticle by a gold-sulfur bond are the focus of this chapter, and are shown in Figure 3.1. Through ancillary ligand substitution, the electronic communication between these clusters can be tuned to directly control the ground state electron transfer rate. ν(CO) bands will shift to either higher or lower frequencies based on the electron density present on each cluster. In addition to ligand substitution, solvent effects, which are known to affect ET rates in several ways, were probed by

observing infrared spectroelectrochemistry (IR-SEC) responses in various solvents, showing distinctive differences in the degrees of ν(CO) coalescence.

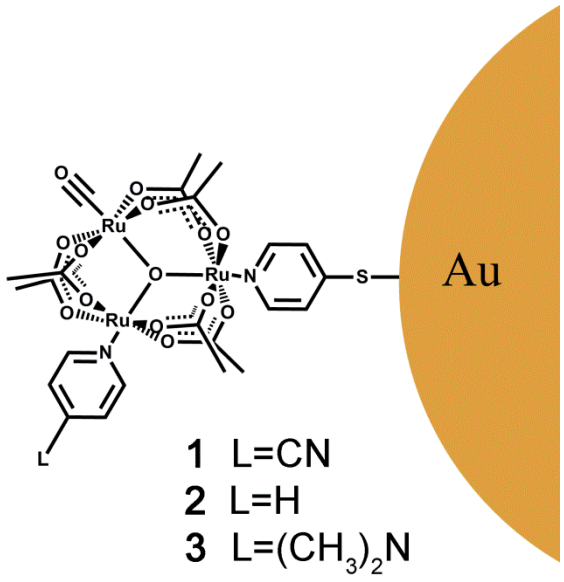

Figure 3.1. Structures of bound Ru_3O clusters with varying ancillary ligands, 4-cyanopyridine **(1)**, pyridine **(2)**, and 4-dimethylaminopyridine **(3)** on a Au nanoparticle used in this study.

Chapter 2 elucidated the first preparation and characterization of Au nanoparticle Ru_3O mixed valence assemblies.[20] Chapter 3 follows with a complete study of the ground state electron transfer rates trends based on systematic ligand substitution and solvent dependence. The results show that even in large supramolecular mixed valence systems where ET proceeds over very long (nm) distances, solvent dynamics still exert control on ET rates.

3.2 Results and discussion

Coalescence of ν(CO) spectra of Ru_3O clusters bound to Au nanoparticles has been previously interpreted in terms of ET on the picosecond time scale.[20] Here we exert additional control over ET by substituting the ancillary ligands on the Ru_3O clusters and by changing the surrounding solvent media. Complexes used in this study, oxo-centered trinuclear Ru clusters, commonly of the type $[Ru_3O(OAc)_6(CO)(L)(pyS\text{-}Spy)]$ are covalently attached to Au NPs upon reduction of the disulfide pyridine ligand by $LiBH_4$. The disulfide linker, 4-4' bipyridyl disulfide (pyS-Spy), is adjacent to the ancillary ligands used to tune the electronic coupling, which are essential in determining how ligand donating abilities affect ET rates.[21]

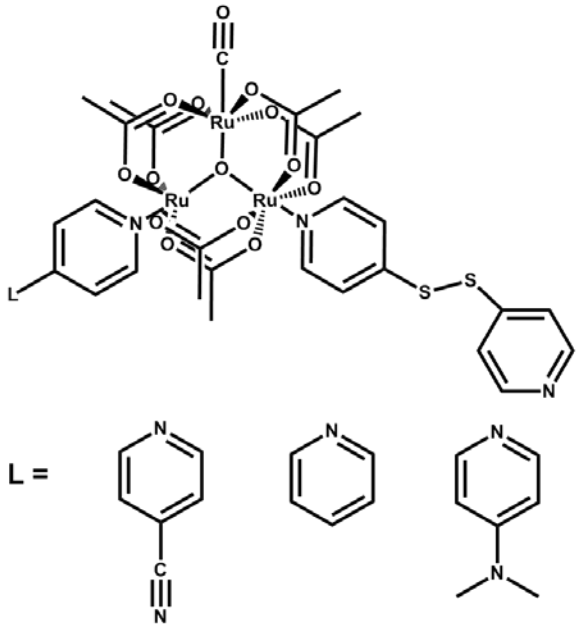

Figure 3.2. Structure of $[Ru_3O(OAc)_6(CO)(L)(pyS\text{-}Spy)]$ as synthesized in this study. Upon reduction of the disulfide using a BH_4, these monomers are bound to the Au nanoparticle via a Au-S bond as shown in Figure 3.1.

To characterize these systems, electrochemistry, TEM imaging, and 2D NMR Diffusion Ordered Spectroscopy (DOSY) were used to determine purity and relative size of the nanoparticles. We recently showed that the radius of a cluster determined *via* DOSY is consistent with radial measurements obtained by TEM imaging.[22]

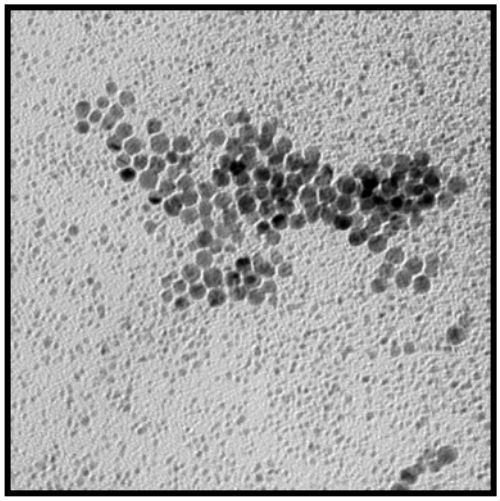

Figure 3.3. TEM image of Au nanoparticles at 200,000x magnification.

By using the diffusion rate ratio measured by DOSY between an internal standard (ferrocene), and the nanoclusters, along with the hydrodynamic radius of ferrocene, a size estimate of the nanoclusters (R_{Nc}) can be obtained.

$$R_{NC} = 0.3nm \text{ X } \frac{D_{FC}}{D_{NC}} \qquad (1)$$

The hydrodynamic radius of Fc is known to be 0.3nm[22,23], therefore by using Eq. 1 it is possible to approximate a particle size for the clusters. DOSY results

show that the nanoclusters have a size of about 4-5 nm. Excellent agreement is observed in NP radius as determined by the hydrodynamic radius of the nanoclusters in DOSY and the size given by TEM imaging.

Surface coverage of the Ru_3O clusters on the nanoparticle was calculated to be $5x10^{10}$ clusters/cm^{-2}, and was estimated by using a modified molecular dynamics method first described by Sarsa and co-workers.[24] The method utilizes molecular dynamics to determine surfactant surface density as a function of the radius. The average number of Ru clusters per nanoparticle is found to be 20-25, assuming an average NP sizes of 3-4 nm. To further validate the results of the method used to calculate the number of Ru clusters per NP, two additional methods were applied, with similar results. These two methods are presented at the end of the chapter.

Electrochemical results show two reversible oxidations and one reversible reduction for $[Ru_3O(OAc)_6(CO)(L)(dpyS)]$. Upon attachment to the Au NPs a more negative irreversible one electron reduction is apparent. This behavior is analogous to a molecular mixed valence ion, where the observed splitting of the reduction waves in the cyclic voltammogram is an indication of the comproportionation constant, $K_c = e^{nF\Delta E_{½}/RT}$, for the formation of the mixed valence ion from the complexes in two isovalent states.[13,14,16] The splitting in the Ru_3O nanoclusters is significant because it indicates increased electronic communication between the clusters, and the existence of a thermodynamically stable mixed valence state.

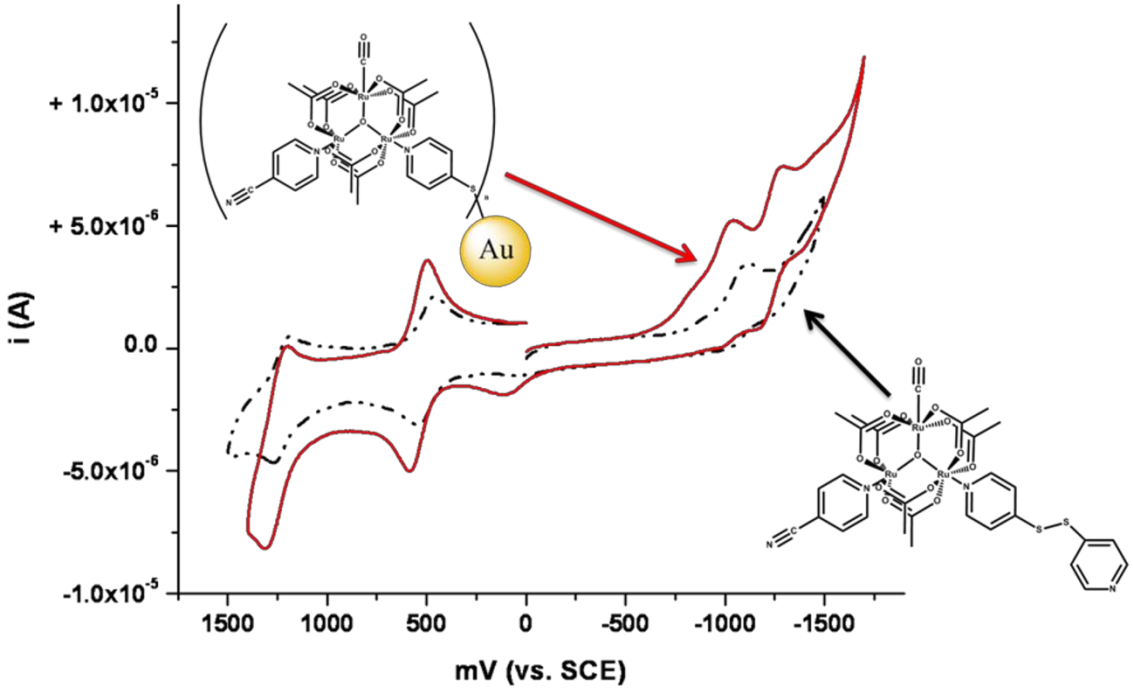

Figure 3.4. Cyclic voltammograms of freely diffusing Ru_3O clusters (black dotted line) and Au NP bound clusters (red solid line) in CH_2Cl_2, Au working electrode, Pt counter electronde, and Ag/AgCl wire as the reference electrode with 0.1 M TBAH as supporting electrolyte, approximately 2.0 mM sample concentrations, and a scan rate of 100 mV/s. 2 mM concentrations for the nanoclusters were calculated using 20 Ru_3O clusters per nanoparticle as an approximation. The nanoclusters electrochemical response clearly shows a second more negative irreversible reduction indicating the presence of multiply charged states and the presence of a thermodynamically stable mixed valence state.

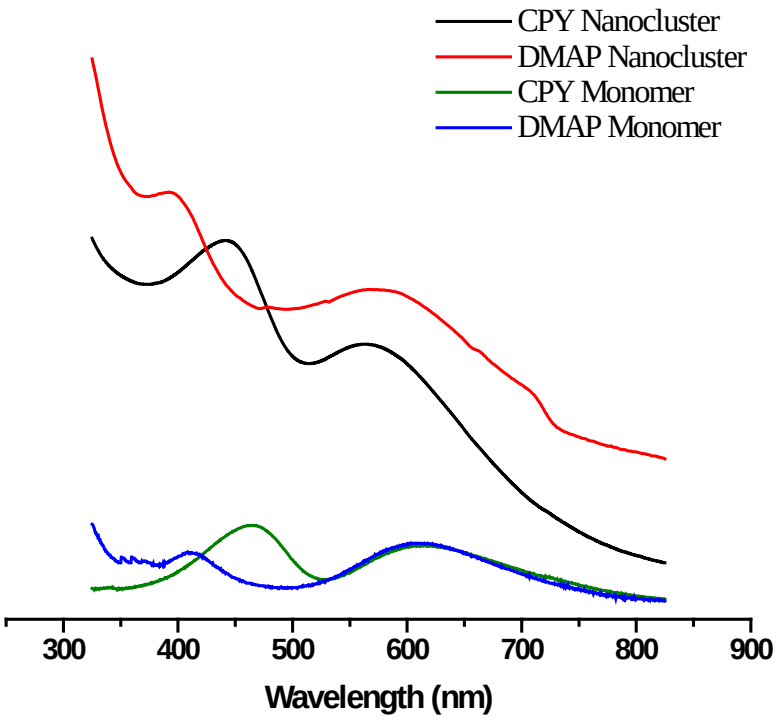

Figure 3.5. Electronic absorption spectra of bound and unbound clusters. Free Ru_3O clusters are shown in green (cpy) and blue (dmap). Au NP bound nanoclusters are shown in red (dmap) and black (cpy). Both freely diffusing and bound clusters show two distinctive features in the visible range. Upon binding to the NPs there is a clear shift to higher energies for both bands.

The electronic absorption spectra of $[Ru_3O(OAc)_6(CO)(L)(dpyS)]$ show two distinct absorptions in the visible region. A higher energy band located around 400-470 nm depending on the monomer, is assigned as metal to ligand charge transfer (MLCT) and a lower energy band located at 600-615 nm is assigned as intracluster charge transfer (ICCT), which is consistent with other known Ru_3O complexes.[12,14,21] The ICCT is relatively insensitive to ancillary and bridging ligand substitution, while the higher energy MLCT band responds to the electron donor

ability of the pyridyl ancillary ligands.[21] This is clearly shown in the absorption spectra shown in Figure 3.5 where there is a marked difference in the MLCT of $[Ru_3O(OAc)_6(CO)(cpy)(pyS\text{-}Spy)]$, green trace in Figure 3.5, and $[Ru_3O(OAc)_6(CO)(dmap)(pyS\text{-}Spy)]$ clusters, blue trace in Figure 3.5. The Ru_3O-NP nanoclusters also show two distinct bands. Upon attachment both the MLCT and ICCT shift to higher energies. The MLCT band's shift to higher energy is expected when the pyridine disulfide linkers become reduced and subsequently bound to the surface of the Au NPs. The ICCT band's large shift in energy is also predicted as it represents an addition of the NP plasmon resonance, located at 550nm, to the ruthenium cluster ICCT band.[20,25]

Infrared reflectance spectroelectrochemistry (IR-SEC), was used to monitor the ν(CO) stretches of the Ru_3O clusters as the NP mixed valence state is generated in various solvents. Electron transfer rate constants, k_{et}, were found to be in the ultrafast regime, as is evident by the coalescence of the ν(CO) bands. Coalescence of the ν(CO) is indicative of charge transfer on the vibrational (picosecond) timescale. Simulated k_{et} rate constants (details in SI) also verified an increase in rate with more electron-donating substituents on the ancillary ligands, as seen in the increased coalescence of the IR-SEC signals for the mixed valence state.

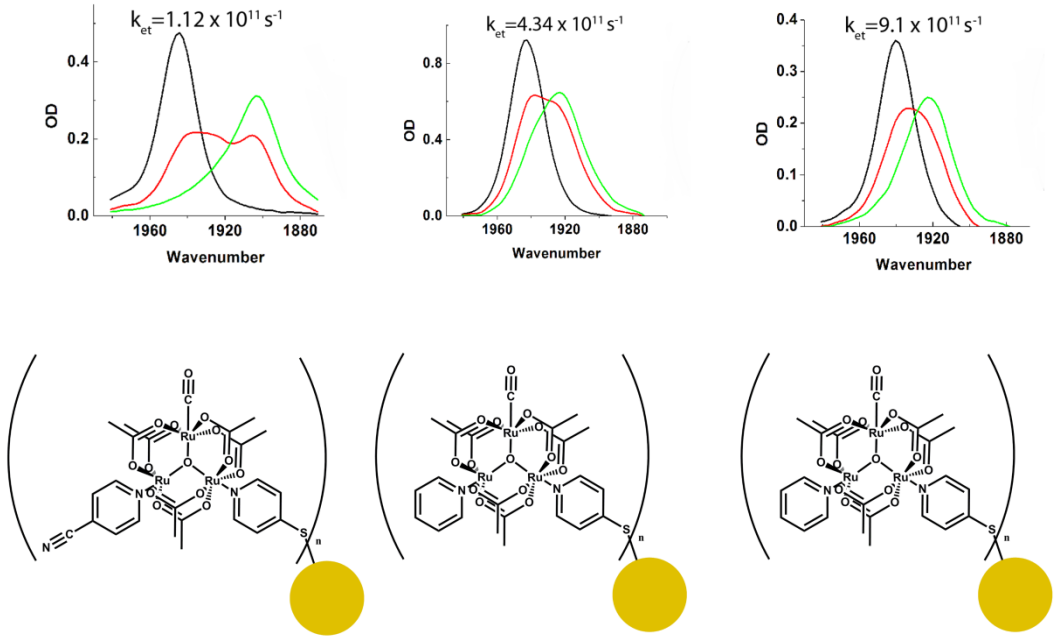

Figure 3.6. IR-spectroelectrochemistry responses of 0 (black trace), -1 (red trace),and -2 (green trace) states of Ru_3O clusters on Au nanoparticles in CH_2Cl_2. (a) 4-cyanopyridine (b) pyridine (c) 4-dimethylaminopyridine

Table 3.1. Simulated ground state electron transfer rates (s^{-1}) from experimental IR-SEC traces in varying solvents, for cpy, py, and dmap MV nanoclusters.

SOLVENT[a]	***CPY***	***PY***	***DMAP***
DCM	1.5×10^{11}	5.8×10^{11}	1.0×10^{12}
1,2 DCE	1.4×10^{11}	4.5×10^{11}	1.0×10^{12}
1,2 DME	0.8×10^{11}	2.0×10^{11}	0.8×10^{12}
THF	0.6×10^{11}	1.0×10^{11}	0.5×10^{12}

[a] Dichlormethane (DCM), 1,2 Dichloroethane (DCE), 1,2 Dimethoxyethance (DME), and Tetrahydrofuran (THF).

One of the synthetic side products that can be easily obtained by dissolution in acetonitrile, is the dipyridyl disulfide bridged molecular Ru_3O dimers. The presence (or absence) of these dimers in solution is readily checked by 2D DOSY NMR. Control experiments to determine that the IR-SEC responses observed correspond to nanocluster mixed valence assemblies, and not to exchange in molecular dimers were performed as previously reported.[20] Electron transfer rates in the disulfide bridged dimers are known to be slower than in the nanoclusters due to the poor conjugation over a relatively long bridging ligand.[20]

Previous work in our laboratory has shown that electronic communication between Ru_3O bridged units is controlled by the orbital overlap of the d-orbitals of the Ru clusters and the π^* orbitals of the bridging ligand.[12] More electron donating ancillary ligands were shown to raise the overall cluster d-orbitals relative to those of the bridging ligand. This improves electronic communication between clusters and the bridge by having favorable energetic alignment, which is reflected in faster ET rates in molecular dimers.[13,14,16,20,21,26] In the present study, the same effects are observed, as shown by the varying degrees of ν(CO) colascence in Figure 3.6. More electron donating substituents, those with the highest pyridine ligand pK_as, produce faster k_{et} rate constants. Although the trend in rates of ET with pyridine electron donor ability in a molecular mixed valence ion and the mixed valence NP's is the same, it does not reflect the same physical model. There is not a direct counterpart to the donor-bridge-acceptor orbital energy overlap of a molecular mixed valence complex in a metal NP assembly.

One possible explanation for the observed trend in ET rates is that, as the reduction potentials of the Ru_3O clusters attached to the Au NP's are shifted more negative by the stronger donor pyridine ligands, the density of states of the Au NP increase. Generally, as the density of states increases in energy, the distribution becomes more narrow, and this might suggest the opposite trend in ET rates.

It is known that the density of states of metallic Au near the Fermi energy level is expected to be mostly of *s* and *d* character, and that Au-S and delocalized *s* and *d* orbitals dominate transport at the molecule/surface interface.[27] An alternative explanation for the trends in ET rates observed, therefore, is that the effect of increased electron donor ability of the pyridine ancillary ligands on the Ru_3O clusters is to shift greater amounts of the unpaired spin density onto the mercaptopyridine ligand that attaches the Ru_3O cluster to the Au NP. This directly influences the orbital overlap at the pyS-Au interface, and would be expected to accelerate the rate of ET both in the NP, and out of it at the acceptor site.

The rate expression for symmetrical ground state electron transfer in mixed valence systems is given in eq. 2,

$$k_{ET} = \kappa \nu_n exp\left[-\frac{\Delta G_\lambda^* - H_{AB} + \frac{H_{AB}^2}{4\Delta G_\lambda}}{RT}\right] \qquad (2)$$

where κ is the adiabaticity factor, which is assumed to be 1 in the adiabatic limit, ν_n the nuclear frequency factor, H_{AB} the electronic coupling, and ΔG^*_λ the thermal activation energy barrier.

The thermal activation energy barrier depends on the reorganization energy, λ, and the electronic coupling as shown in Eq. 3.

$$\Delta G_{\lambda}^{*} = (\lambda - 2H_{AB})^2/4\lambda \quad (3)$$

The reorganization energy is a sum of the inner sphere and outer sphere contributions. (4)

$$\lambda = \lambda_i + \lambda_o$$

The inner sphere reorganization energy depends on molecular vibrations, while the outer sphere reorganization energy is controlled by the properties of the solvent.

$$\lambda_o = e^2 \left(\frac{1}{2a_1} + \frac{1}{2a_2} - \frac{1}{r}\right)\left(\frac{1}{\varepsilon_{op}} - \frac{1}{\varepsilon_s}\right) \quad (5)$$

Where a_1 and a_2 are the molecular radii of spheres enclosing the redox sites, *e* is the unit electron charge, and *r* is the internuclear distance. [28]

The outer sphere reorganization energy is dictated by the optical and static dielectric, as in the Marcus dielectric continuum model.[2-4] The solvent is considered a structureless continuum, which includes the effects of solvent nuclear rearrangement upon ET, $(1/\varepsilon_{op} - 1/\varepsilon_s)$. [29,30]

The pre-exponential portion of the rate expression, ν_n includes all of the nuclear frequencies modes (complex and solvent) that are involved in the ET reorganization energy. Bond length and angle adjustment is usually fast (10^{13}-10^{14} s^{-1}) but solvent motions are relatively slow (10^{11}-10^{12} s^{-1}), in the right timescale to directly affect ET rates.[26,31] In highly coupled systems solvent dynamics, especially

solvent inertial response times are heavily weighted in ν_n, and have been shown to strongly correlate with Maroncelli's t_{1e}, the solvent relaxation time.[32]

3.3 Solvent effects on mixed valence complexes

As shown in Table 1, it is immediately apparent that solvent plays an important role in ground state ET rates in the systems presented here. It is known that there is a strong dependence of the electron transfer lifetimes with solvent parameters in nearly barrierless ultrafast electron transfer at the mixed valence II/III class borderline.[6,16,33] Some of these studies were repeated for the mixed valence nanoclusters to understand the relationship of solvent dynamics (time dependent) and thermodynamics (time independent) on electron transfer rates in these systems.

The first parameter considered is the Pekar factor[30], which is important because it is the variable portion of the outer sphere solvent reorganization energy and is commonly used to represent the Marcus dielectric continuum.[2]

Table 3.2. Pekar factor values for the four solvents used in this study.

SOLVENT	***PEKAR FACTOR***
THF	0.373
DCM	0.381
1,2 DME	0.384
1,2 DCE	0.386

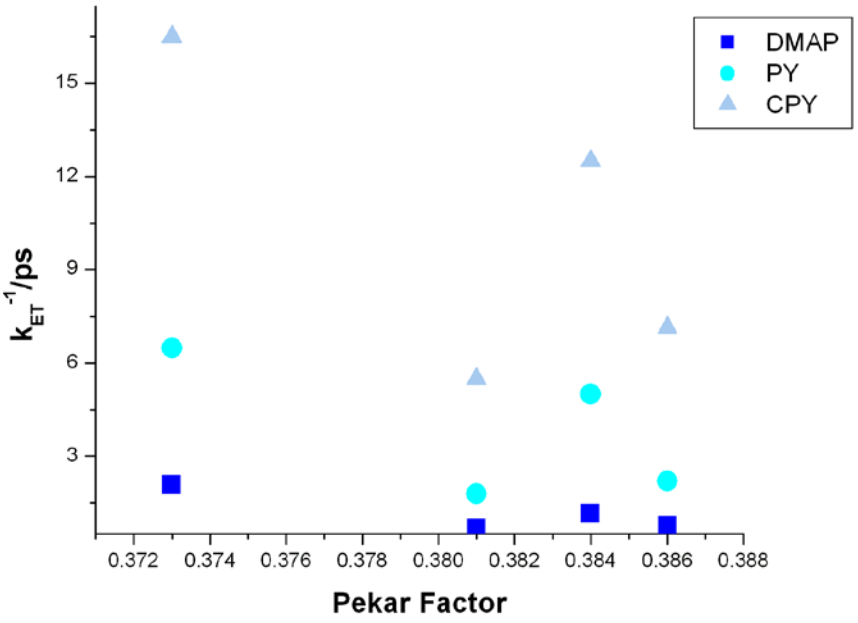

Figure 3.7. Plot of the Pekar factor ($1/\varepsilon_{op}$-$1/\varepsilon_s$) for the solvents used in this study, the variable portion of the outer sphere reorganization energy, λ_o, versus ET lifetimes, k_{ET}^{-1}, for the complexes used, 4-cyanopyridine (triangles), pyridine (circles), and 4-dimethylaminopyridine (squares).

From the plot of electron transfer lifetimes vs. Pekar factor it can be concluded that there is no clear correlation between solvent thermodynamics and observed electron transfer rates.

Solvent dynamics parameters should also be taken into consideration when considering solvent dependence of electron transfer in mixed valence Ru_3O clusters where rates of ET approach the ps timescale. [16,33] The principal moment of inertia in the x-direction (I_x) is often relevant in solvent dynamics when discussing intramolecular electron transfer in bridged ruthenium systems.[16,33] I_x correlates

strongly with Maroncelli's t_{1e},[32] the solvent inertial response time,[16] and can easily be calculated using Chem 3D.[34] Inertial parameters address the rotational component of the solvent, and provide information about the dipole reorientation upon ET. I_x describes the rotation along the x-axis, or the axis with the lowest rotational moment of inertia.

Table 3.3. Calculated[34] principal moment of inertia in the x-direction (I_x) for the solvent used in this study.

SOLVENT	$\boldsymbol{I_x}$
THF	71
DCM	16.2
1,2 DME	29.1
1,2 DCE	17.6

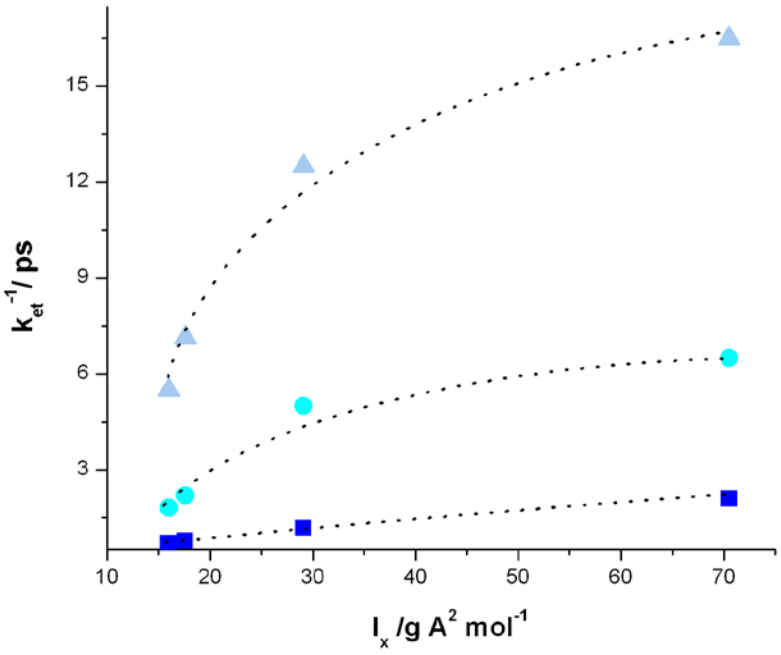

Figure 3.8. Plot of the principal moment of inertia, I_x, the variable portion of the outer sphere reorganization energy, λ_o, for the solvents used in this study versus ET lifetimes, k_{ET}^{-1}, for the complexes used, 4-cyanopyridine (triangles), pyridine (circles), and 4-dimethylaminopyridine (squares).

It can be clearly noted that there is a strong relationship between I_x and observed electron transfer lifetimes. These solvent dynamics parameters are known to be on the vibrational picosecond timescale, further supporting the simulated ground state electron transfer rates obtained from the dynamic coalescence of ν(CO) from the IR-SEC responses of the Ru_3O-NP nanoclusters.

Larger solvent molecules having large inertial response times do not effectively penetrate between Ru_3O clusters and the NP surface, therefore exerting less control on ET rates and effectively becoming decoupled. This is clearly

observed in the plateau between solvent inertial response time and electron transfer lifetimes, in Figure 8.

3.4 Conclusions

The systems presented here are examples of mixed valence supramolecular structures that can transfer electrons over distances up to 4nm, at ultrafast rates and with extremely high efficiency.

Using IR-SEC responses of mixed valence Ru_3O clusters bound to Au nanoparticles ET rates were shown to be at the picosecond timescale. Evidence of ultrafast, picosecond ground state electron transfer across a nanoparticle interface had been previously reported and discussed in chapter 2[20], but here we expanded the investigation of these systems by reporting the effects on ET of ancillary ligand substitution and solvent dynamics dependence. The ancillary pyridyl ligand electron donating ability correlates well with increased electron transfer rates, as noted by 4-dimethylaminiopyridine (dmap) having the fastest rate of exchange for the systems considered in this study. The trend in rates of ET with ancillary pyridine ligand dmap > py> cpy is interpreted as a result of the transfer of greater amounts of spin density onto the mercapto pyridine ligand that attaches the Ru_3O cluster to the Au NP. This is suggested by the increased coalescence of the ν(CO) bands, serving as further evidence that the electron transfer event is indeed ultrafast, and occurs on the vibrational (picoseconds) timescale. Along with ancillary ligand substitution, solvent effects were also probed in order to discern what parameters govern ET in nanocluster supramolecular systems. Although we report a NP size of 4nm, the

actual ET distance is not known, and further research is ongoing to elucidate the ET pathway and distance more precisely.

Solvent dynamics, rather than solvent thermodynamics were found to strongly influence the rates of exchange in the Ru_3O clusters bound to NPs. The solvent principal moment of inertia, I_x , showed the strongest correlation with the observed ET lifetimes in the various solvents studied. This is significant because the inertial parameter describes the rotation of the solvent about the x-axis, and provides information about the dipole reorientation upon ET. Solvent size is also found to be critical in controlling ET rates in nanocluster systems. Large solvent molecules do not effectively penetrate between the Ru_3O clusters and the NP surface, effectively decoupling the charge transfer between the two. The rate expression for ground state ET of mixed valence nanocluster systems with small or negligible barriers to ET is found to be completely governed by solvent modes. These solvent modes are strongly weighted in the pre-exponential factor, ν_n, highlighting the importance of solvent dipolar reorientation times and solvent size in long range ET.

Much like in nature's systems[35], this study is an example of efficient long range ET across a NP interface, and illustrates that fast charge transfer over large distances is possible when the couplings are optimized.

3.5 Experimental

General

All chemicals were used as received unless otherwise noted. Solvents used in electrochemistry and spectroscopy were sparged with argon and dried over alumina. Elemental analysis was performed by Numega Labs in San Diego, CA.

Synthesis and characterization

$[Ru_3O(OAc)_6(CO)(cpy)(dpyS)]$ was prepared using a previously reported method.[20] Briefly, $[Ru_3O(OAc)_6(CO)(cpy)(H_2O)]$ was synthesized as described previously,[11] and purified by chromatography. $[Ru_3O(OAc)_6(CO)(cpy)(H_2O)]$ (0.150 mmol) was stirred in 25 mL CH_2Cl_2. 4-4'-dipyridyldisulfide (10 eq.) was added as a solid and the reaction was allowed to stir for 48 hours. The reaction was taken to dryness on a rotary evaporator. The cluster was redissolved in 10 mL CH_2Cl_2 and filtered through celite to remove excess solid 4-4'-dipyridyldisulfide. The product, $[Ru_3O(OAc)_6(CO)(cpy)(dpyS)]$, was precipitated by addition of excess hexanes, filtered and washed with hexanes, 30mL, then dried *in vacuo* for 8 hrs.

^1H NMR (500 MHz, δ): ppm 9.04 (d, 2 H), 8.78 (d, 2 H), 8.46(d, 2 H), 8.21 (d, 2 H), 7.63 (d, 2 H), 7.11 (td, 2H), 1.95 (s, 6 H), 1.91 (s, 6 H), 1.70 (s, 6 H). UV/vis ($CHCl_3$) nm 280, 456, 610. IR cm^{-1} (CH_2Cl_2): 2241(m), 1951, 1711 (s), 1602, 1569, 1450 (s), 1420, 1350. Elemental analysis: Calc. for $Ru_3O(OAc)_6(CO)(cpy)(dpyS)$ $C_{29}H_{30}N_2O_{14}Ru_3S_2$ C 35.22; H 3.05; N 5.48. Found C 35.41; H 3.23; N 5.76 .

$[Ru_3O(OAc)_6(CO)(py)(dpyS)]$ was prepared in identical fashion as $[Ru_3O(OAc)_6(CO)(cpy)(dpyS)]$

^{1}H NMR (500 MHz, δ): ppm 9.02 (d, 2 H), 8.47 (d, 2 H), 8.14(d, 2 H), 8.07 (d, 2 H), 7.64 (m, 2 H), 7.12 (m, 2H), 2.35 (s, 6 H), 1.84 (s, 6 H), 1.56 (s, 6 H). UV/vis ($CHCl_3$) nm 278, 440, 610. IR cm^{-1} (CH_2Cl_2): 2931, 1945, 1611, 1605, 1578, 1434, 1412, 1349, 1092.

$[Ru_3O(OAc)_6(CO)(dmap)(dpyS)]$ was prepared in identical fashion as $[Ru_3O(OAc)_6(CO)(cpy)(dpyS)]$.

^{1}H NMR (500 MHz, δ): ppm 9.01 (d, 2 H), 8.92 (d, 2 H), 8.60(d, 2 H), 8.09 (d, 2 H), 7.53 (d, 2 H), 7.16 (td, 2H), 3.31 (s,6 H, DMAP-CH_3), 2.35 (s, 6 H), 2.04 (s, 6 H), 1.77 (s, 6 H). UV/vis ($CHCl_3$) nm 280, 405, 608. IR cm^{-1} (CH_2Cl_2): 1950, 1711, 1586, 1546, 1442, 1420, 1350.

Nanoclusters

The nanoclusters were synthesized using an updated version of a method previously reported.0.200 g of $HAuCl_4$ is dissolved in water (30 mL) and mixed with the phase transfer reagent tetraoctylammonium bromide (80 mL, 0.05 M) in toluene. The solution is stirred vigorously for 15 minutes until the organic layer turns a deep burgundy red, indicating that all of the gold colloid has been transferred to the organic phase. The organic phase is extracted with a separatory funnel. To the organic phase, the desired Ru_3O monomer (20 mg) and an alkanethiol (1:1 ratio) if a mixed monolayer is preferred, are then added over a period of 2 minutes. An aqueous $LiBH_4$ (25 mL, 0.4 M) or $NaBH_4$ (25 mL, 0.4 M) solution is then added

dropwise while stirring. (Note: The $LiBH_4$ is preferred for reducing the disulfide). The solution is stirred for an additional 12 hrs. The solvent is evaporated to 10 mL. Ethanol (400 mL) is added to induce precipitation of the product. The solution is placed in a freezer overnight to induce precipitation of the product. The nanoclusters are then filtered over a fine porosity glass filter, washed copiously with about 500 mL of ethanol, followed by a washing with approximately 100 mL of hexanes. The product is then dissolved in about 10mL of toluene and then reprecipitated. Washing extensively with ethanol and hexanes ensures the complete removal of any unbound thiol, Ru cluster, and tetraoctylammonium bromide. The nanoclusters are then collected by dissolution in minimal chloroform or unstabilized dichloromethane. The nanoclusters can be vacuum dried and stored away from light in a dessicator.

Spectroscopy

IR spectra were collected on a Bruker Equinox 55 FTIR spectrometer. IR-SEC was performed with a custom built reflectance cell mounted on a specular reflectance unit.[36]

TEM imaging

TEM images were taken using a FEI Tecnai G2 Sphera equipped with a LaB_6 filament operating at an accelerating voltage of 200 kV. The Tecnai G2 Sphera is equipped with a GatanUltrascan 1000 UHS CCD camera. The samples were prepared by evaporating one drop (3.5μL) of a dilute $CHCl_3$ solution of the nanoclusters onto a 3x3 mm carbon coated copper grid. Images were analyzed using Image J software, available from NIH[37].

2D DOSY NMR sample preparation and acquisition

DOSY NMR samples were prepared using a previously reported method modified for use with the nanoclusters.[22]

5mL of a 0.1 mM nanocluster solution was vacuum dried, 1mL of the preferred deuterated solvent was added, and then transferred to a 5mm medium walled NMR tube. Ferrocene was added, serving as the internal reference (approximately 0.1 mg). All data were acquired using a JEOL ECA 500 MHz spectrometer equipped with an inverse-geometry broadband NMR probe and processed using JEOL's Delta software[38]. Exponential decays in the acquired DOSY data sets were fit using the CONTIN[39] method.

Electrochemical Measurements.

Electrochemistry was performed with a BAS Epsilon potentiostat in dried deoxygenated CH_2Cl_2 with 0.1 M tetrabutylammonium hexafluorophosphate (TBAH, recrystallized from MeOH and dried under vacuum at 80 °C) and 0.3-5 mM sample concentrations at a scan rate of 100 mV/s under N_2 atmosphere. The working electrode was a platinum disk (1.6mm diameter) or a glassy carbon disk (3.0mm diameter), the counter electrode a platinum wire, and the reference a Ag/AgCl wire.

3.6 Derivation of K_c and cluster per nanoparticle counts.

Derivation of K_c.

The comproportionation constant is a very important value for mixed valence complexes as it quantifies the thermodynamic stability of the mixed-valence ion. It is derived from the Gibbs Free Energy and its relationship with half cell potentials.

$$\Delta G^0 = -nFE - RTlnK$$

the equation can be rearranged to be

$$lnK = \frac{nF\Delta E_{1/2}}{RT}$$

and finally expressed as

$$K_c = e^{\frac{nF\Delta E_{1/2}}{RT}}$$

Ru_3O clusters per nanoparticle.

The cluster per nanoparticle question can be easily answered by using these two very simple methods. The first methods is based on calculations of nanoparticle sizes and surface area. The second is derived from a methods shown by Prashant Kamat and co-workers in *J. Phys. Chem. B* **2006** 110 (42), 20737-2074.

Method 1: Surface Area

Nanoparticle Size: 3.5-4 nm

NP surface area = 45-50 nm^2

SAM Nanoparticle Coverage = 50%

Surface Area of Ru_3O (from 2D NMR DOSY) = 1nm^2

TOTAL NUMBER of Ru_3O clusters per NP = **20-25**

Method 2: Approximation adapted from Kamat et al.

NP size = 4nm

No. gold atoms per NP = 2461

No. of gold atoms = $0.05 \times 10^{-3} \times 6.023 \times 10^{23} = 3.01 \times 10^{19}$ atoms

No. of gold clusters = $3.01 \times 10^{19} / 2461 = 1.22 \times 10^{16}$

For Ru_3O:

Ru_3O on NPs = 0.5μmol

No. of Ru clusters = $0.5 \times 10^{-6} \times 6.022 \times 10^{23} = 3.01 \times 10^{17}$molecules

No. of Ru clusters per nanoparticle = $3.01 \times 10^{17} / 1.22 \times 10^{16}$ = ***24 Ru_3O per nanoparticle***

Note: Much of the material for this chapter comes directly from a manuscript entitled "Ultrafast Electron Transfer Across a Gold Nanoparticle: Ancillary Ligand and Solvent Influences" by Gabriele Canzi and Clifford P. Kubiak, which has been published in *Journal of Physical Chemistry C,* **2012**, *116* (11), 6560-6566. The dissertation author is the primary author of this manuscript.

3.7 References

(1) Marcus, R. A. *Angewandte Chemie International Edition in English* **1993**, *32*, 1111.

(2) Marcus, R. A. *The Journal of Chemical Physics* **1956**, *24*, 966.

(3) Marcus, R. A.; Sutin, N. *Biochim Biophys Acta* **1985**, *811*, 265.

(4) Sutin, N. *Prog Inorg Chem* **1983**, *30*, 441.

(5) Kaim, W.; Klein, A.; Glöckle, M. *Accounts of Chemical Research* **2000**, *33*, 755.

(6) Robin, M. B.; Day, P. In *Advances in Inorganic Chemistry*; Emeléus, H. J., Sharpe, A. G., Eds.; Academic Press: 1968; Vol. Volume 10, p 247.

(7) Varma, C. M. *Reviews of Modern Physics* **1976**, *48*, 219.

(8) Creutz, C. In *Prog Inorg Chem*; John Wiley & Sons, Inc.: 2007, p 1.

(9) Creutz, C.; Taube, H. *Journal of the American Chemical Society* **1969**, *91*, 3988.

(10) Ward, M. D. *Chemical Society Reviews* **1995**, *24*, 121.

(11) Ito, T.; Hamaguchi, T.; Nagino, H.; Yamaguchi, T.; Washington, J.; Kubiak, C. P. *Science* **1997**, *277*, 660.

(12) Londergan, C. H.; Kubiak, C. P. *Chemistry – A European Journal* **2003**, *9*, 5962.

(13) Glover, S. D.; Goeltz, J. C.; Lear, B. J.; Kubiak, C. P. *Eur J Inorg Chem* **2009**, 585.

(14) Glover, S. D.; Goeltz, J. C.; Lear, B. J.; Kubiak, C. P. *Coordin Chem Rev* **2010**, *254*, 331.

(15) Glover, S. D.; Lear, B. J.; Salsman, C.; Londergan, C. H.; Kubiak, C. P. *Philos T R Soc A* **2008**, *366*, 177.

(16) Lear, B. J.; Glover, S. D.; Salsman, J. C.; Londergan, C. H.; Kubiak, C. P. *Journal of the American Chemical Society* **2007**, *129*, 12772.

(17) Pfennig, B. W.; Fritchman, V. A.; Hayman, K. A. *Inorg Chem* **2000**, *40*, 255.

(18) Ferretti, A.; Lami, A.; Ondrechen, M. J.; Villani, G. *The Journal of Physical Chemistry* **1995**, *99*, 10484.

(19) Goeltz, J. C.; Kubiak, C. P. *Journal of the American Chemical Society* **2010**, *132*, 17390.

(20) Canzi, G.; Kubiak, C. P. *Small* **2011**, *7*, 1967.

(21) Salsman, J. C.; Ronco, S.; Londergan, C. H.; Kubiak, C. P. *Inorg Chem* **2005**, *45*, 547.

(22) Canzi, G.; Mrse, A. A.; Kubiak, C. P. *The Journal of Physical Chemistry C* **2011**, *115*, 7972.

(23) Bond, A. M.; Henderson, T. L. E.; Mann, D. R.; Mann, T. F.; Thormann, W.; Zoski, C. G. *Analytical Chemistry* **1988**, *60*, 1878.

(24) Jiménez, A.; Sarsa, A.; Blázquez, M.; Pineda, T. *The Journal of Physical Chemistry C* **2010**, *114*, 21309.

(25) Schiffrin, D. J.; Sendroiu, I. E.; Mertens, S. F. L. *Phys Chem Chem Phys* **2006**, *8*, 1430.

(26) Glover, S. D.; Kubiak, C. P. *Journal of the American Chemical Society* **2011**, *133*, 8721.

(27) Basch, H.; Ratner, M. A. *J Chem Phys* **2003**, *119*, 11943.

(28) Demadis, K. D.; Hartshorn, C. M.; Meyer, T. J. *Chemical Reviews* **2001**, *101*, 2655.

(29) Demadis, K. D.; Hartshorn, C. M.; Meyer, T. J. *Chemical Reviews* **2001**, *101*, 2655.

(30) Pekar, S. *Zhurnal Eksperimentalnoi Teor. Fiz.* **1946**, *16*, 335.

(31) Kapturkiewicz, A. *Advances in electrochemical science and engineering*; Wiley-VCH, 1997; Vol. 5.

(32) Horng, M. L.; Gardecki, J. A.; Papazyan, A.; Maroncelli, M. *The Journal of Physical Chemistry* **1995**, *99*, 17311.

(33) Londergan, C. H.; Salsman, J. C.; Ronco, S.; Dolkas, L. M.; Kubiak, C. P. *Journal of the American Chemical Society* **2002**, *124*, 6236.

(34) CambridgeSoft; 12.0 ed.; CambridgeSoft: 2010.

(35) Ricks, A. B.; Solomon, G. C.; Colvin, M. T.; Scott, A. M.; Chen, K.; Ratner, M. A.; Wasielewski, M. R. *Journal of the American Chemical Society* **2010**, *132*, 15427.

(36) Zavarine, I. S.; Kubiak, C. P. *Journal of Electroanalytical Chemistry* **2001**, *495*, 106.

(37) Abramoff, M. D.; Magalhaes, P. J.; Ram, S. J. *Biophotonics International* **2004**, *11*, 36.

(38) JEOL; JEOL: Tokyo, 2006.

(39) Provencher, S. W. *Computer Physics Communications* **1982**, *27*, 229.

Chapter 4

Controlling the rate of electron transfer between QDs and Ru_3O clusters by tuning the chemistry of the interface

4.1 Introduction

After having shown that electron transfer and significant electronic coupling can be observed at a conducting metallic nanoparticle surface we looked at alternative nanoparticles, in particular semiconducting nanoparticles, to investigate how the presence of a bandgap affect supramolecular electron transfer. Nanoparticles are known to be either insulators, semiconductors, or conductors. An insulator has a bandgap between the valence and the conduction band that is large, too large for electrons to be promoted from the valence band to its conduction band. A semiconductor has a bandgap that is non-zero but is smaller than an insulator. In

fact, electrons can be readily promoted from the valence band to the conduction band. In a metallic conductor, the band gap is either extremely small, zero, or there is considerable overlap between the conduction and valence band, as depicted in Figure 4.1. Electrons in conducting materials can be injected freely in the conduction band.

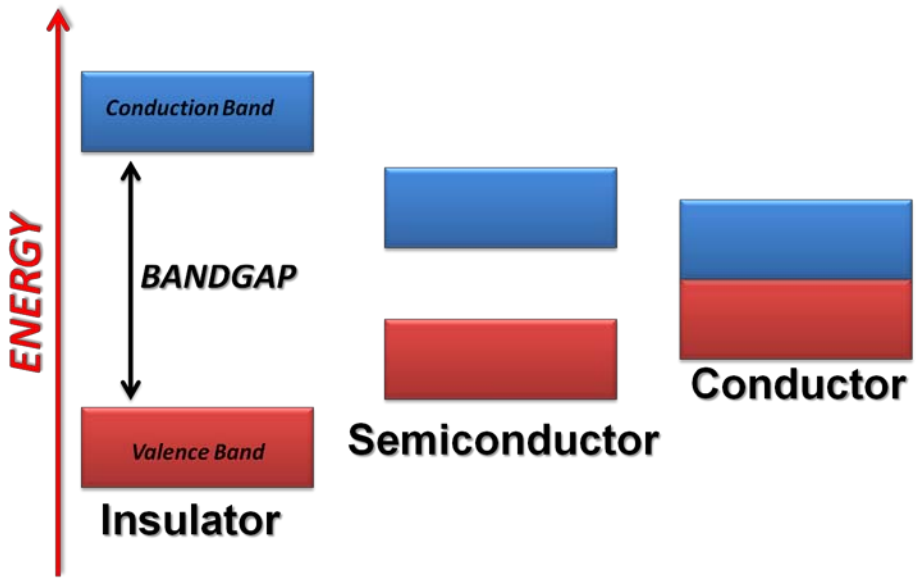

Figure 4.1. Schematic indicating the bandgap comparison between an insulator, semiconductor, and conductor.

With this in mind we started investigating at using semiconducting nanoparticles as the "bridge" in our nanocluster systems. At the same time, since we don't have easy access to a laser system, we started looking for possible collaborations where we could use a laser system to promote electrons from a semiconducting naoparticle to our Ru_3O clusters. The collaboration that made the

material used in this chapter possible came from my first attendance of the Electron Donor-Acceptor Interactions Gordon Research Conference. It was a hot day at Salve Regina University in Rhode Island, it was time for the students to give their poster presentation As I browsed other posters, one really caught my eye. Adam Morris-Cohen from Northwestern University was presenting some really interesting work on photoinduced ET between a quantum dot and methyl viologen. After a quick chat with Adam, where I explained our need for a collaboration to work on our idea, we decided to start this collaboration. We decided that not only did we want to clearly show the ET dynamics between the quantum dots (QDs) and the Ru clusters, but we also wanted to understand how functional groups, our "bridge" between the nanoparticle and cluster interface, affect the rates of charge separation and charge recombination. This chapter that follows is a results of this very fruitful collaboration and describes the dependence of the rate of photoinduced electron transfer (PET) from CdSe quantum dots (QDs, diameter = 2.4 nm) to oxo-centered triruthenium clusters (Ru_3O) on the structure of the chemical headgroup by which the Ru_3O clusters adsorb to the QDs. We synthesized two types of Ru_3O clusters, "nic-Ru_3O" and "thiol-Ru_3O"; the clusters are identical except that nic-Ru_3O adsorbs to the QD through a pyridine-4-carboxylic acid linkage, and thiol-Ru_3O adsorbs to the QD through a 4-mercaptopyridine linkage, Figure 4.2. The rate of solution-phase PET, as measured by transient absorption (TA) spectroscopy, is approximately seven times faster when the thiol-connected Ru_3O cluster is the electron acceptor than when the nic-Ru_3O is the acceptor. The energetic driving

force, measured by electrochemistry, and calculated reorganization energy for the PET processes are nearly identical for the two QD-Ru_3O complexes. We therefore attribute the difference in the PET rates of the two complexes to differences in the magnitude of donor-acceptor electronic coupling. Electronic structure calculations indicate that the shape of the electron-accepting orbital between the QD and Ru_3O cluster (specifically, the degree to which it delocalizes onto the bridging pyridine ligand) is modulated by the torsional angle of the bridging pyridine ligand, and that only certain geometries of the complex contribute to the overall electronic coupling for PET.

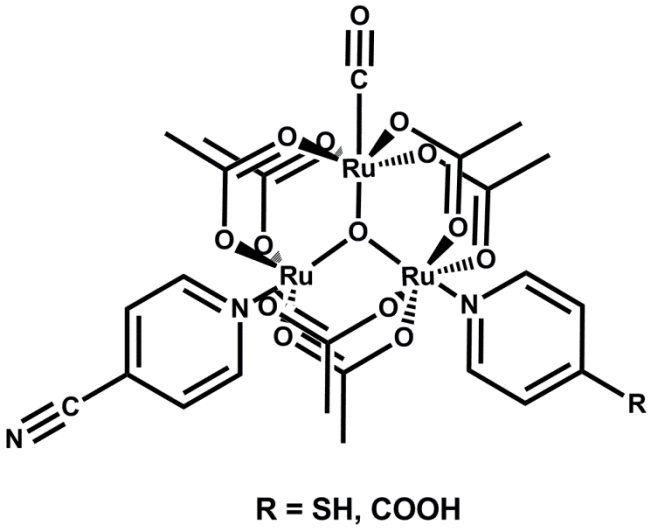

Figure 4.2. Chemical structure of the oxo-centered triruthenium clusters (Ru_3O) used in this study. The two clusters differ in fuctional group through which they adsorb to the surface of the QD. The ligands will be named "thiol-Ru_3O" for R = SH and "nic-Ru_3O" for R = COOH.

Hybrid systems comprising QDs and molecular catalysts are promising candidates for photo-catalytic applications because of the strong, broad, and size-tunable absorption of the QDs, and the catalytic activity toward target reactions of the transition metal complexes.[1-3] Application of these systems to catalysis requires that we understand which chemical features of the interface result in fast, high-yield electron exchange between the QD and catalyst components. Mechanistic analysis of PET in donor-acceptor systems requires accurate measurements of physical parameters such as the energetic driving force for the reaction, the energy required for nuclear reorganization of the redox moieties and surrounding medium, and the electronic coupling between neutral and charge-separated states. This analysis is complicated in QD-ligand systems, in general, because of the heterogeneity in adsorption geometries, the presence of a native ligand shell that provides a local dielectric environment that is different from that of the solvent, and the instability of QDs to precise electrochemical measurements of redox potentials. One strategy for developing a model for PET in QD-ligand systems that approaches the quantitative predictive ability of the Marcus equations for covalently-bound molecular donor-acceptor systems is to explore each relevant parameter systematically while holding all other variables in the system constant. Here, we compare PET rates for two different QD-ligand complexes in which the driving force for the PET reaction and the reorganization energy are nearly identical. We also measure and account for the surface coverage of Ru_3O clusters bound to the QD, and therefore ensure that any difference in PET rate constant between the two species does not arise due to a

difference in the number of available PET pathways. Several other groups have previously used Ru- and Re-centered transition metal complexes[4,5] as electron transfer partners in QD-ligand complexes, but our experimental design enables us, for the first time, to experimentally isolate and compare the effect of electronic coupling for two different ligands on the rate of PET across the QD-ligand interface. We show that the nanocrystal surface supports a range of conformations of the redox-active catalyst component, and the distribution of the donor-acceptor electronic couplings corresponding to these conformations affects the observed rate of interfacial PET.

Throughout this chapter we will refer to both of the oxo-centered triruthenium (Ru_3O) species as "clusters" and the QD-Ru_3O donor-acceptor pairs as "complexes".

4.2 Results and discussion

Absorption spectra of the Ru_3O clusters have two distinct bands, as shown in Figure 4.3. The lower-energy peak, centered at 596 nm for the thiol-Ru_3O cluster and 593 nm for the nic-Ru_3O cluster, corresponds to a metal-to-ligand charge transfer (MLCT) transition.[6-9] The higher-energy band, centered at 426 nm for thiol-Ru_3O cluster and 326 nm for the nic-Ru_3O cluster, corresponds to an intra-cluster charge transfer (ICCT) transition.[6-9] The maximum of the first excitonic peak in the absorption spectra of the QDs is at 505 nm, which corresponds to a QD diameter of 2.4 nm.[10] The absorption spectra of the mixtures of CdSe QDs and

Ru_3O clusters have a similar shape, but differ slightly in intensity (particularly at shorter wavelengths), compared to the sum of the individual absorption spectra of the isolated QDs and Ru_3O clusters. We attribute these intensity changes to changes in the absorptivity of the Ru_3O clusters upon adsorption induced by the different local dielectric environment near the surface of the QD.[11]

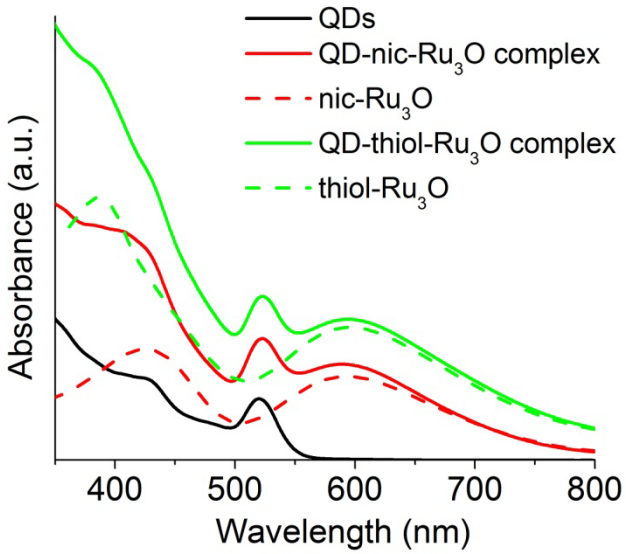

Figure 4.3. Ground state absorption spectra of CdSe QDs in $CHCl_3$ (d = 2.5nm, $2.7x10^{-5}$ M, black), thiol-Ru_3O clusters ($5.4x10^{-4}$ M, green-dashed), nic-Ru_3O clusters ($5.4x10^{-4}$ M, red-dashed) and mixtures of the thiol-Ru_3O or nic-Ru_3O clusters with the QDs at the same concentrations (green-solid and red-solid, respectively).

4.3 Photoexcitation of the QD induces electron transfer from the QD to the Ru_3O cluster.

Figure 4.4-A shows that adding Ru_3O clusters to solutions of QDs quenches the photoluminescence (PL) of the QD. Figure 4.4-B shows that, upon photoexcitation of the QDs to their first excitonic state, it is energetically feasible

for either the electron or the hole to transfer from the QD to the Ru_3O cluster. In this diagram, the energy levels of the Ru_3O cluster HOMO and LUMO are determined from electrochemistry and energy levels of the QD LUMO and HOMO (conduction and valence band-edges) are taken from literature values derived from cyclic voltammetry measurements of films of CdSe QDs.[12]

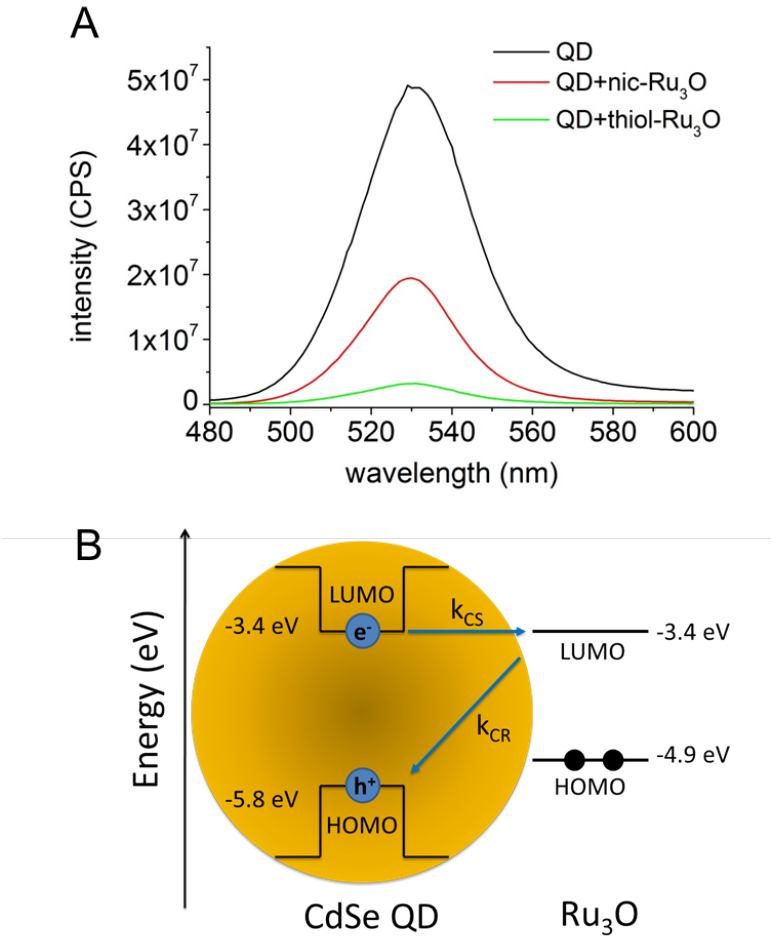

Figure 4.4. (A) Photoluminescence spectra of CdSe QDs in $CHCl_3$ excited at 450 nm (d = 2.5nm, $2.7x10^{-5}$ M, black), and solutions of same QDs after stirring for 30 min with either $5.4x10^{-4}$ M thiol-Ru_3O clusters (green) or $5.4x10^{-4}$ M nic-Ru_3O clusters (red). (B) Schematic diagram illustrating the charge separation (CS) and charge recombination (CR) processes that occur after generating a band-edge exciton in a CdSe QD.

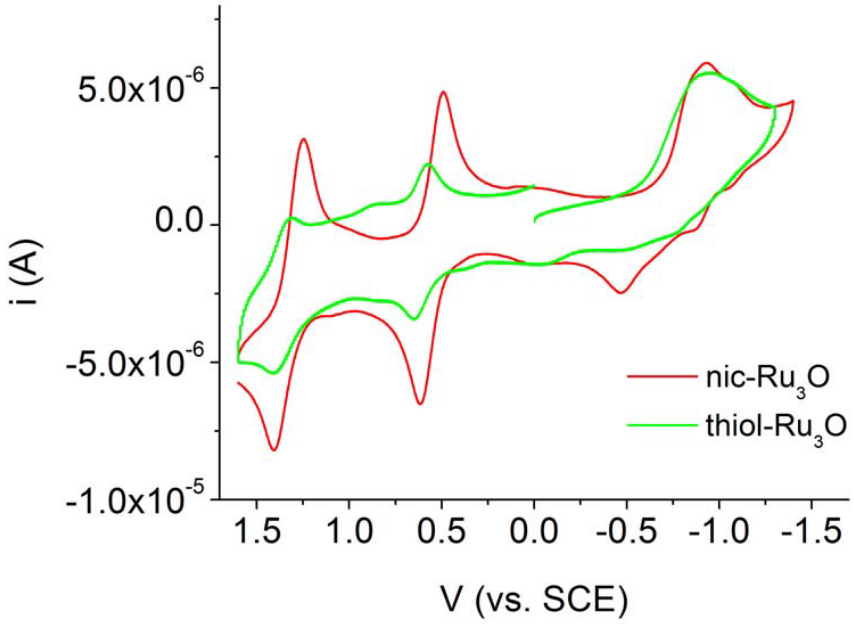

Figure 4.5. Electrochemical responses for the systems studied. The reduction of the clusters is nearly overlapping at -930mV vs. SCE.

There are two pieces of evidence that suggest the mechanism for PL quenching of the QD is electron transfer from the LUMO of the QD to the LUMO of the Ru_3O cluster (rather than hole transfer). (i) Figure 4.6 shows that addition of both the nic- and thiol-Ru_3O clusters induces recovery of the ground state bleach in the TA spectrum of the QD at a faster rate than it recovers in free QDs with no added Ru_3O clusters. The ground state bleach of CdSe QDs reflects the population of electrons in the $1S_e$ state and is mostly insensitive to the population of holes in the $1S_h$ state.[13,14] Recovery of the ground state bleach upon addition of the Ru_3O clusters indicates that the clusters facilitate depopulation of electrons from the $1S_e$ state and is therefore consistent with PET from the LUMO of the QD to the LUMO of the Ru_3O cluster. (ii) Addition of the Ru_3O clusters to QDs produces a new,

broad transient absorption between 550 nm and 700 nm in the visible region and another broad absorption centered at 1250 nm in the near-infrared region (NIR) for both the nic-Ru_3O and thiol-Ru_3O clusters (Figures 4.6-A, inset, and 4.6-B). The shape of the absorption band is different for the nic- and thiol- Ru_3O clusters in the visible region, but very similar for the two species in the NIR. Absorption spectra of Ru_3O clusters chemically reduced by decamethylcobaltocene (Figure 4.6) and spectra reported previously[15] shows these new peaks in the TA spectrum correspond to absorptions of the Ru_3O^- radical anion. We see no evidence of the radical cation of Ru_3O (the product of hole transfer) or the excited state of Ru_3O (the product of energy transfer) in the TA spectrum.

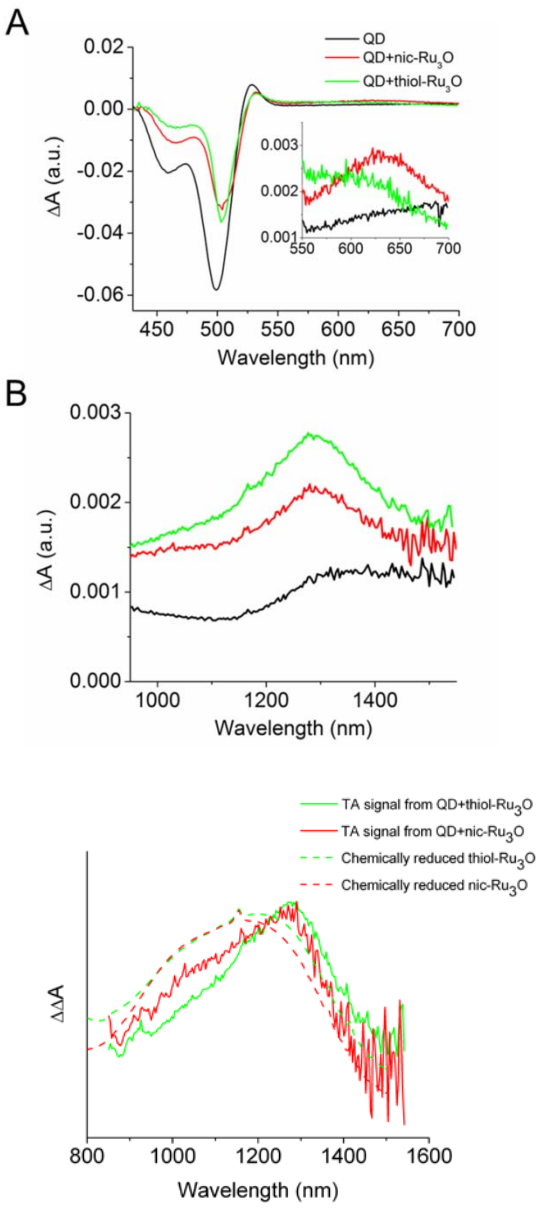

Figure 4.6. Transient absorption spectra of CdSe QDs (d = 2.5 nm, 3.0×10^{-5} M) in $CHCl_3$ 600 ps after photoexcitation (black), and of mixtures of the same QDs with the nic-Ru_3O (red) and thiol-Ru_3O (green) clusters, at a molar ratio of 20 clusters/QD. ***Inset*:** Zoomed in region of the photoinduced absorptions of the three samples. **(B)** Transient absorption spectra of the same samples as in **A** in the near-IR region of the spectrum, 100 ps after photoexcitation (top) and overlap between chemically reduced (using decamethylcobaltocene) NIR region of the clusters with TA results corresponding to reduced Ru_3O.

We note that, although we synthesized CdSe QDs so that the first excitonic peak in their absorption spectrum overlaps with the region of minimum absorption of the Ru_3O clusters, some Ru_3O clusters are inevitably photoexcited by the TA pump pulse. Figure 4.7 shows the results of control experiments, in which we measured the TA spectra of Ru_3O clusters photoexcited at a lower energy than the first excitonic peak of the QD (such that only the clusters, and not the QDs, are excited); these spectra show no signals indicative of electron transfer or other interactions between the excited Ru_3O cluster and the QD, so we can eliminate the contribution of incidentally excited Ru_3O clusters to the observed PET dynamics.

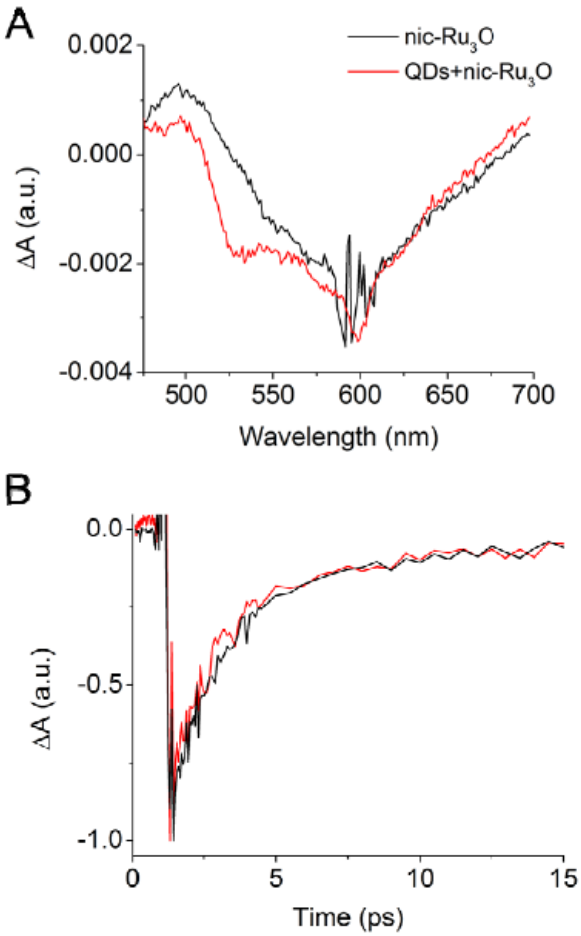

Figure 4.7. (A) Transient absorption spectra of 1.4×10^{-4} M nic-Ru_3O in $CHCl_3$ (black) and of the same clusters with added M CdSe QDs (d = 2.7 nm, 2.4×10^{-5}; red) 4.3 ps after photoexcitation. The bleach centered at 600 nm corresponds to the ground state bleach of the Ru_3O and the positive absorption at ~500 nm corresponds to absorbance by nic-Ru_3O*. The increased noise at 600 nm results from scattered pump light and the additional peak in the QD + nic-Ru_3O trace corresponds to bleaching of the QD via two photon absorption. **(B)** Kinetic traces of the same to samples from **(A)** taken at 585nm.

4.4 Extracting the intrinsic charge separation rates for the QD-Ru_3O complexes from the TA dynamics.

We monitored the dynamics of the PET process at 1150 nm within the absorption band of the radical anion of both Ru_3O clusters. We chose this

wavelength, instead of those within the broad transient absorption of Ru_3O^- between 550 nm and 700 nm or those within the ground state bleach of the QD, because we found that the NIR feature is least convoluted with other, non-PET-related dynamics.[16,17] Specifically, monitoring PET using bleach dynamics is non-ideal because, in order to extract the electron transfer rate constant from the bleach dynamics, one has to separate the dynamics of the PET process from the multiexponential dynamics of the intrinsic (QD-only) relaxation processes. Furthermore, pumping the sample at the band-edge exciton – which we did in order to eliminate the possibility of carrier-cooling affecting the PET process – makes it more difficult to extract quantitative kinetic information from the ground state bleach of the QD, because the signal from scattered pump light degrades the TA spectrum at that wavelength. The dynamics of the broad transient absorption of Ru_3O^- between 550 nm and 700 nm is even more difficult to deconvolute because it represents a mixture of the radical anion signal with signals from (i) the ground state bleach of the incidentally excited Ru_3O complexes, and (ii) the rise and decay of photoinduced intraband absorptions of excitonic carriers of the QD. Figure 4.8 contains kinetic traces from each of these features in the TA spectra of the QD-Ru_3O complexes. Despite the difficulty in quantifying the rate of PET from these two signals in the visible region, we observe that each signal qualitatively agrees with the kinetic traces of the Ru_3O^- signal at 1150 in the NIR.

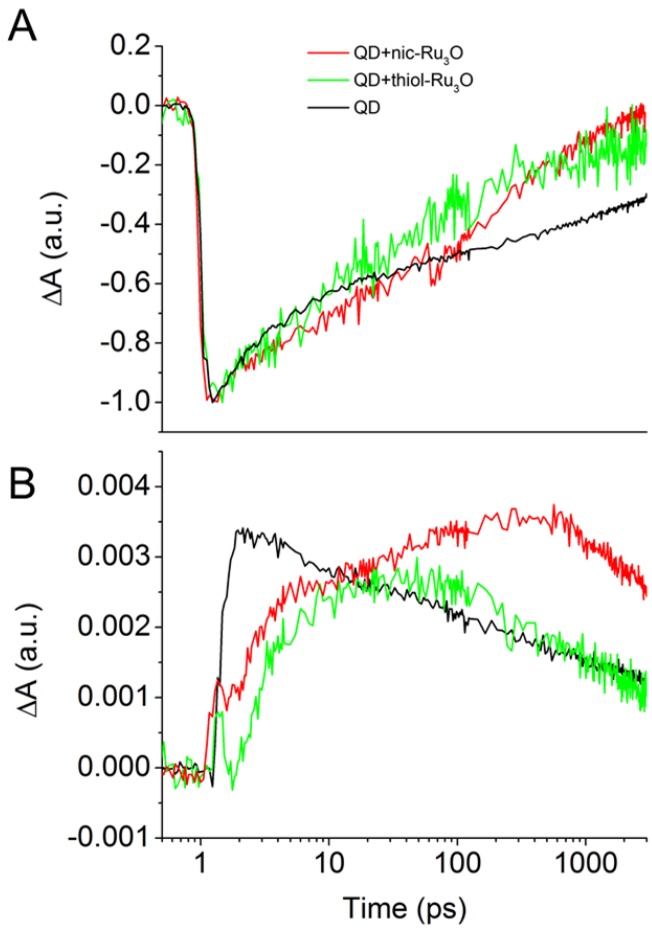

Figure 4.8. (A) Transient absorption kinetic traces, at a probe wavelength of 500 nm, of 3.0×10^{-5} M CdSe QDs (d = 2.4 nm) in $CHCl_3$ (with no added Ru_3O) after photoexcitation (black), and traces for a sample of the same QDs with the nic-Ru_3O (red) and thiol-Ru_3O (green) clusters added at a ratio of 20 clusters/QD. The kinetic traces are normalized to their peak minimum at t_0. Electron transfer induces an additional, fast recovery of the ground state bleach. **(B)** Same as (A) but at 640 nm illustrating the dynamics of the new photoinduced absorption.

To isolate the PET dynamics from the QD excitonic carrier dynamics at 1150 nm, we acquired kinetic traces at this wavelength for samples of the QD-Ru_3O complexes and samples of the QDs without added Ru_3O. We first normalized these kinetic traces to their amplitudes at zero delay (t_0) after the laser pump pulse. This

normalization is necessary, even though all samples contain the same concentration of QDs and are excited using the same pump fluence, because absorption by the Ru_3O clusters at the pump wavelength leads to a slightly smaller population of excited QDs in samples containing Ru_3O clusters than in those without Ru_3O clusters. Figure 4.9 shows these normalized kinetic traces. The dynamics of the three systems at 1150 nm are nearly identical for the first few picoseconds after photo-excitation; the dynamics on this short timescale primarily reflect relaxation of the excitonic hole within the QDs,[16] and are not perturbed by the presence of the Ru_3O clusters. We then subtracted the kinetic trace for the free QD sample from the kinetic traces for the QD-Ru_3O complexes. In doing this subtraction, we assume that the only mechanism by which the Ru_3O cluster perturbs the carrier dynamics of the QD is by providing a charge transfer pathway for the electron, and that adsorption of the cluster and the PET process does not affect the intrinsic hole dynamics. This assumption is reasonable because, in CdSe QDs, the hole dynamics are largely complete in the first five ps.[16] Figure 4.9 shows the difference between the kinetic traces of the QD-only samples and the samples with QDs and nic-Ru_3O or thiol-Ru_3O in Figure 4.9; these "difference" traces track the formation of the nic-Ru_3O^- and thiol-Ru_3O^- anions after photoexcitation of the QD. The rate of formation of the Ru_3O^- radical anion is the observed rate of charge separation (CS) for the QD-Ru_3O complex.

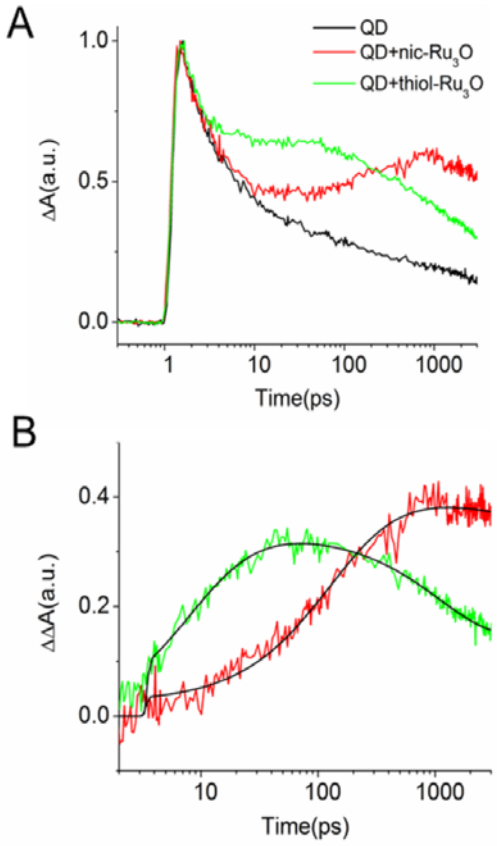

Figure 4.9. Transient absorption kinetic traces, at a probe wavelength of 1150 nm, of 3.0×10^{-5} M CdSe QDs (d = 2.4 nm) in $CHCl_3$ (with no added Ru_3O) after photoexcitation (black), and traces for a sample of the same QDs with the nic-Ru_3O (red) and thiol-Ru_3O (green) clusters added at a ratio of 20 clusters/QD. The kinetic traces are normalized to their peak maxima at t_0. Formation of the Ru_3O^- radical anion produces a rise component in the kinetic trace that competes with the decay of the QD feature. **(B)** Transient absorption kinetics for the Ru_3O-nic and Ru_3O-thiol samples after subtraction of the kinetic trace for the QD-only sample (black trace figure 5A). The black lines are the best fits to these "difference kinetics" using equation 4. From these fits, the values of k_{CS} (rate constant for formation of Ru_3O^-) are 32.5 ps for QD-thiol-Ru_3O and 242 ps for QD-nic-Ru_3O.

We then must consider that the observed rate constant of CS for a QD-ligand complex is linearly proportional to the number of adsorbed charge-accepting

ligands.[18,19] Consequently, in an ensemble of QDs where there are many subpopulations of QDs, each containing a different number of adsorbed Ru_3O clusters, the intensity of the Ru_3O anion signal as a function of time, *I(t)*, is given by eq 1.[18,20-22] Each exponential function within the sum in eq 1 corresponds to

$$I(t) = \sum_{m=0}^{N} A_m e^{-mk_{CS,int}t} \quad (1)$$

a subpopulation of the ensemble with *m* adsorbed Ru_3O clusters. The prefactor A_m gives the probability of encountering a QD with *m* adsorbed ligands, and $k_{CS,int}$ is the intrinsic rate constant of charge separation – that is, the rate constant for a single QD donor-single cluster acceptor pair.[18] The intrinsic rate constant is the quantity we need to compare the efficiencies of CS for the two QD-Ru_3O complexes because its value is not a function of the number of adsorbed Ru_3O clusters. The set of A_m in eq 1 have the form of the binomial distribution, eq 2.[20,23] In eq 2, θ is

$$A_m = \binom{N}{m} (\theta)^m (1-\theta)^{N-m} \quad (2)$$

the mean fractional surface coverage of Ru_3O clusters on the QD, and *N* is the number of available surface sites on the QD to which a Ru_3O cluster can absorb. Substituting eq 2 into eq 1 and taking the sum from *m = 0* to *m = N* yields eq 3. Equation 3 accounts for the fact that the

$$I(t) = (1 + (e^{-k_{CS,int}t} - 1)\theta)^N \quad (3)$$

observed CS dynamics in an ensemble measurement of QD-ligand complexes depends on the fractional surface coverage of ligands on the QD. Equation 3 is a fitting function for the CS portion of the kinetic trace at 1150 nm (the formation of

the Ru_3O^- feature). In order to describe the entire kinetic trace, which includes the instrument response, CS, and charge recombination (CR), we use eq 4. In eq 4, *IRF* is the instrument response function (here the error function), A_{CS}

$$I(t) = IRF(A_{cs}(1 + (e^{-k_{CS,int}t} - 1)\theta)^N + A_{CR}e^{k_{CR}t})$$

is the amplitude for the function representing the CS process, A_{CR} is the amplitude for the component representing the CR process, and k_{CR} is the CR rate constant. The CR rate constant does not need to be treated statistically because each Ru_3O cluster is adsorbed to only one QD and thus there is only one possible pathway for CR.

One of the input parameters in the fitting function in eq 4 is θ, the fractional surface coverage of each Ru_3O cluster on the QDs at a given added concentration of cluster. We have shown previously that, for QD-ligand complexes that undergo photoluminescence (PL)-quenching PET much faster than the rate of radiative recombination (as is the case here), the PL of the QD can be used as a quantitative probe of the concentration of quenchers on the surface of the QD.[18,23] Using three separate PL measurements on samples prepared identically to those we measured in the TA experiment, and a procedure described elsewhere,[23] we find that there are an average of 2.9 thiol-Ru_3O clusters adsorbed per QD and an average of 1.1 nic-Ru_3O clusters adsorbed per QD at the concentrations of each component of the mixtures that we study with TA. We calculate that there are roughly 100 surface sites per QD; ψ is therefore 0.029 and 0.011 for the thiol-Ru_3O and nic-Ru_3O, respectively. Inserting these values of ψ and N = 100 into eq 4, and using this equation to fit the

PET kinetics, we ensure that we determine the intrinsic (surface coverage-independent) rate constant for CS for each complex.

The intrinsic rate of PET from the QD to the Ru_3O cluster is seven times faster through the thiolate linkage than through the carboxylate linkage. We fit the kinetic traces for the formation and decay of Ru_3O^- for both QD-Ru_3O complexes (Figure 4.7) to eq 4 to obtain the photoinduced CS and CR rates for the QD-Ru_3O systems. Data from three separately prepared samples, each measured either two or three times on a single day, yield the intrinsic time constants for CS: $k_{CS,int}$ = 29 ± 6 ps for the QD-thiol-Ru_3O complex, and $k_{CS,int}$ = 210 ± 40 ps for the QD-nic-Ru_3O complex. The fit to the kinetic trace for the QD-thiol-Ru_3O complex also yields k_{CR} = 800 ± 200 ps, while the CR process for the QD-nic-Ru_3O complex is too slow to measure accurately with our 3 ns time window. The rate of CS is therefore approximately a factor of seven greater for the QD-thiol-Ru_3O complex than for the QD-nic-Ru_3O complex, and the rate of CR is measurably (although not quantifiably) faster for the QD-thiol-Ru_3O complex than for the QD-nic-Ru_3O complex.

4.5 Discussion of the difference in PET rates between the QD-thiol-Ru_3O and the QD-nic-Ru_3O complexes.

In the Marcus formalism, the rate of PET depends on (i) the driving force for the reaction, (ii) the intramolecular and solvent reorganizational energy for charge separation, and (iii) the electronic coupling between the pre-CS and post-CS states. The reduction potential versus Ag/AgCl in dichloromethane is -931 mV for the nic-

Ru_3O cluster and -930 mV for the thiol-Ru_3O cluster, as shown in Figure 4.5. The driving force for PET must therefore be the same for both complexes (~10 meV) because other contributions to the change in free energy—such as the excited state oxidation potential of the QD and the dielectric environment—are also nearly identical for the two systems. We determined the reorganization energies of the two Ru_3O clusters by calculating the difference between the energy of the geometry-optimized cluster anion and the single-point energy of the cluster anion at the optimized neutral geometry using density functional theory (B3LYP, def2-DZVP). We found that they are -0.170 eV and -0.185 eV for the nic- and thiol-functionalized Ru_3O clusters, respectively. The semiclassical Marcus equation[24,25] predicts that, for a driving force of 10 meV at room temperature, the 15-meV difference in reorganization energy between the two Ru_3O clusters only results in a factor of 1.2 increase in PET rate constant on going from the nic to the thiol-linked system. The observed difference in rate constants is a factor of seven. We measured the PET rates for both complexes in the same solvent, using the same synthetic batch of QDs that were purified and prepared for measurement using the same procedure, so additional contributions to the reorganization energy from the QD, native ligands and solvent should be identical for the two systems.

As we can rule out driving force, reorganization energy, and surface coverage as explanations for the difference in the PET rate between the two Ru_3O clusters, we hypothesize that it is a difference in the donor-acceptor electronic coupling that results in the higher PET rate for the QD-thiol-Ru_3O cluster than for

the QD-nic-Ru_3O cluster. The donor-acceptor electronic coupling is sensitive to the degree of orbital overlap (either direct or via a molecular bridge) between the donor orbital on the QD and the acceptor orbital on the Ru_3O cluster. We first identified the lowest unoccupied molecular orbital of each of the QD-Ru_3O complexes that is localized on the Ru_3O clusters; this orbital is the LUMO + 3 of the QD-thiol-Ru_3O complex and the LUMO+1 of the QD-nic-Ru_3O complex (lower-energy LUMOs are localized on the QD). This orbital is the electron-accepting orbital for the complex. We then noted that the shape of this orbital depends sensitively on the torsional angle, ψ, of the O-Ru-N-C bond connecting the Ru_3O core of the cluster with either the pyridine-4-carboxylic acid or 4-mercaptopyridine bridging ligand. In both the nic and thiol complexes, when the pyridine ligand is coplanar with the three Ru atoms, the acceptor orbital extends over the Ru_3O core to the edge of the pyridine ligand at the point of attachment between the Ru_3O cluster and the QD – that is, it is delocalized over the core and the bridging ligand (Figure 4.10, left column). In this coplanar geometry, the acceptor orbital directly overlaps with the donor orbital (the LUMO of the QD). When the plane of the pyridine ligand is perpendicular to the plane of the three Ru atoms, the acceptor orbital is localized in the core of the Ru_3O cluster, Figure 4.10, right column. In this "twisted" geometry, electron transfer must occur by superexchange (or indirect tunneling), as the acceptor orbital does not directly overlap with the donor orbital, but rather couples to it through the lowest-lying orbital located on the bridging ligand. The torsional angle ψ therefore modulates the donor-acceptor electronic coupling of the QD-Ru_3O complex.

Calculation of the geometry-optimized 1-D torsional potential energy surfaces (TPES) of the two clusters adsorbed to the surface of a truncated QD shows that the coplanar (ψ = 43°) and twisted (ψ = 132°) conformations are the two minimum-energy geometries of both the QD-nic-Ru_3O and QD-thiol-Ru_3O complexes (Figure 4.11). The energy barrier for interconversion of these two conformations is 4 - 5 k_BT, which corresponds to a time constant of >10 ns for interconversion through rotation around the O-Ru-N-C bond. We can therefore conclude that the complexes are "frozen" in either the coplanar or twisted conformation during the PET process. In addition to any energy barrier for PET due to reorganization of nuclei, PET in the twisted conformation must occur by superexchange tunneling through the energetic barrier presented by the bridging ligand.[9] The height of this tunneling barrier is approximately the energy of the MO that is localized on the bridging ligand (relative to the energies of the electron donor and acceptor orbitals, which are within 10 meV of each other): ~1.5 eV for PET within the QD-thiol-Ru_3O complex, and ~0.8 eV for PET within the QD-nic-Ru_3O-QD complex. Given the height and length of these tunneling barriers, simple WKB tunneling theory PET in the coplanar conformation will be a factor of 10^3 - 10^5 faster than PET in the twisted conformation for the complexes. We can therefore reasonably conclude that the single distributed time constant we observe for formation of the cluster radical anion is that for PET in the coplanar conformation of both complexes, and that the difference in observed PET rates for the nic and thiol

complexes is due to a difference in electronic coupling magnitude in the coplanar conformation.

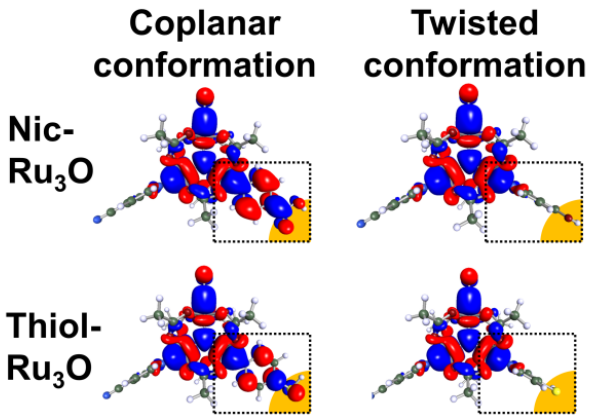

Figure 4.10. Electron-accepting orbitals of the QD-nic-Ru_3O and QD-thiol-Ru_3O complexes, where the QD is represented by an orange quarter-circle for clarity. The orbital isodensity surfaces are for electron density 0.01. ***Left:*** Orbital maps for the complexes in the "coplanar" geometry, where the bridging pyridine moiety is co-planar with the three Ru atoms and the electron-accepting orbital is delocalized across the central Ru_3O cluster as well as the rings of the functionalized pyridine ligands. ***Right*****:** Orbital maps for the complexes in the "twisted" geometry, where with the pyridine moiety perpendicular to the plane of the three Ru atoms, and the electron-accepting orbital does not extend over the pyridine ligands.

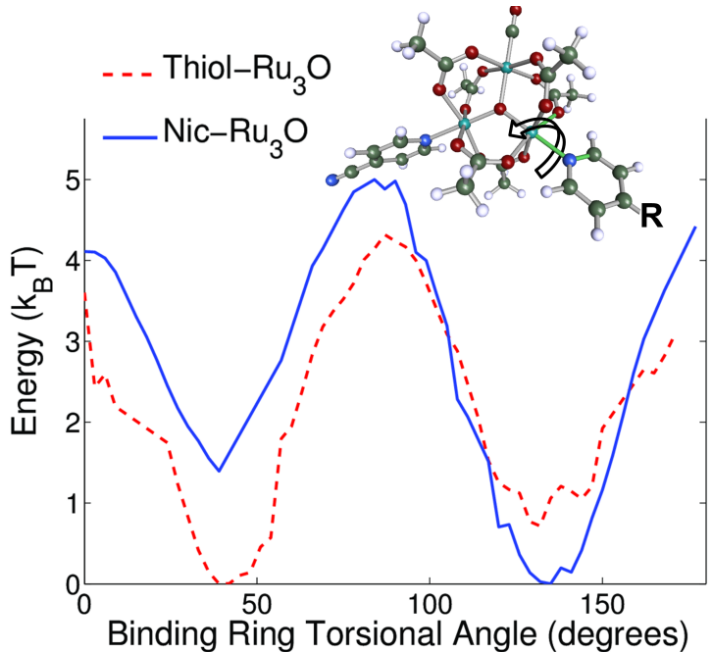

Figure 4.11. Geometry-optimized torsional potential energy curves, as a function of the torsional angle ψ between the bridging pyridine ligand and the three Ru atoms, for the QD-nic- and QD-thiol-Ru_3O complexes, calculated with the PBE0 hybrid functional and the TZVPP basis set. For both complexes, the surfaces contain two minima: ψ = 135°, where the pyridine-4-**R** moiety is perpendicular to the plane of the Ru atoms ("twisted" conformation), and ψ = 40°, where the pyridine-4-**R** moiety is co-planar with the Ru atoms ("coplanar" conformation). The **R** group is either the carboxylic acid or the thiol that links the cluster to the QD surface. ***Inset:*** Ru_3O cluster highlighting (in green) the O-Ru-N-C torsional angle ψ being scanned. The angle pictured corresponds to ψ=0°, and ψ increases as the pyridine moiety rotates in the direction of the arrow.

4.6 Conclusions

We measured the photoinduced electron transfer rate from photoexcited CdSe QDs to adsorbed oxo-centered triruthenium clusters (Ru_3O) through either a pyridine-4-carboxylic acid linkage (nic-Ru_3O) or a 4-mercaptopyridine linkage (thiol-Ru_3O) (Figure 4.2). We analyzed the rate of PET by monitoring the formation of the Ru_3O^- radical anion at 1150 nm in the transient absorption spectra. The

intrinsic charge separation rate constant ($k_{CS,int}$), which is independent of the number of adsorbed Ru_3O complexes per QD, is approximately seven times faster for the thiol-Ru_3O cluster compared to the nic-Ru_3O cluster. We rule out differences in the driving force and reorganization energy as explanations of the difference in the PET rate for the two clusters, and therefore conclude that the difference in donor-acceptor electronic coupling for the two complexes is responsible for the discrepancy in their PET rates. We further determine that electronic coupling is dictated by the O-Ru-N-C torsional angle of the bridging ligand of the cluster, and that the maximum electronic coupling is achieved when the pyridine ring of the bridging ligand is co-planar with the three Ru atoms of the cluster core: this is the PET-active conformation of the complex. We can therefore say that it is the difference in electronic coupling between donor and acceptor orbitals in this conformation that results in the observed differences in PET rate between the two complexes; however, discussion of the chemical and structural factors that result in this difference is speculative without precise knowledge of the binding geometry and chemistry for both complexes.

This work illustrates that the charge transfer rates between colloidal quantum dots and redox-active ligands adsorbed to their surfaces can be tuned through the choice of the coordinating headgroup of the ligand. In future work, we would like to design systems in which we can achieve dynamic control of the conformation of ligands on the surface of the QD and modulate the electronic coupling in the QD-ligand complex. Achievement of this goal will be facilitated by continual

development of tools for quantitative chemical characterization of the ligand shell on small colloids.

4.7 Experimental

Synthesis of Ru_3O Clusters

$Ru_3O(OAc)_6(CO)$(4-cyanopyridine)(4-pyridine thiol) and $Ru_3O(OAc)_6(CO)$(4-cyanopyridine)(isonicotinic acid) were synthesized following previously reported procedures.[8,9,15] Briefly, we stirred $Ru_3O(OAc)_6(CO)$(4-cyanopyridine)(H_2O) (100 mg) in minimal CH_2Cl_2 and 10 mL MeOH in an ice bath, and added 4-pyridine thiol or isonicotinic acid (10 eq.) as a solid over several minutes. The reaction was stirred for 48 hours and subsequently allowed to warm to room temperature. The product was filtered through Celite to remove excess free thiol or free carboxylic acid. We filtered the product as needed to ensure purity as confirmed by NMR. The product was dried in a rotary evaporator with no heat applied, precipitated it with excess hexanes, diluted it in minimal degassed CH_2Cl_2, and collected it on a fine porosity glass frit. The product was washed with hexanes. The residue was once again re-diluted in degassed CH_2Cl_2 and crashed out with hexanes. If difficulties arise with crashing out in hexanes small amounts of anhydrous diethyl ether can be added. The product was collected on a fine porosity frit, dried overnight in a vacuum oven with no heat applied, and stored away from light.

Electrochemical Measurements

Cyclic Voltammetry experiments were performed in degassed CH_2Cl_2 under an atmosphere of N_2. Experiments were performed with a BAS Epsilon potentiostat with 0.1M tetrabutylammonium hexafluorophosphate (TBAH) as the supporting electrolyte. TBAH was recrystallized from methanol and dried under vacuum. Experiments were carried out with 0.1mM analyte concentrations and 100mV/s scan rate using a 3mm glassy carbon working electrode, a platinum wire as the counter electrode, and Ag/AgCl wire as the reference electrode. The ferrocene/ferrocenium couple was used as an internal standard.

UV/vis/NIR Data Collection.

UV/vis/NIR data were collected on a Shimadzu UV-3600 UV/vis/NIR spectrometer. Samples were enclosed in a Specac sealed liquid IR cell with CaF_2 windows with 0.5 mm path length. Curve fitting of spectra to multiple Gaussian peaks was performed in Origin 6.0. Chemical reductions were performed using decamethylcobaltocene ($E^{o'}$= -1.94 vs. Fc/Fc^{+})[65] as the reducing agent. Optical cryostat studies were performed using a Specac variable temperature cell holder (Model GS21525). The temperature is controlled by addition of liquid nitrogen and subsequent heating with a computer controlled thermocouple.

***Infrared Spectroscopy*.**

Infrared spectra were obtained on a Bruker Equinox 55 spectrometer using a custom built reflectance spectroelectrochemical cell and air-tight IR cells from Specac.

Absorption Measurements of Ru_3O Clusters

We collected ground state absorption spectra of the Ru_3O clusters on a Shimadzu UV-3600 UV/vis/NIR spectrometer. Samples were prepared in a nitrogen filled glovebox. The samples were reduced with a small excess of decamethylcobaltocene and filtered to remove any impurities or undissolved reducing agent. The samples were injected into a Specac sealed liquid IR cell with CaF_2 windows and a 1mm metal spacer. In order to prevent the Ru_3O anion from degrading rapidly, the cells were kept at -20 °C once exposed to air.

Synthesis and Purification of CdSe QDs

We added 90% technical grade trioctylphosphine oxide (TOPO, 1.94 g, 5.02 mmol), hexadecylamine (HDA, 1.94 g, 8.03 mmol), and cadmium stearate ($CdSt_2$, 0.112 g, 0.165 mmol) to a dry 50-mL three-neck round bottom flask, and dried the reaction mixture for 1 h at 120 °C under N_2(g). We heated the mixture to 320 °C with stirring under positive nitrogen flow. After the $CdSt_2$ completely dissolved, we rapidly injected trioctylphosphine selenide (TOPSe, 1 mL of 1 M solution in TOP, prepared and stored in a glovebox), and allowed the QDs to grow at 290 °C for 30 seconds. We removed the flask from heat, and cooled the reaction mixture to room temperature by adding 10 mL of hexanes under vigorous nitrogen flow. We allowed the reaction mixture to stir in a three-neck flask for 2 h at room temperature, and then centrifuged the reaction mixture at 3500 rpm for five minutes, which yielded a white pellet containing unreacted reagent and excess ligand and a clear, orange supernate containing the QDs. We decanted the supernate, added 1:1 v/v methanol,

which made the solution turbid, and re-centrifuged the sample. We treated the QDs with another cycle of purification by dispersing them in hexane, precipitating them with 1:1 v/v methanol, centrifugation and decantation. Finally, we dispersed the pellet in 20 mL of chloroform.

Calculation of the Average Number of Clusters Adsorbed per QD

To calculate the number of adsorbed Ru_3O clusters, we must first estimate the number of surface sites. We estimated an upper bound for number of surface sites by calculating the number of the largest of ions in the QD (Se^{2-}) that could be present at the surface of the QD. We calculate the number of surface atoms on a CdSe QD with Eq. 5,

$$n_{sites} = \frac{\pi}{4}\left(\frac{4\pi {r_{QD}}^2}{\pi r {Se^{2-}}^2}\right)$$

where r_{QD} is the radius of the QD and $r_{Se^{2-}}$ is the radius of the selenide anion. Equation 5 yields approximate 110 surface sites perCdSe QD for the d=2.4 nm QDs used in this study.

We have shown previously that the fraction of QD PL intensity remaining after addition of an efficient quenching ligand (PL/PL_0) reveals the fraction of QDs with zero adsorbed ligands and the mean fractional surface coverage, θ. To find θ, we first model the distribution of ligands bound to each QD using the binomial distribution,

$$P(m|N,\theta) = \binom{N}{m}\theta^m(1-\theta)^{N-m}$$

where $P(m|N,\theta)$ is the probability of finding a QD within the ensemble with m adsorbed ligands given that each QD has N surface sites and a mean fractional surface coverage of ligands is θ. Since PL/PL$_0$ equals $P(m|N,\theta)$, we substitute 0 in for m and solve.

$$P(m|N,\theta) = \left(\frac{PL}{PL_0}\right) = (1-\theta)^N$$

Using Eq. 7 with N = 115 and three separate measurements of PL/PL$_0$ on samples prepared identically to those we measured in the TA experiment, we find that there are an average of 2.9 thiol-Ru$_3$O clusters adsorbed per QD and an average of 1.1 nic-Ru$_3$O clusters adsorbed per QD at the concentrations of each component of the mixtures that we study with TA.

Preparation of Samples for Transient Absorption (TA)

We acquired ground state absorption spectra of the QDs on a Varian Cary 5000 spectrometer, and used the absorption at the first excitonic peak to determine the size and concentration of the QDs.[10] We prepared each QD-Ru$_3$O sample in distilled $CHCl_3$ such that the resulting solution was 26 μM in QDs and had a molar ratio of Ru$_3$O/QD = 20:1. These samples had an optical density of 0.3 a.u. at the first excitonic peak in a 2-mm cuvette. We found that the amplitude of the signal from the Ru$_3$O transients in the TA experiment decayed on the 6-24 h timescale once we mixed the Ru$_3$O clusters with the solutions of QDs. We attribute this loss of signal to degradation of the Ru$_3$O clusters in the presence of the QDs. To prevent degradation, we prepared a fresh sample immediately before each TA experiment. Figure 4.12 shows plots from control experiments where we measured the TA

spectrum for a single QD-Ru_3O sample over four consecutive runs. These experiments confirm that the samples are stable on the TA timescale (~1-4 h); the excited state dynamics we observe therefore do not result from degradation and are characteristic of an equilibrated system. In addition, Figure 4.13 describes steady-state PL measurements that show that the QD-Ru_3O complexes equilibrate approximately 30 minutes after mixing (before the first TA measurement).

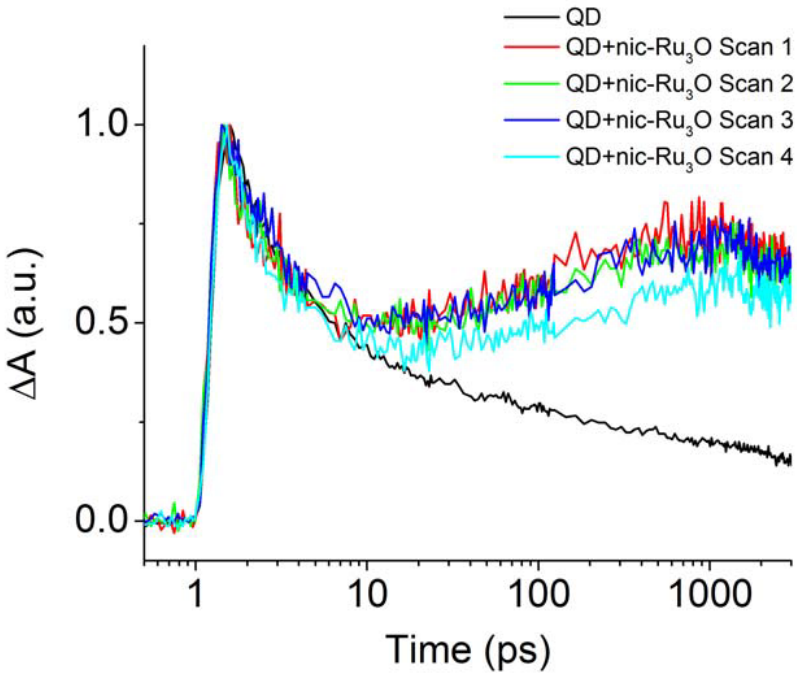

Figure 4.12. Transient absorption kinetic traces at a probe wavelength of 1200 nm of 3.0×10^{-5} M CdSe QDs (d = 2.4 nm) in $CHCl_3$ with no added Ru_3O (black), and of the same QDs with the nic-Ru_3O added at a ratio of 20 clusters/QD. The first three kinetic scans retrace one another well while the fourth scan shows an approximately 20% decrease in amplitude of the signal from the Ru_30^- anion due to photodegradation.

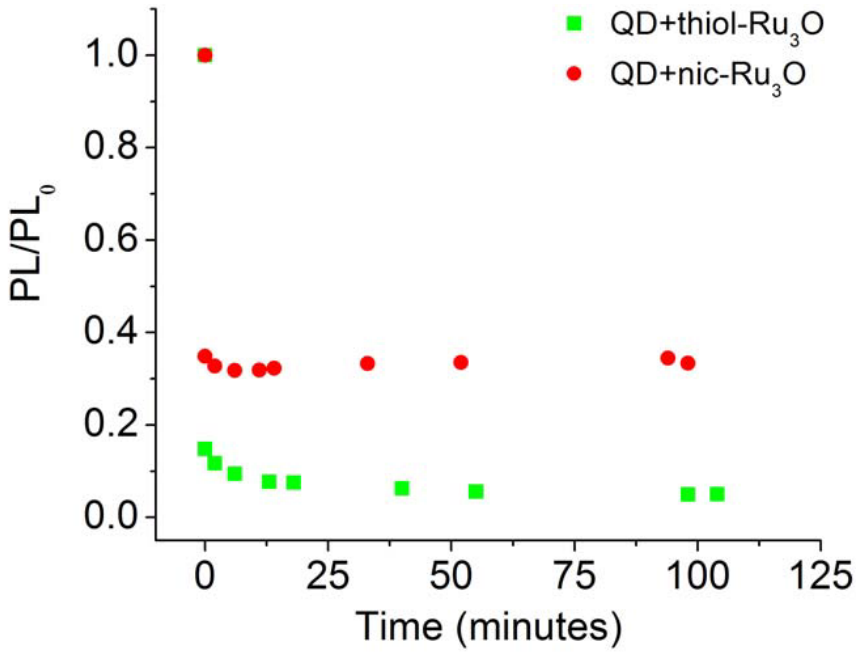

Figure 4.13. Time dependence of the integrated photoluminescence intensity of 3.0×10^{-5} M CdSe QDs (d = 2.4 nm) in $CHCl_3$ with nic-Ru_3O (red) or thiol-Ru_3O added at a ratio of 20 clusters/QD. The PL is normalized to the integrated PL intensity of an identical sample with no added Ru_3O (black).

Transient Absorption Spectroscopy

The transient absorption setup, with visible and NIR continuum probes, is described in detail elsewhere.[16,17] The pump light was depolarized to prevent photoselection so that measurements reflect only population dynamics. We adjusted the incident pump power and spot size to produce an expected excited state population of 0.30. We stirred the solution during the measurement with a magnetic stir bar to minimize local heating.

Computational Methods

We calculated optimized geometries for the Ru_3O clusters and QD-Ru_3O complexes within the TURBOMOLE electronic structure package.[26] The DFT

calculations used the multipole-accelerated resolution-of-the-identity approximation.[27-30] We used a $Cd_{13}Se_{13}$ cluster geometry[31] as a minimal QD structure. We generated coordinates for torsional potential energy surfaces (TPES) by scanning the O-Ru-N-C torsional angle on the binding pyridine ring for each Ru_3O cluster in three-degree increments. For each geometry, we performed a geometry optimization using the def2-SV(P) basis set and the B3LYP hybrid exchange correlation functional[32] while freezing the torsional angle. To obtain more accurate energies at each geometry, we computed single-point energies at the optimized geometries with the def2-TZVPP basis set. We qualitatively reproduced the TPES we obtained with the B3LYP functional by computing single-point energies at the same optimized geometries with the PBE0 and TPSSH hybrid functionals.

Note: Much of the material for this chapter comes directly from a manuscript entitled "Controlling the Rate of Electron Transfer Between QDs and Ru3O Clusters by Tuning the Chemistry of the Interface" by Adam J. Morris-Cohen, Kenneth O. Aruda, Andrew M. Rasmussen, Gabriele Canzi, Tamar Seideman, Clifford P. Kubiak, and Emily A. Weiss which has been published in *Physical Chemistry Chemical Physics* ***2012***, 14, pp.13794-13801 The dissertation author is a contributing author of this manuscript

4.8 References

(1) Benson, E. E.; Sathrum, A. J.; Smieja, J. M.; Kubiak, C. P. *Chem. Soc. Rev.* **2009**, *38*, 89.

(2) Galan, B. R.; Schoffel, J.; Linehan, J. C.; Seu, C.; Appel, A. M.; Roberts, J. A. S.; Helm, M. L.; Kilgore, U. J.; Yang, J. Y.; Dubois, D. L.; Kubiak, C. P. *J. Am. Chem. Soc.* **2011**, *133*, 12767.

(3) Smieja, J. M.; Kubiak, C. P. *Inorg. Chem. (Washington, DC, U. S.)* **2010**, *49*, 9283.

(4) Sykora, M.; Petruska, M. A.; Alstrum-Acevedo, J.; Bezel, I.; Meyer, T. J.; Klimov, V. I. *J. Am. Chem. Soc.* **2006**, *128*, 9984.

(5) Huang, J.; Stockwell, D.; Huang, Z. Q.; Mohler, D. L.; Lian, T. Q. *J. Am. Chem. Soc.* **2008**, *130*, 5632.

(6) Abe, M.; Sasaki, Y.; Yamada, Y.; Tsukahara, K.; Yano, S.; Yamaguchi, T.; Tominaga, M.; Taniguchi, I.; Ito, T. *Inorg. Chem. (Washington, DC, U. S.)* **1996**, *35*, 6724.

(7) Baumann, J. A.; Wilson, S. T.; Salmon, D. J.; Hood, P. L.; Meyer, T. J. *J. Am. Chem. Soc.* **1979**, *101*, 2916.

(8) Canzi, G.; Kubiak, C. P. *Small* **2011**, *7*, 1967.

(9) Salsman, J. C.; Ronco, S.; Londergan, C. H.; Kubiak, C. P. *Inorg. Chem. (Washington, DC, U. S.)* **2006**, *45*, 547.

(10) Yu, W. W.; Qu, L.; Guo, W.; Peng, X. *Chem. Mater.* **2003**, *15*, 2854.

(11) McArthur, E. A.; Godbe, J. M.; Tice, T. B.; Weiss, E. A. *J. Phys. Chem. C* **2012**, *in press*.

(12) Kucur, E.; Riegler, J.; Urban, G. A.; Nann, T. *The Journal of Chemical Physics* **2003**, *119*, 2333.

(13) Cooney, R. R.; Sewall, S. L.; Dias, E. A.; Sagar, D. M.; Anderson, K. E. H.; Kambhampati, P. *Physical Review B* **2007**, *75*.

(14) Klimov, V. I.; McBranch, D. W.; Leatherdale, C. A.; Bawendi, M. G. *Physical Review B* **1999**, *60*, 13740.

(15) Goeltz, J. C.; Kubiak, C. P. *J. Am. Chem. Soc.* **2010**, *132*, 17390.

(16) Knowles, K. E.; McArthur, E. A.; Weiss, E. A. *ACS Nano* **2011**, *5*, 2026.

(17) McArthur, E. A.; Morris-Cohen, A. J.; Knowles, K. E.; Weiss, E. A. *J. Phys. Chem. B*, *114*, 14514.

(18) Morris-Cohen, A. J.; Frederick, M. T.; Cass, L. C.; Weiss, E. A. *J. Am. Chem. Soc.* **2011**, *133*, 10146.

(19) Lian, T. Q.; Song, N. S., N. H.; Zhu, H. M.; Jin, S. Y.; Zhan, W. *ACS Nano* **2011**, *5*, 613.

(20) Tachiya, M. *Chem. Phys. Lett.* **1975**, *33*, 289.

(21) Tachiya, M. *J. Chem. Phys.* **1982**, *76*, 340.

(22) Huang, J. E.; Huang, Z. Q.; Jin, S. Y.; Lian, T. Q. *J. Phys. Chem. C* **2008**, *112*, 19734.

(23) Morris-Cohen, A. J.; Vasilenko, V.; Amin, V. A.; Reuter, M. G.; Weiss, E. A. *ACS Nano* **2011**.

(24) Jortner, J. *J. Chem. Phys.* **1976**, *64*, 4860.

(25) Marcus, R. A.; Sutin, N. *Biochim. Biophys. Acta* **1985**, *811*, 265.

(26) Ahlrichs, R.; Bär, M.; Häser, M.; Horn, H.; Kölmel, C. *Chemical Physics Letters* **1989**, *162*, 165.

(27) Sierka, M.; Hogekamp, A.; Ahlrichs, R. *The Journal of Chemical Physics* **2003**, *118*, 9136.

(28) Eichkorn, K.; Treutler, O.; Öhm, H.; Häser, M.; Ahlrichs, R. *Chemical Physics Letters* **1995**, *240*, 283.

(29) Eichkorn, K.; Weigend, F.; Treutler, O.; Ahlrichs, R. *Theoretical Chemistry Accounts: Theory, Computation, and Modeling (Theoretica Chimica Acta)* **1997**, *97*, 119.

(30) Weigend, F. *Physical Chemistry Chemical Physics* **2002**, *4*, 4285.

(31) Chung, S.-Y.; Lee, S.; Liu, C.; Neuhauser, D. *The Journal of Physical Chemistry B* **2009**, *113*, 292.

(32) Treutler, O.; Ahlrichs, R. *The Journal of Chemical Physics* **1995**, *102*, 346.

Chapter 5

Electronic coupling across hydrogen bonded interfaces

5.1 Introduction

The study of electron transfer (ET) processes through non-covalent interactions is essential in the broader understanding of how long-range electron transfer occurs in biological and artificial supramolecular systems, and has been a topic of considerable interest in recent years.[1-8] Of the non-covalent interactions that define the spatial arrangement of these types of structures, hydrogen bonds are ubiquitous, and, although very few examples exist, hydrogen bonded mixed valence complexes serve as important models for biological electron transfer (ET).[1,3,7-10]

Ruthenium clusters of the types $[Ru_3(\mu_3\text{-}O)(OAc)_6(CO)(L)(L')]$ and $[Ru_3(\mu_3\text{-}O)(OAc)_6(CO)(L)\text{-}(\mu_2\text{-}BL)\text{-}Ru_3(\mu_3\text{-}O)(OAc)_6(CO)(L)]$ have been very fruitful in furthering the understanding of both inter- and intramolecular ground state electron transfer behavior in inorganic mixed valency.[7,11-35] These simple oxo-

centered clusters serve as a robust backbone, especially due to their synthetic accessibility by simple ancillary ligand, and bridging ligand substitution. Ancillary ligand substitution permits simple synthetic control over the electron donating ability (based on ligand conjugate acid pKa) of each cluster. Work on analogous ruthenium systems have shown that the electronic coupling in molecular mixed valence dimers of trimers is controlled by the overlap of the Ru_3 clusters d-orbitals with the bridging ligand (pyrazine and bipyridine) π^* orbitals. Furthermore, the cluster d-orbital energies are raised relative to the bridging ligand π^* orbital by increasingly electron donating ancillary pyridyl ligands.[7,11-15,17,18,26] By using this analysis we seek to investigate whether these effects are true in hydrogen bonded mixed valence dimers.

5.2 Results and discussion

Using isonicotinic acid as an ancillary ligand complex **1** was synthesized according to previous reports. The carboxylic acid functional group is the basis for the formation of cyclic hydrogen-bonded dimers following a one electron reduction, as shown in Figure 5.1. Measurement of electrochemical responses is essential to elucidate the mechanism for the ground state ET reaction. Cyclic voltammetry in a 0.1 M tetrabutylammonium hexafluorophosphate solution in acetonitrile vs. Ag/AgCl reveals two reversible one-electron oxidations at positive potentials (Figure 5.2, waves A and B), and two overlapping one-electron reductions at negative potentials (Figure 5.2, waves C and D, respectively) as shown in

differential pulse voltammetry (DPV) results, Figure 5.3. The splitting, 285 mV in ACN, between the two oxidative processes, occurring at -817 mV and -532 mV (Figure 5.2, waves E and F), is indicative of the presence of a thermodynamically stable mixed valence state and moderate electronic communication between the two redox-active Ru_3O clusters due to the formation of a hydrogen bonded bridge, *vide infra*. Consistent with this interpretation voltammetric experiments performed in DMSO show a clear disruption of any bridging interaction; only one single-electron reductive wave is observed at reducing potentials.[7]

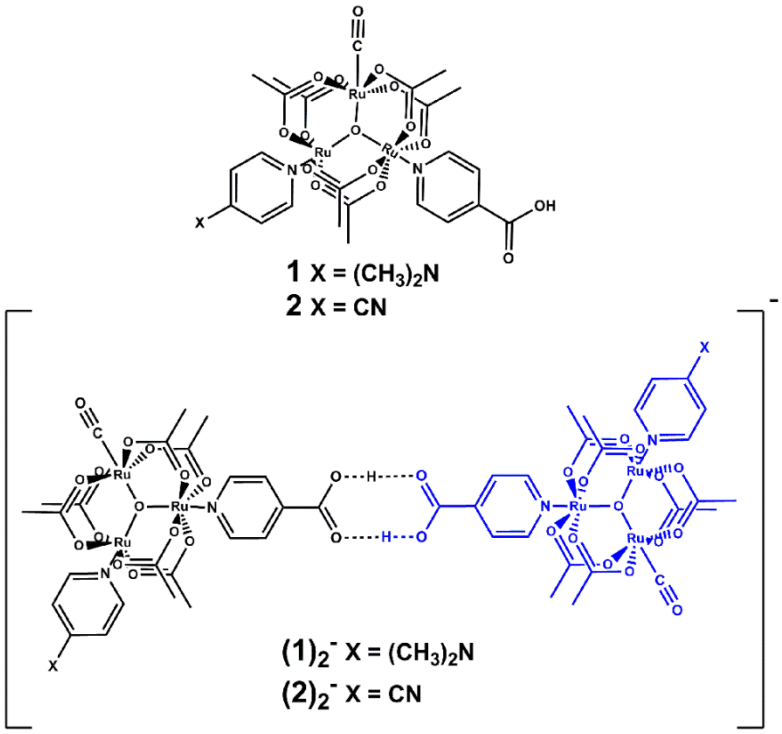

Figure 5.1. Structure of complexes **1** and **2** used in this study**,** and the mixed valence dimer ion $\mathbf{(1)_2}^{-1}$ and $\mathbf{(2)_2}^{-1}$ formed upon dimerization after a one-electron reduction of **1** and **2** respectively. A second single-electron reduction yields the doubly reduced dimer, $\mathbf{(1)_2}^{-2}$ and $\mathbf{(2)_2}^{-2}$.

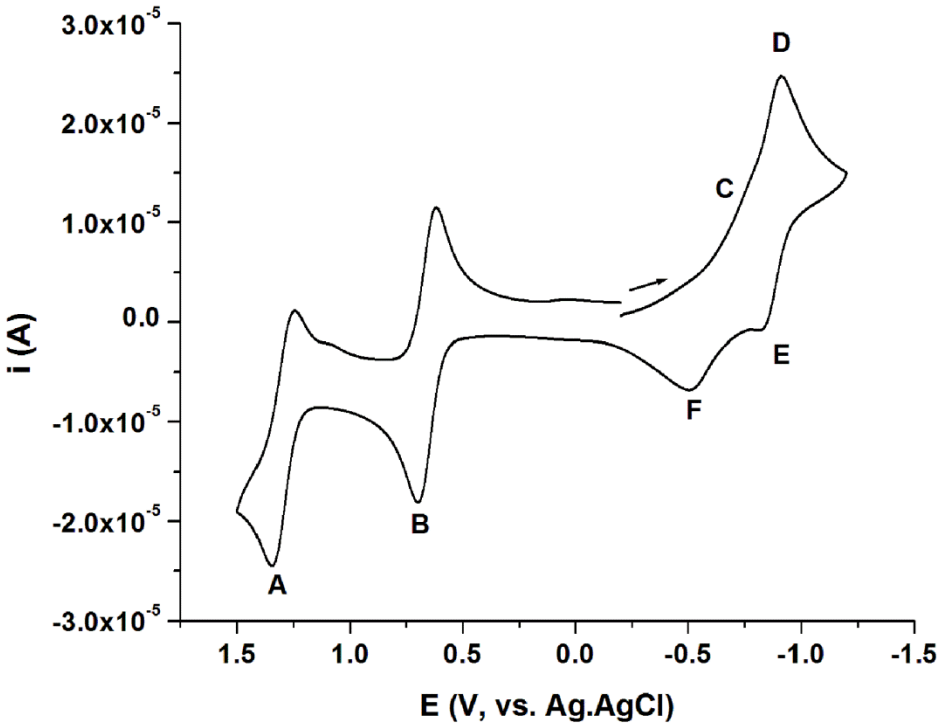

Figure 5.2. Cyclic voltammogram of **1** in acetonitrile at a scan rate of 100mV/s with a 3 mm glassy carbon working electrode, a Pt counter electrode, and a Ag/AgCl reference. CV measurements were started and ended at 200 mV. At positive potentials two single-electron oxidations are observed (A and B). At negative potentials two overlapping single-electron reductions are apparent (C and D). On the return sweep two distinct reoxidation waves are apparent (E and F), indicative of a ECE mechanism where C is dimerization due to a hydrogen-bonding interaction.

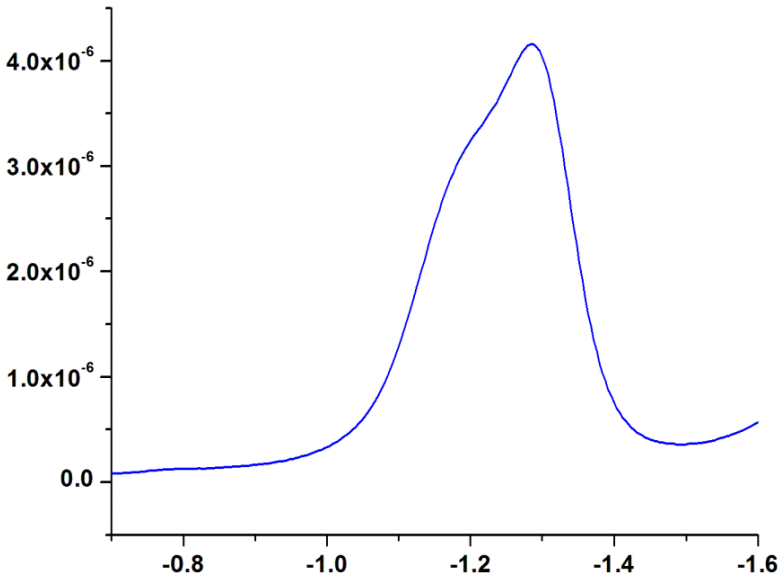

Figure 5.3. Differential Pulse Votammetry (DPV) of **1** in DCM at a scan rate of 20 mV/s vs. Fc/Fc^{+} couple. The response observed clearly indicates that there are two overlapping reductions (C and D) in the forward wave of the cyclic voltammogram.

The comproportionation constant,[36] $K_c = e^{\frac{nF\Delta E_{\frac{1}{2}}}{RT}}$, of $\mathbf{(1)_2}^{-}$ has been shown to be on the order of 10^5 and 10^3 for $\mathbf{(2)_2}^{-}$ indicating that the mixed-valence ion is highly stable with respect to the disproportionation reaction.[7] In contrast, K_{dim} of unreduced monomer **1** is quite small, <0.01.[7] Significant electronic coupling in hydrogen-bonded mixed-valence systems has been shown to exist in various systems.[4,37] In fact, hydrogen bonds have been shown to have electronic couplings comparable with covalent σ bonds.[4,38] The observed electrochemical behavior of these Ru_3O clusters in solution is best described by an ECE mechanism, where E is attributed to a one-electron reduction, and C is dimerization of the complex. The electrochemical

splitting of the reoxidation waves (E and F) was found to modulate with solvent choice.

Table 5.1. Splitting (in mV) observed for the reoxidation waves in the CV for the solvents used in this chapter.

Solvent	Splitting (mV)
DCM	393
ACN	285
DMF	244
THF	365
Toluene	405
DMSO	0

As shown in Figure 5.4, good agreement (R^2= 0.83) was found between the electrochemical splitting of E and F with the solvent dielectric constants of the solvents used in this study. This indicates destabilization of mixed valency across hydrogen bonds in higher dielectric media.

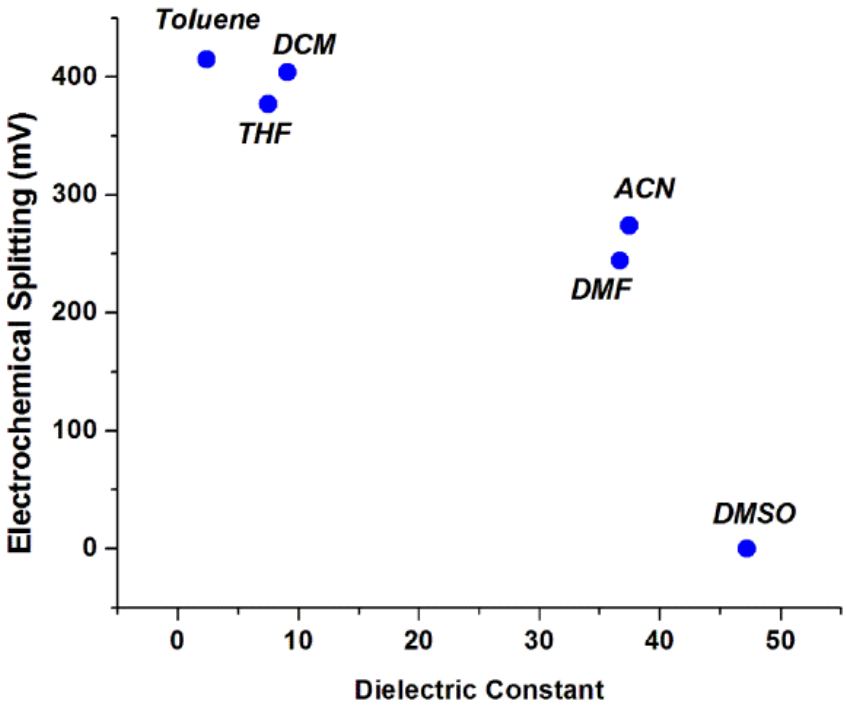

Figure 5.4. Electrochemical splitting of the return waves (1 mM concentration, 100 mV/s scan rate) observed in the electrochemical responses of **1** versus solvent dielectric constants for the solvents used in this study.

FT-IR spectroscopy of neutral (0) monomer **1** shows a ν(CO) stretch at 1945 cm^{-1}, as expected for Ru_3O carbonyl complexes.[7,20,21,26,39,40] Upon two one-electron reductions, the fully reduced state, $\mathbf{(1)_2}^{2-}$, exhibits a shift of 50 wavenumbers to 1895 cm^{-1}. This shift is consistent with additional electron density on the cluster increasing the π backbonding of the carbonyl. The mixed valence state, $\mathbf{(1)_2}^{-}$, shows essentially no dynamic coalescence of the ν(CO) stretch under the same conditions, signifying localized behavior on the IR timescale with distinct stretches observed at 1937 and 1897 $cm^{-1,}$ as shown in Figure 5.5. Localized behavior in FT-IR clearly indicates that the ET process is slower than the vibrational timescale, 10^{10} s^{-1}.

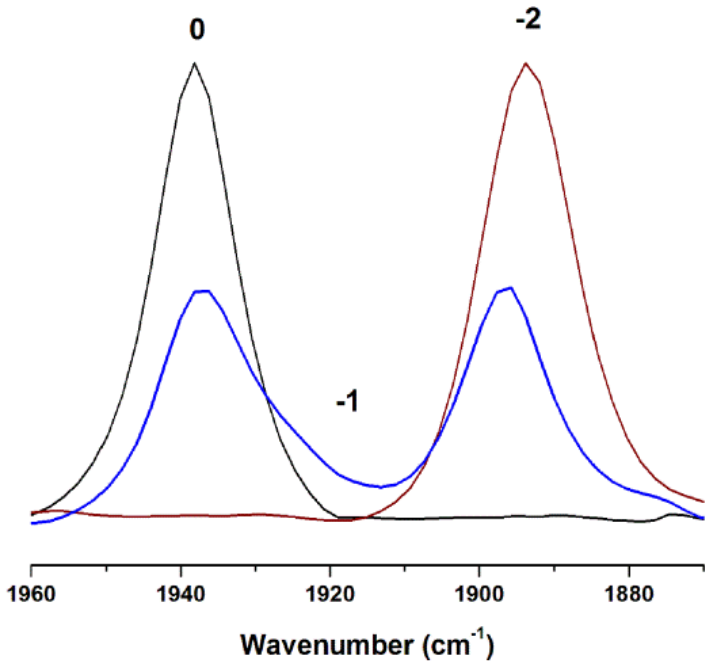

Figure 5.5. FT-IR of the ν(CO) in acetonitrile for the neutral (0, black), mixed valence (-1, blue) and fully reduced state (-2, red) of complex **1**. Chemical reductions were performed using bis(η_5-pentamethyldienyl)cobalt(II) as the reducing agent. The absence of dynamic coalescence of the ν(CO) in the mixed valence state is evidence of localized behavior on the IR timescale.

The electronic absorption spectra of **1** in acetonitrile shows two distinct absorptions in the visible region, analogous to previously reported Ru_3O monomers.[7,13,18,26] The higher energy absorption (λ_{max} 399 nm, ν_{max} 25707 cm^{-1}, ε_{max} 7260) is assigned as a metal-to-ligand charge transfer (MLCT) and the lower energy absorption (λ_{max} 596 nm, ν_{max} 17065 cm^{-1}, ε_{max} 5860) is assigned as intracluster charge transfer (ICCT), consistent with literature precedent.[26] Upon a single one-electron reduction a concomitant shift and intensification of the ICCT band, coupled with a weakening of the MLCT band is apparent. In addition, new

bands appear in the near-infrared (NIR) region, diagnostic of *two* distinct intervalence charge transfer (IVCT) transitions, and not one band as expected by the normal two-state Marcus-Hush description of the symmetric mixed valence complex.[41,42] IVCT bands similar to those observed in the electronic spectra of $(\mathbf{1})_2^-$ have also been observed in multiple hydrogen-bonded systems by Kaifer, where ferrocene centers showed surprisingly large electronic couplings across large separations between donor and acceptor.[37]

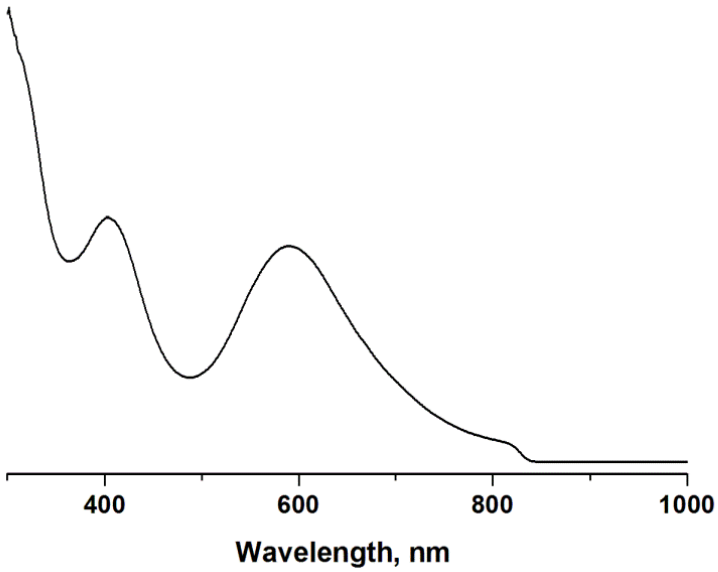

Figure 5.6. Electronic absorption spectra of **1** in acetonitrile showing two absorptions in the visible region. The higher energy absorption (λ_{max} 399 nm) is assigned as a metal-to-ligand charge transfer (MLCT) and the lower energy absorption (λ_{max} 596 nm) is assigned as intracluster charge transfer (ICCT), consistent with literature precedent.

Previous work by our laboratory showed that the appearance and behavior of *two* IVCT bands in the NIR region of the electronic spectra of pyrazine bridged

Ru_3O dimers was best described by the application of a semiclassical three-state model.[13] The Brunschwig, Creutz, and Sutin (BCS) three-state model uses the basis of a two-state system and adds an additional element for the bridge.[43] The BCS model is parametrized in terms of donor acceptor coupling, (H_{ac}), donor bridge couplings, (H_{ab}, H_{bc}), and the energy separation between the donor and the bridge state, (ΔG_{ab}). Consistent with the BCS model, the higher energy IVCT band is best described as metal-to-bridge charge transfer (MBCT) since the bridge state is expected to be higher in energy than the metal states.[13,43] The remaining lower energy band can then be assigned as metal-to-metal charge transfer (MMCT).[13,43] These characteristic bands are absent in the electronic absorption spectra after a one electron reduction in DMSO, a hydrogen-bonding solvent that has been shown to disrupt the dimerization of similar systems as shown in Figure 5.9.[7]

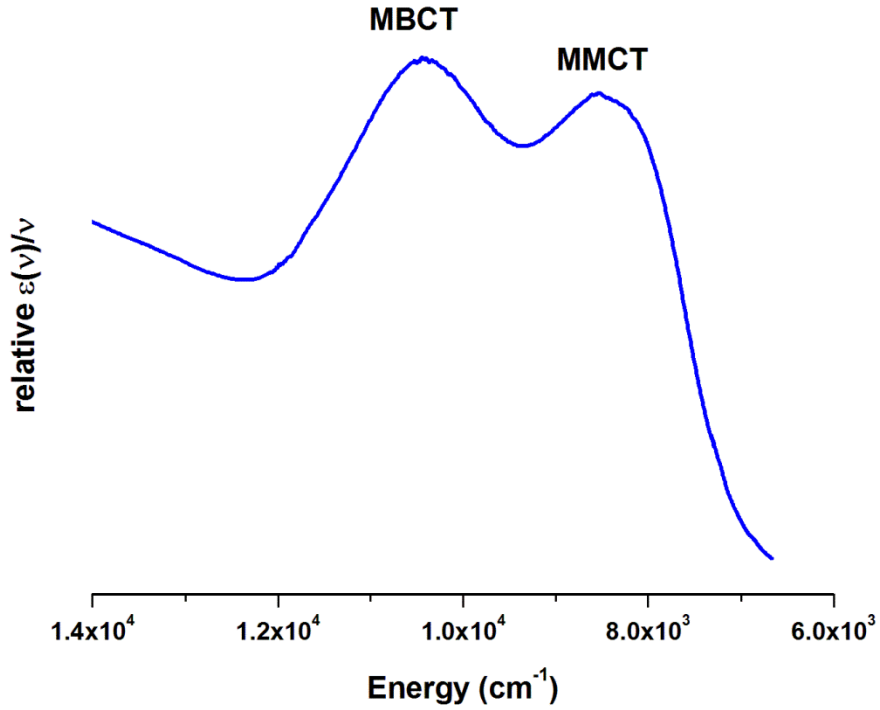

Figure 5.7. Near-infrared (NIR) region of the electronic absorption spectra of **1** showing two distinct IVCT bands at 298 K in acetonitrile with an optical parthlength of 0.5 mm decamethylcobaltocene as the reducing agent. The low energy band is assigned as a metal-to-metal charge transfer (MMCT) and the high energy band as metal-to-bridge charge transfer (MBCT).

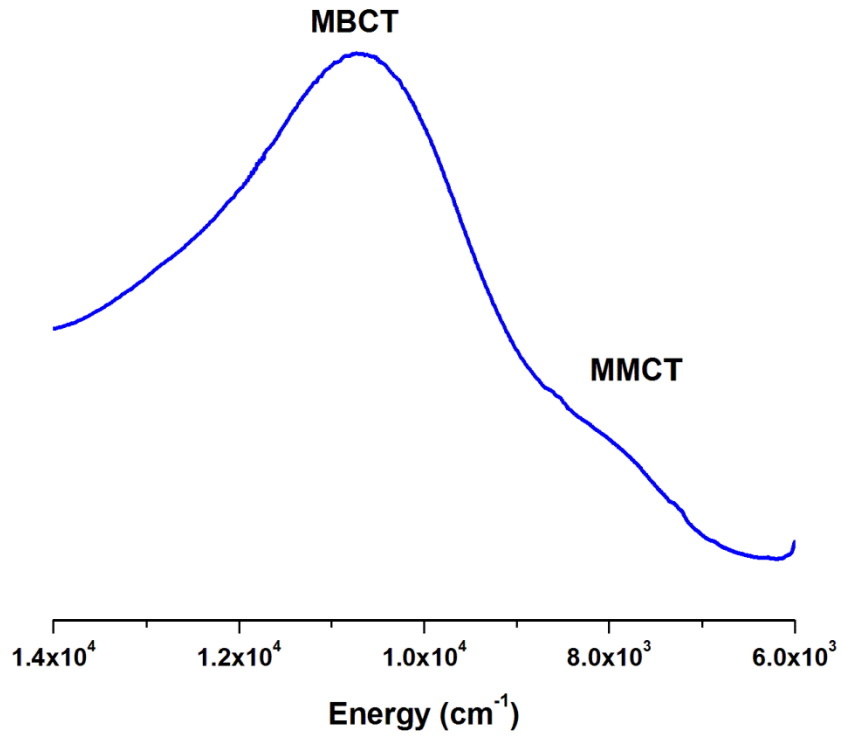

Figure 5.8. Near-infrared (NIR) region of the electronic absorption spectra of **2** showing two distinct IVCT bands at 298 K in acetonitrile with an optical parthlength of 0.5 mm decamethylcobaltocene as the reducing agent. The low energy band is assigned as a metal-to-metal charge transfer (MMCT) and the high energy band as metal-to-bridge charge transfer (MBCT). Differences in MMCT with the NIR region of **1** are attributed to the magnitude of metal-to-bridge coupling due to ancillary ligand substitution.

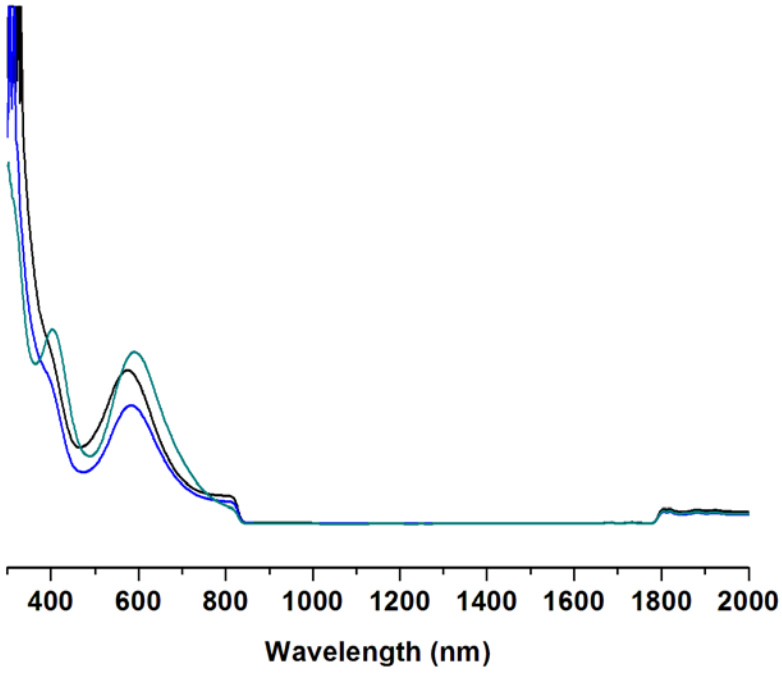

Figure 5.9. Electronic absorption spectra of **1** showing *no* IVCT bands at 298 K in DMSO.

The presence of *two* IVCT bands is significant because it highlights the importance of the metal-to-bridge coupling. We have previously shown that in other Ru_3O systems,[14-17] a close match between the π* levels of the bridge to the dπ of the Ru allows for significant electron spin density to be on the bridge.[17] We probed the effects on metal-to-metal coupling (H_{ac}) by varying the donor ability of these systems by tuning the energetics of the clusters by simple ancillary ligand substitution. As shown in Figure 5.9, when an electron withdrawing ancillary ligand such as 4-cyanopyridine (pka≈2) is used, the intensity of the MMCT is weaker in comparison to when an electron donating ligand such as 4-dimethylaminopyridine

(pka ≈9) is used. This highlights the importance of metal-to-bridge (H_{ab} *and* H_{bc}) couplings. The data clearly shows that the magnitude of H_{ac} in these systems is directly related to the magnitude of H_{ab} and $H_{bc,}$ and that in systems bridged by a non-covalent interaction such as a hydrogen bond, meaningful metal-to-metal electronic coupling is only observed when there is a substantial metal-to-bridge interaction.

In a donor (M_a), bridge (B_b), acceptor (M_c) system,

$$M_a - B_b - M_c \qquad (1)$$

each represented by basis functions:

$$\varphi_a, \varphi_b, \varphi_c \qquad (2)$$

In the limit of significant delocalization between the metal centers and the bridging ligand, significant mixing between the metal based and bridging ligand functions can occur:

$$\Psi_a = a\varphi_a + b\varphi_b \qquad (3)$$

$$\Psi_c = c\varphi_c + b\varphi_b \qquad (4)$$

The direct mixing of metal center and bridging ligand wavefuntions, provides an indirect quantum mechanical mechanism for donor (M_a), - acceptor (M_c) overlap

$$\int \Psi_a \Psi_c \approx \int b^2 \varphi_b^2 \neq 0 \qquad (5)$$

It is this metal-ligand mixing which provides significant electronic coupling between metal centers normally considered too far apart or too weakly *directly* coupled to give a stable mixed valence state.

Changes in the IVCT bands of **1** in acetonitrile were monitored as a function of temperature from 300 K to 258 K. As the temperature is decreased the MBCT and MMCT band intensities increase and no major shifts in energies are observed, Figure 5.10. The intensification of both the MMCT and MBCT is predicted by the BCS model and is due to an increase in H_{ac} for a Class II system at lower temperatures.[43] Minimal or no changes in the energies of these transitions are expected for a localized electronic ground state where solvent dynamic motions are faster than the ground state electron-transfer rate.[13] These results are analogous to purely Robin-Day Class II bipyridine bridged mixed valence dimers previously studied in our laboratory.[13,44]

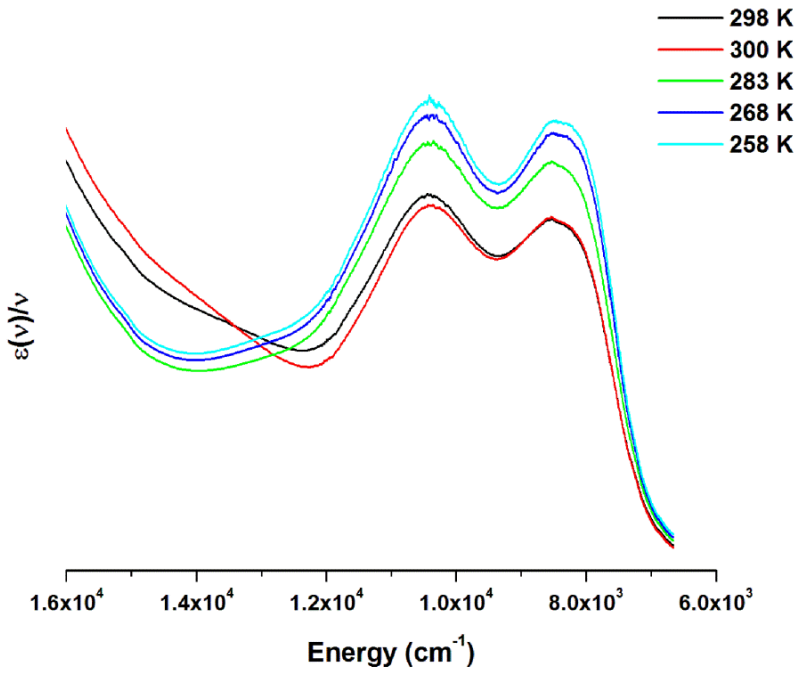

Figure 5.10. NIR region of the electronic spectra of **1** in acetonitrile at varying temperatures. Both the MBCT and MMCT increase in intensity with decreasing temperature as predicted by the three-state model, indicating that H_{ac} is increasing with lower temperatures.

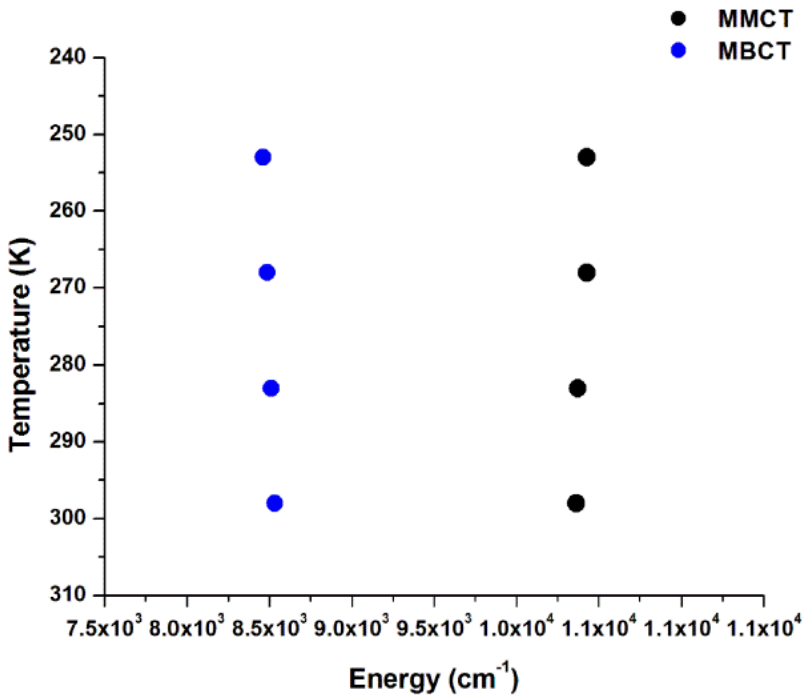

Figure 5.11. Changes in energy of the MMCT and MBCT of **1** in acetonitrile at varying temperatures. Subtle changes in the band energies indicate that the systems are only slightly more delocalized at lower temperatures.

5.3 Solvent dependence and solvent parameters.

According to classical theories by Marcus, Hush and Sutin,[41-43,45-47] the electron transfer rate constant for electron trasfer is given by:

$$k_{ET} = \kappa \nu_n \exp(-\Delta G^*/RT)$$

where κ is the adiabaticity factor, also known as the transmission coefficient, ν_n is the nuclear frequency factor, or the weighted average for all nuclear frequency modes involved in ET, and ΔG^* is the activation free energy. In symmetric mixed valence systems, the electron transfer rate constant can be rewritten as:

$$k_{ET} = \kappa \nu_n \exp\left[-(\Delta G_\lambda^* - H_{AB} - {H_{AB}}^2/4\Delta G_\lambda^*)/RT\right]$$

where ΔG_λ^* is the thermal activation barrier, and H_{AB} is the electronic coupling matrix element. The thermal activation barrier is given by:

$$\Delta G_\lambda^* = (\lambda - 2H_{AB})^2/4\lambda$$

and is dependent on the amount of electronic coupling as well as the total reorganization energy, λ. The total reorganization is a sum of the inner sphere and outer sphere term contributions:

$$\lambda = \lambda_i + \lambda_o$$

λ_i is dependent on the structural changes upon ET (vibrations), λ_o is the outer sphere contribution and includes the reorganization of the solvent, the major contribution to the total reorganization energy, λ. The outer sphere reorganization energy is given by:

$$\lambda_0 = \frac{(\Delta e)^2}{8\pi}\left(\frac{1}{\varepsilon_{op}} - \frac{1}{\varepsilon_s}\right)\int (D_A - D_B)^2 \, d\pi$$

where Δe is the charge transferred, ε_{op} is the optical dielectric constant, ε_s is the static dielectric constant and D_A and D_B are the dielectric displacement vectors of the complexes. The solvent contribution factor is $\left(\frac{1}{\varepsilon_{op}} - \frac{1}{\varepsilon_s}\right)$, also known as the Pekar factor, and the major contribution is given by the solvent static dielectric constant, which is given by:

$$\varepsilon_s = \frac{4\pi}{3} N_o(\alpha_o + \frac{\mu^2}{3KT})$$

α_o is the polarizability of the solvent, and μ represents the dipole moment of the solvent in response to an applied field. There are two main processes that affect reorganization energy for a given solvent. The first is the orientation of the permanent dipolar moments of the solvent molecules, which occurs at timescales in the order of vibrations (10^{-11} - 10^{-13}s).[48] The second is the polarization of the electronic clouds of the solvent molecules that induces temporary dipoles. Polarization occurs at a faster timescale then dipolar orientation as it corresponds to the readjustment of electronic clouds around each nuclei.[48] This indicates that the solvent static dielectric provides a good estimate of how solvent responds to ET, as it provides a parameter for how the solvent responds to the change in dipole moment brought forth by ET.[27] Good agreement (R^2 = 0.92681) between the solvent dielectric and the electrochemical splitting of the return wave was found for the solvents used in this study, as shown in Figure 5.4. Additionally ε_s describes the solvent response when the applied field is static or oscillates at frequencies less than far IR ($10^{11}s^{-1}$).[27] This serves as a additional evidence that the solvent static dielectric greatly affects the ET in these systems, which is slower than $10^{11}s^{-1}$, as indicated by the localized nature of the IR-SEC responses.

To further probe the influence on solvent on the hydrogen bonding interaction in the mixed valence ions, the electrochemical splitting of the return wave was plotted against the Gutmann acceptor number (AN) and the donor number

(DN).[49] The acceptor number measures the Lewis acidity of a solvent[50], and can also infer the hydrogen bond donor strength in the presence of Lewis bases.[50] On the other hand, the DN correlates the behavior of a solute in varying solvents with known basicities. This is obtained from the enthalpy of the reaction with a known reference,[51] and provides a measure for the solvent's ability to donate an electron pair.[52] No evident correlation between Lewis acidity and the electrochemical splitting of the return wave in the CV. Thus we can deduce from the data that it is not the hydrogen bond donor ability of a solvent that affects the splitting, but rather, it is the solvent polarity that directly affects the hydrogen bond formation.

H-bonding solvents are known to have higher λ_o because they require more energy to reorient[48], and have more basic electron pairs which allow for stronger hydrogen bonds.[52] With decreasing temperatures, the static dielectric of the solvent is expected to increase,[53] therefore disrupting the hydrogen bonding interaction.

Another solvent parameter to be considered, especially when looking at low temperatures is the solvent viscosity, η. Viscosity is a direct measure of the fluidity of the solvent, and is known to increase with lowering temperature.[54] Because viscosity is a direct measure of the fluidity of the solvent, it serves as a direct measure of the restriction of translational motion. In polar solvents and decreased temperature, motion is expected to be restricted, therefore directly impacting interactions such as hydrogen bonding as well as ET processes.[27] Sensible agreement was found between electrochemical results and the viscosity of the solvents used. Although viscosity shows reasonable agreement with the

electrochemical splitting, little translational motion of the solvent is expected in response to ET. The major reorganizational movement is expected to be the rotation of the dipole, where the solvent rotates to the correct orientation of the dipole moment with respect to the charge distribution.[27] It is important to note that dielectric relaxation is a process that involves only rotational motions while viscous relaxation involves both rotational and translational motions.[55]

5.4 Variable temperature electrochemistry

Temperature dependence of these hydrogen bonded assemblies, was investigated using variable temperature electrochemistry. The results were unusual but not surprising. The reduction side of the cyclic voltammetry showed only one quasi-reversible reduction wave at low temperatures (-30 ˚C) (Figure 5.12).

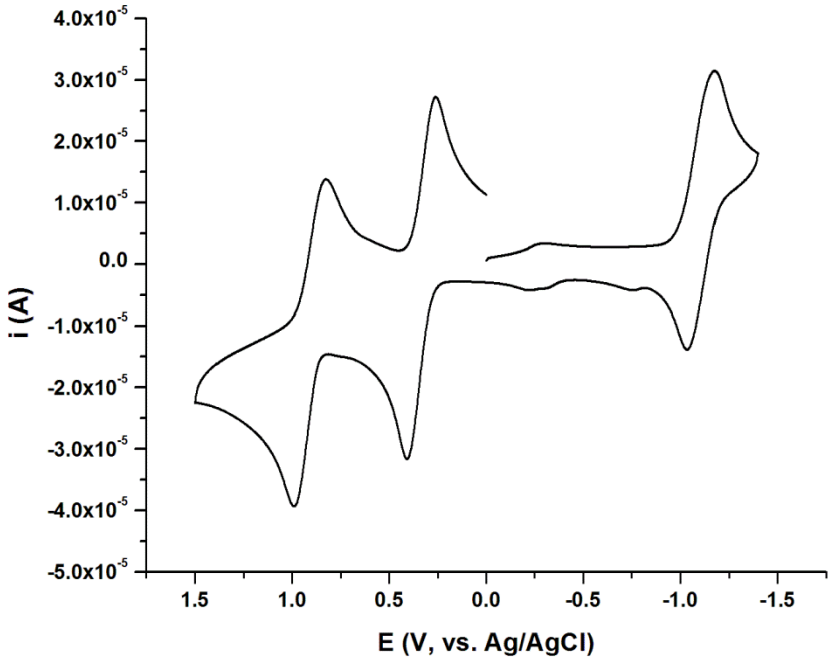

Figure 5.12. Low temperature electrochemistry (-30 ˚C) of **1** in acetonitrile at a scan rate of 100mV/s with a 3mm glassy carbon working electrode, a Pt counter electrode, and a Ag/AgCl reference. Temperature was controlled using a Neslab Endocal ULT-80 low temperature bath circulator attached to a hollow copper wire wrapped around the electrochemical cell. Temperature readings of the solution were taken with an IKA ETS-D5 digital thermometer.

This is indicative that the dimerization is affected by lowering the temperature of the solvent. This might seem contrary to general knowledge of hydrogen bonds, which are known to strengthen and shorten with temperature,[56] but our results seem to highlight that solvent choice and changes in the parameters of said solvents with varying temperature are of great importance to hydrogen bonding and are in direct competition with purely temperature effects. Effects of solvents on intermolecular hydrogen bonds have been previously shown to play an integral role

especially in polar solvents, which lead to attractive forces between non polar groups.[57] As discussed previously, good correlation was found between the electrochemical splitting in the reoxidation waves and solvent dielectric constants. As the temperature of acetonitrile is lowered the dielectric constant approaches values of over 40.[58] An increase in solvent dielectric constant, as the temperature is lowered, is also coupled to an increase in viscosity of the solvent. Viscosity's dependence on T is given by:[59]

$$\eta = Ae^{\frac{E_v}{RT}}$$

where E_v is the activation energy of viscous flow. These contributing forces disrupt the hydrogen bond bridge as reflected in the electrochemical responses. Hatton et al. have previously shown that the frictions created by dielectric and viscous changes with temperature directly affect the pre-exponential factor of reaction rates and these rates can be dependent on solvent structure and dynamics.[55] Additionally, Hatton denotes that both the dielectric relaxation time constant, τ, and ε_s exhibit Arrhenius type temperature dependence which is described as characteristic of energetic processes.[55]

Although our results indicate that there is much better correlation between the splitting and dielectric effects, it might very well be that the temperature dependence we observe is a combination of viscous and dielectric effects. While it is true that in ground state ET solvent rotational motions are more important than translational motions, changes in viscosity cannot be discarded due to the

importance of solvent translational modes on the formation of hydrogen bonded dimers.

5.5 Conclusions

The importance of electron transfer through hydrogen bonds resonates in the scientific community, with these rather simple interactions playing a fundamental role in artificial photosynthesis, biology and catalysis.[60-63] The results presented are consistent with significant electronic coupling across a large distance between two distinct clusters linked by non-covalent hydrogen-bonding interactions. These systems elucidate some important aspects of ET mediated by hydrogen bonding interactions. In particular the dependence of the electrochemical splitting on the solvent dielectric demonstrated how solvent affects these interactions, and how lowering temperatures restricts the formation of the bridging hydrogen bond. Further, we found that by analyzing the NIR region of the electronic spectra of the mixed valence ions their behavior is best described by using a semiclassical three-state model. The NIR region of the singly reduced dimers was found to show two distinct IVCT bands at room temperature, assigned to MMCT and MBCT, a result parallel to the IVCT behavior of analogous Ru_3O bridged molecular dimers.[13] These systems are classified as Class II, illustrate that large electronic couplings, and high ET rates are possible in hydrogen bonding systems where there is electronic alignment between metals and the intervening hydrogen bond bridge. Future work will seek to understand the effects of using other hydrogen-bonding moieties, as well as extending the length of these bridges and their geometric

orientation in order to examine the effects of donor-acceptor interactions in these hydrogen bonded systems.

5.6 Experimental

Synthesis and characterization

Complexes (**1** and **2**) were synthesized following previously reported techniques.[7,64] In brief, $[Ru_3O(OAc)_6(CO)(L)(H_2O)]$ (0.15 mmol), where L= 4-cyanopridine or 4-dimethylaminopyridine, was stirred in 50mL of 80% CH_2Cl_2 and 20% MeOH in an ice bath. Isonicotinic acid (nic) was added in excess (10 Eq.) as a solid over a brief period of time (usually 2-3 minutes). The reaction was allowed to come to room temperature with stirring for 48 hours. Upon completion, the reaction was dried in a rotary evaporator at a maximum temperature of 35 ºC. Using unstabilized CH_2Cl_2 the product was filtered through celite to remove excess acid. The product obtained was precipitated with excess hexanes, collected on a frit, washed extensively with hexanes, and dried overnight under vacuum. As previously reported yields were about 75-80%.

UV/vis/NIR Data Collection.

UV/vis/NIR data were collected on a Shimadzu UV-3600 UV/vis/NIR spectrometer. Samples were enclosed in a Specac sealed liquid IR cell with CaF_2 windows with 0.5 mm path length. Curve fitting of spectra to multiple Gaussian peaks was performed in Origin 6.0. Chemical reductions were performed using decamethylcobaltocene ($E^{o'}$= -1.94 vs. Fc/Fc^+)[65] as the reducing agent. Optical cryostat studies were performed using a Specac variable temperature cell holder

(Model GS21525). The temperature is controlled by addition of liquid nitrogen and subsequent heating with a computer controlled thermocouple.

***Infrared Spectroscopy*.**

Infrared spectra were obtained on a Bruker Equinox 55 spectrometer using a custom built reflectance spectroelectrochemical cell and air-tight IR cells from Specac.

***NMR Data Collection and Analysis*.**

^{1}H spectra were collected on a JEOL 500 MHz NMR spectrometer and analyzed using JEOL Delta software. Deuterated solvents were purchased and used as is from Cambridge Isotope Laboratories in Tewksbury, MA.

***Electrochemical Measurements*.**

Electrochemistry was performed with a BAS Epsilon potentiostat in dried deoxygenated solvents with 0.1 M tetrabutylammonium hexafluorophosphate (TBAH) as the electrolyte in a custom made electrochemical cell. The working electrode was a glassy carbon disk (3.0 mm diameter), the counter was a platinum wire, and the reference was a Ag/AgCl wire. . Low temperature electrochemical studies were made by wrapping a hollow copper wire around the electrochemical cell. A Neslab Endocal ULT-80 low temperature bath circulator was attached to the copper wire to control the temperature of the electrochemical cell. Temperature readings of the solution were taken with a IKA ETS-D5 digital thermometer before running any scans.

Note: Much of the material for this chapter comes directly from a manuscript entitled "On the Observation of Intervalence Charge Transfer Bands in Hydrogen-Bonded Mixed-Valence Complexes" by Gabriele Canzi, John C. Goeltz, Jane S. Henderson, Roger E. Park, Chiara Maruggi, and Clifford P. Kubiak, which has been published in *Journal of the American Chemical Society*, **2014**, *136* (5), 1710-1713. The dissertation author is the primary author of this manuscript.

5.7 References

(1) Tadokoro, M.; Inoue, T.; Tamaki, S.; Fujii, K.; Isogai, K.; Nakazawa, H.; Takeda, S.; Isobe, K.; Koga, N.; Ichimura, A.; Nakasuji, K. *Angewandte Chemie International Edition* **2007**, *46*, 5938.

(2) Meyer, T. J. *Accounts of Chemical Research* **1989**, *22*, 163.

(3) Bonin, J.; Costentin, C.; Robert, M.; Savéant, J.-M.; Tard, C. *Accounts of Chemical Research* **2011**, *45*, 372.

(4) Rege, P. J. F. d.; Williams, S. A.; Therien, M. J. *Science* **1995**, *269*, 1409.

(5) Turro, C.; Chang, C. K.; Leroi, G. E.; Cukier, R. I.; Nocera, D. G. *Journal of the American Chemical Society* **1992**, *114*, 4013.

(6) Ward, M. D. *Chem. Soc. Rev.* **1997**, *26*, 365.

(7) Goeltz, J. C.; Kubiak, C. P. *Journal of the American Chemical Society* **2010**, *132*, 17390.

(8) Wilkinson, L. A.; McNeill, L.; Meijer, A. J. H. M.; Patmore, N. J. *Journal of the American Chemical Society* **2013**.

(9) Pichlmaier, M.; Winter, R. F.; Zabel, M.; Záliš, S. *Journal of the American Chemical Society* **2009**, *131*, 4892.

(10) Westlake, B. C.; Brennaman, M. K.; Concepcion, J. J.; Paul, J. J.; Bettis, S. E.; Hampton, S. D.; Miller, S. A.; Lebedeva, N. V.; Forbes,

M. D. E.; Moran, A. M.; Meyer, T. J.; Papanikolas, J. M. *Proceedings of the National Academy of Sciences* **2011**, *108*, 8554.

(11) Glover, S. D.; Goeltz, J. C.; Lear, B. J.; Kubiak, C. P. *Eur. J. Inorg. Chem.* **2009**, 585.

(12) Glover, S. D.; Goeltz, J. C.; Lear, B. J.; Kubiak, C. P. *Coord. Chem. Rev.* **2010**, *254*, 331.

(13) Glover, S. D.; Kubiak, C. P. *Journal of the American Chemical Society* **2011**, *133*, 8721.

(14) Glover, S. D.; Lear, B. J.; Salsman, C.; Londergan, C. H.; Kubiak, C. P. *Phil.Trans. Roy. Soc. A.* **2008**, *366*, 177.

(15) Goeltz, J. C.; Benson, E. E.; Kubiak, C. P. *Journal of Physical Chemistry B* **2010**, *114*, 14729.

(16) Goeltz, J. C.; Glover, S. D.; Hauk, J.; Kubiak, C. P.; Putman, R. D.; Rauchfuss, T. B. In *Inorg. Synth.* 2010; Vol. 35, p 156.

(17) Goeltz, J. C.; Hanson, C. J.; Kubiak, C. P. *Inorganic Chemistry (Washington, DC, United States)* **2009**, *48*, 4763.

(18) Canzi, G.; Kubiak, C. P. *Small* **2011**, *7*, 1967.

(19) Canzi, G.; Kubiak, C. P. *The Journal of Physical Chemistry C* **2012**, *116*, 6560.

(20) Ito, T.; Hamaguchi, T.; Nagino, H.; Yamaguchi, T.; Kido, H.; Zavarine, I. S.; Richmond, T.; Washington, J.; Kubiak, C. P. *Journal of the American Chemical Society* **1999**, *121*, 4625.

(21) Ito, T.; Hamaguchi, T.; Nagino, H.; Yamaguchi, T.; Washington, J.; Kubiak, C. P. *Science (USA)* **1997**, *277*, 660.

(22) Ito, T.; Imai, N.; Yamaguchi, T.; Hamaguchi, T.; Londergan, C. H.; Kubiak, C. P. *Angew. Chem. Int. Ed.* **2004**, *43*, 1376.

(23) Ito, T.; Yamaguchi, T.; Kubiak, C. P. In *Macromolecular Symposia*; Wiley-VCH Press: 2000; Vol. 156, p 269.

(24) Salsman, J. C.; Kubiak, C. P. In *Spectroelectrochemisty*; Kaim, W., Klein, A., Eds.; Royal Society of Chemistry: Cambridge, 2008, p 123.

(25) Salsman, J. C.; Kubiak, C. P.; Ito, T. *Journal of the American Chemical Society* **2005**, *127*, 2382.

(26) Salsman, J. C.; Ronco, S.; Londergan, C. H.; Kubiak, C. P. *Inorganic Chemistry (Washington, DC, United States)* **2006**, *45*, 547.

(27) Lear, B. J.; Glover, S. D.; Salsman, J. C.; Londergan, C. H.; Kubiak, C. P. *Journal of the American Chemical Society* **2007**, *129*, 12772.

(28) Lear, B. J.; Kubiak, C. P. *Inorganic Chemistry (Washington, DC, United States)* **2006**, *45*, 7041.

(29) Lear, B. J.; Kubiak, C. P. *Journal of Physical Chemistry B* **2007**, *111*, 6766.

(30) Londergan, C. H.; Kubiak, C. P. *J. Phys. Chem. A.* **2003**, *107*, 9301.

(31) Londergan, C. H.; Kubiak, C. P. *Chemistry--A European Journal* **2003**, *9*, 5962.

(32) Londergan, C. H.; Rocha, R. C.; Brown, M. G.; Shreve, A. P.; Kubiak, C. P. *Journal of the American Chemical Society* **2003**, *125*, 13912.

(33) Londergan, C. H.; Salsman, J. C.; Lear, B. J.; Kubiak, C. P. *Chemical Physics* **2006**, *324*, 57.

(34) Londergan, C. H.; Salsman, J. C.; Ronco, S.; Dolkas, L. M.; Kubiak, C. P. *Journal of the American Chemical Society* **2002**, *124*, 6236.

(35) Londergan, C. H.; Salsman, J. C.; Ronco, S.; Kubiak, C. P. *Inorganic Chemistry (Washington, DC, United States)* **2003**, *42*, 926.

(36) Richardson, D. E.; Taube, H. *Coord. Chem. Rev.* **1984**, *60*, 107.

(37) Sun, H.; Steeb, J.; Kaifer, A. E. *Journal of the American Chemical Society* **2006**, *128*, 2820.

(38) Jakob, M.; Berg, A.; Stavitski, E.; Chernick, E. T.; Weiss, E. A.; Wasielewski, M. R.; Levanon, H. *Chemical Physics* **2006**, *324*, 63.

(39) Kubiak, C. P. *Inorganic Chemistry* **2013**.

(40) Walsh, J. L.; Baumann, J. A.; Meyer, T. J. *Inorganic Chemistry* **1980**, *19*, 2145.

(41) Hush, N. S. *Prog. Inorg. Chem.* **1967**, *8*, 391.

(42) Marcus, R. A. *Annu. Rev. Phys. Chem.* **1964**, *15*, 155.

(43) Brunschwig, B. S.; Creutz, C.; Sutin, N. *Chem. Soc. Rev.* **2002**, *31*, 168.

(44) Robin, M. B.; Day, P. *Adv. Inorg. Chem. Radiochem.* **1967**, *10*, 247.

(45) Brunschwig, B. S.; Sutin, N. *Journal of the American Chemical Society* **1989**, *111*, 7454.

(46) Marcus, R. A. *Angew. Chem. Int.- Ed.* **1993**, *32*, 1111.

(47) Sutin, N. J. *Prog. Inorg. Chem.* **1983**, *30*, 441.

(48) Astruc, D. *Electron Transfer and Radical Processes in Transition-Metal Chemistry*; Wiley-VCH: New York, 1995.

(49) Chastrette, M.; Carretto, J. *Tetrahedron* **1982**, *38*, 1615.

(50) Hankache, J.; Niemi, M.; Lemmetyinen, H.; Wenger, O. S. *The Journal of Physical Chemistry A* **2012**, *116*, 8159.

(51) Wypych, G. *Handbook of solvents*; ChemTec, 2001.

(52) Neyhart, G. A.; Hupp, J. T.; Curtis, J. C.; Timpson, C. J.; Meyer, T. J. *Journal of the American Chemical Society* **1996**, *118*, 3724.

(53) Shenderovich, I. G.; Burtsev, A. P.; Denisov, G. S.; Golubev, N. S.; Limbach, H.-H. *Magnetic Resonance in Chemistry* **2001**, *39*, S91.

(54) Seeton, C. *Tribol Lett* **2006**, *22*, 67.

(55) Lou, J.; Paravastu, A. K.; Laibinis, P. E.; Hatton, T. A. *The Journal of Physical Chemistry A* **1997**, *101*, 9892.

(56) Dougherty, R. C. *The Journal of Chemical Physics* **1998**, *109*, 7372.

(57) Cook, J. L.; Hunter, C. A.; Low, C. M. R.; Perez-Velasco, A.; Vinter, J. G. *Angewandte Chemie International Edition* **2007**, *46*, 3706.

(58) Shkodin, A. M. *Zh. Obshch. Khim.* **1977**, 1681.

(59) Brancker, A. V. *Nature* **1950**, *166*, 905.

(60) Hammarström, L.; Hammes-Schiffer, S. *Accounts of Chemical Research* **2009**, *42*, 1859.

(61) Magnuson, A.; Anderlund, M.; Johansson, O.; Lindblad, P.; Lomoth, R.; Polivka, T.; Ott, S.; Stensjö, K.; Styring, S.; Sundström, V.; Hammarström, L. *Accounts of Chemical Research* **2009**, *42*, 1899.

(62) Dempsey, J. L.; Brunschwig, B. S.; Winkler, J. R.; Gray, H. B. *Accounts of Chemical Research* **2009**, *42*, 1995.

(63) Sobolewski, A. L.; Domcke, W.; Hättig, C. *Proceedings of the National Academy of Sciences of the United States of America* **2005**, *102*, 17903.

(64) Morris-Cohen, A. J.; Aruda, K. O.; Rasmussen, A. M.; Canzi, G.; Seideman, T.; Kubiak, C. P.; Weiss, E. A. *Physical Chemistry Chemical Physics* **2012**, *14*, 13794.

(65) Connelly, N. G.; Geiger, W. E. *Chemical Reviews* **1996**, *96*, 877.

Chapter 6

Spectroscopic and electrochemical studies of Ru_3O clusters with π-stacking ligands

6.1 Introduction

After having described ET in hydrogen bonded assemblies we set out to study other non-covalent interactions of interest. In particular we turned our focus to π-stacking interactions because electron transport through π-stacked systems plays a vital role in materials science, biology and biochemistry.[1-7] π-π interactions are of particular importance to the field of molecular electronics and electron transport in DNA bases.[3-5,7,8] The nature of these interactions, as well as the nature of electronic coupling, $H_{ab,}$ in such systems has been of particular interest in recent years.[5,8,9] The vast majority of efforts to describe and quantify H_{ab} in these systems have been from theoretical groups.[2-5,8-11] That is not to say that many laboratories have not attempted to develop complexes that assemble through π-stacking by utilizing the strongly favorable π-π interaction. We set out to exploit that favorable π-π interaction to assemble two Ru_3O clusters in solution. As shown in Chapter 5, electron density and electronic delocalization stabilizes non-covalent hydrogen

bonding interactions, and surprisingly large electronic couplings can be observed in such systems.[12,13] Using a long extended π ligand framework, 4-phenylethynyl pyridine (PEP), as the basis for our ancillary ligand "bridge", we were curious to see if the same is true for π-stacking interactions.

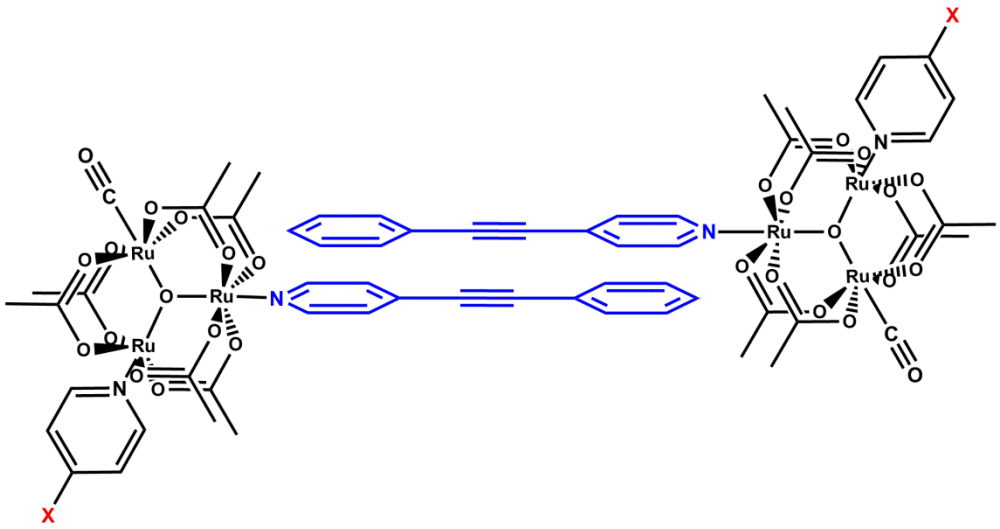

Figure 6.1. Schematic showing the expected π-π interaction between two clusters in solution.

Herein we describe the synthesis, electrochemistry, and spectroscopic behavior of these newly prepared Ru_3O clusters. We use tri-nuclear metal clusters of the form $[M_3O(OAc)_6(L)_3]$ where M = metal and L = ancillary ligand because these clusters have been subject to extensive research in the last 50 years.[14-21] The ruthenium version of these clusters have been used in our laboratory in the last two decades and have been extremely useful due to their rich redox chemistry, as well as the ability to be assembled in oligomers.[21,22]

6.2 Results and discussion

Synthesis

All complexes synthesized for this chapter are derived from the parent solvento specie $[Ru_3O(OAc)_6(S)_3]^{+1}$ where S= is coordinated solvent, either H_2O or MeOH in our case. The ancillary PEP ligands were synthesized using simple Sonogashira coupling reaction conditions.[23-25] This cross-coupling reaction allows for the formation of new carbon-carbon bonds between terminal alkynes and aryl halides in the presence of a Pd(II) and CuI.[24,26,27]

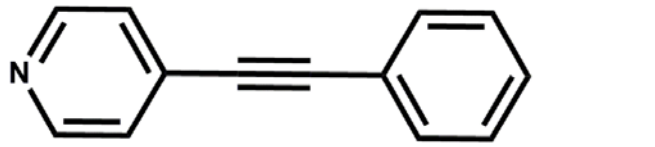

4-(phenylethynyl)pyridine (PEP)

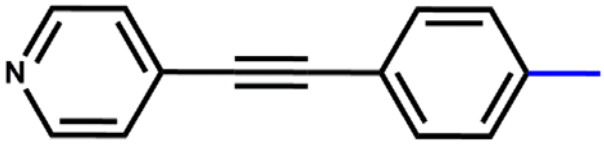

4-(*p*-tolylethynyl)pyridine (MePEP)

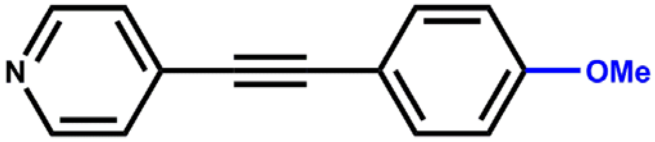

4-((4-methoxyphenyl)ethynyl)pyridine
(MeOPEP)

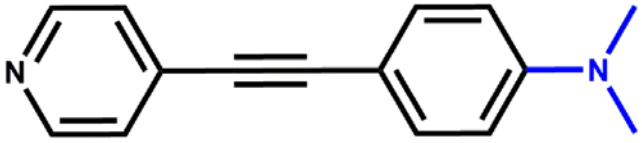

N,N-dimethyl-4-(pyridin-4-ylethynyl)aniline
(DMAP-PEP)

Figure 6.2. Series of ligands used in these studies. 4-phenylethynyl pyridine (PEP) is used as the backbone and functional groups substitutions are made at the *para* position of the phenyl ring. The substituents are shown in increasing donor ability.

The role of the Pd(II) source is well understood, while the mechanistic involvement of the Cu is still very fuzzy.[27]

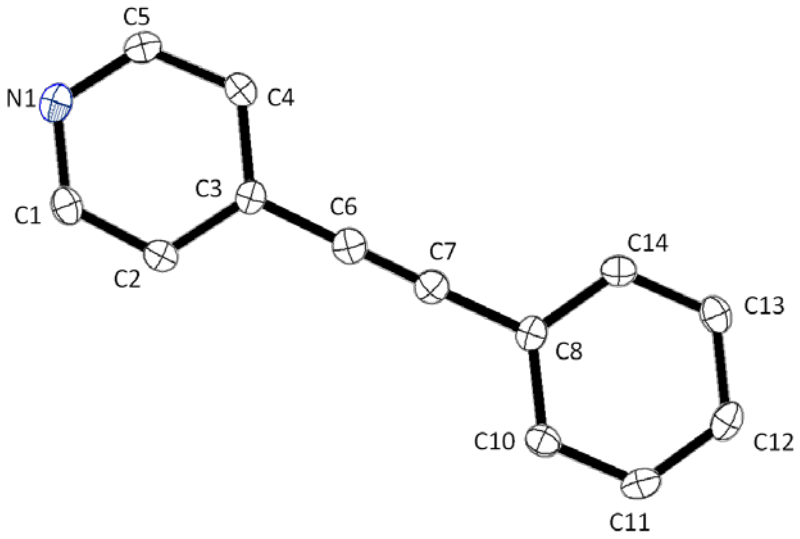

Figure 6.3. Molecular structure of 4-(phenylethynyl)pyridine (PEP). Hydrogen atoms are omitted for clarity. Ellipsoids are set at 50% probability.

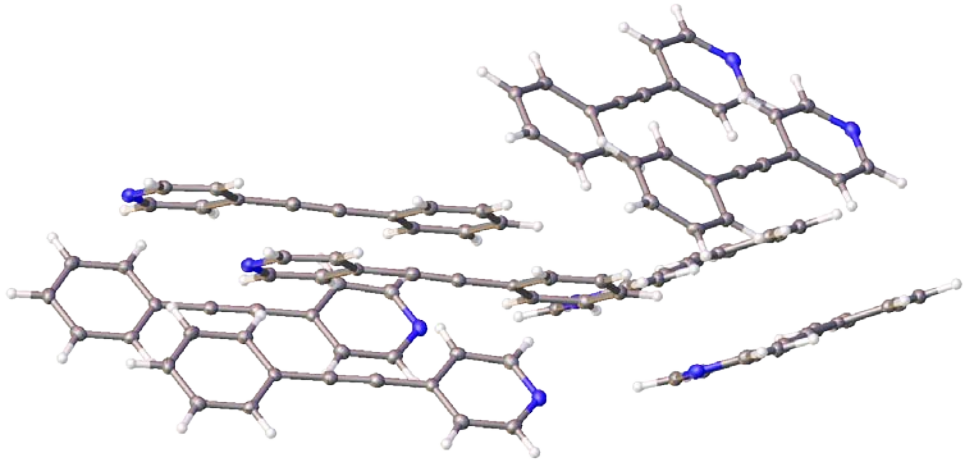

Figure 6.4. Crystal packing of 4-(phenylethynyl)pyridine. Hydrogen atoms are omitted for clarity. Ellipsoids are set at 50% probability. Two PEP units are stacking in solution as expected.

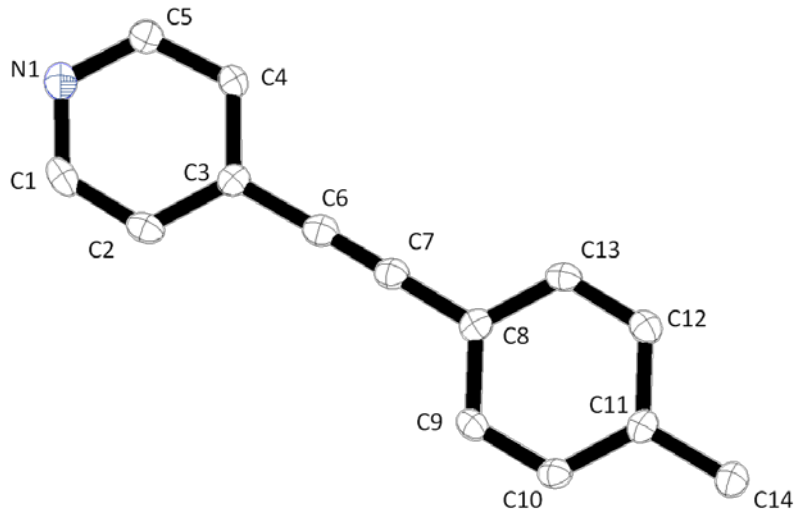

Figure 6.5. Molecular structure of 4-(p-tolylethynyl)pyridine (Me-PEP). Hydrogen atoms are omitted for clarity. Ellipsoids are set at 50% probability.

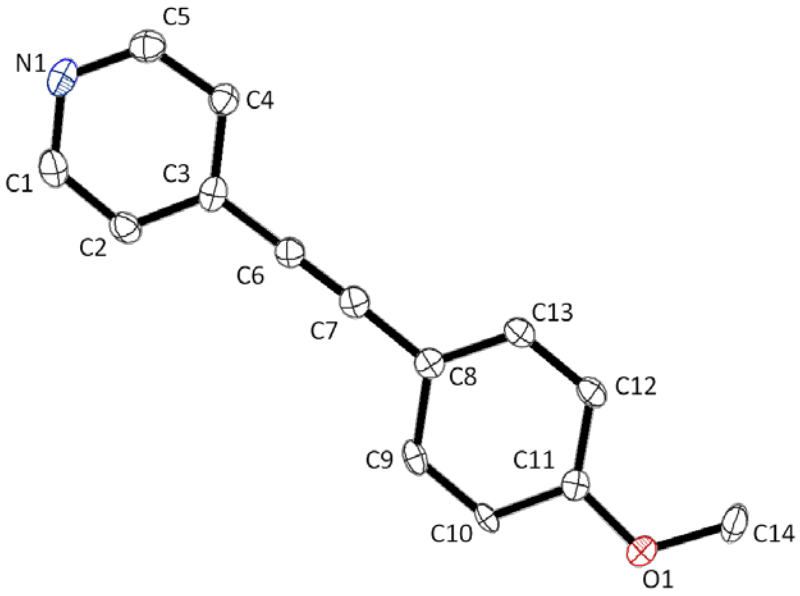

Figure 6.6. Molecular structure of 4-((4-methoxyphenyl)ethynyl)pyridine (MeO-PEP). Hydrogen atoms are omitted for clarity. Ellipsoids are set at 50% probability.

The triply substituted clusters (**8-10**) were derived by simply reacting under reflux the parent complex with the desired PEP ligand in the presence of hydrazine

monhydrate as the reducing agent. Reducing the parent solvento cluster with less than one equivalent of borohydride and pressurizing the reaction vessel with CO, one of the solvent molecules is displaced by a CO. The CO substituted Ru_3O clusters, as has been shown in all previous chapters, have been extremely useful in the work performed in the Kubiak laboratory.[12,13,21,22,28-42] The doubly substituted complexes (**5-7**) are synthesized from the $[Ru_3O(OAc)_6(CO)(S)_2]$ by adding excess ancillary ligand. The asymmetric clusters (**1-4**) were synthesized by first adding the ancillary pyridyl ligands to $[Ru_3O(OAc)_6(CO)(S)_2]$ and after purification adding excess PEP bridge.

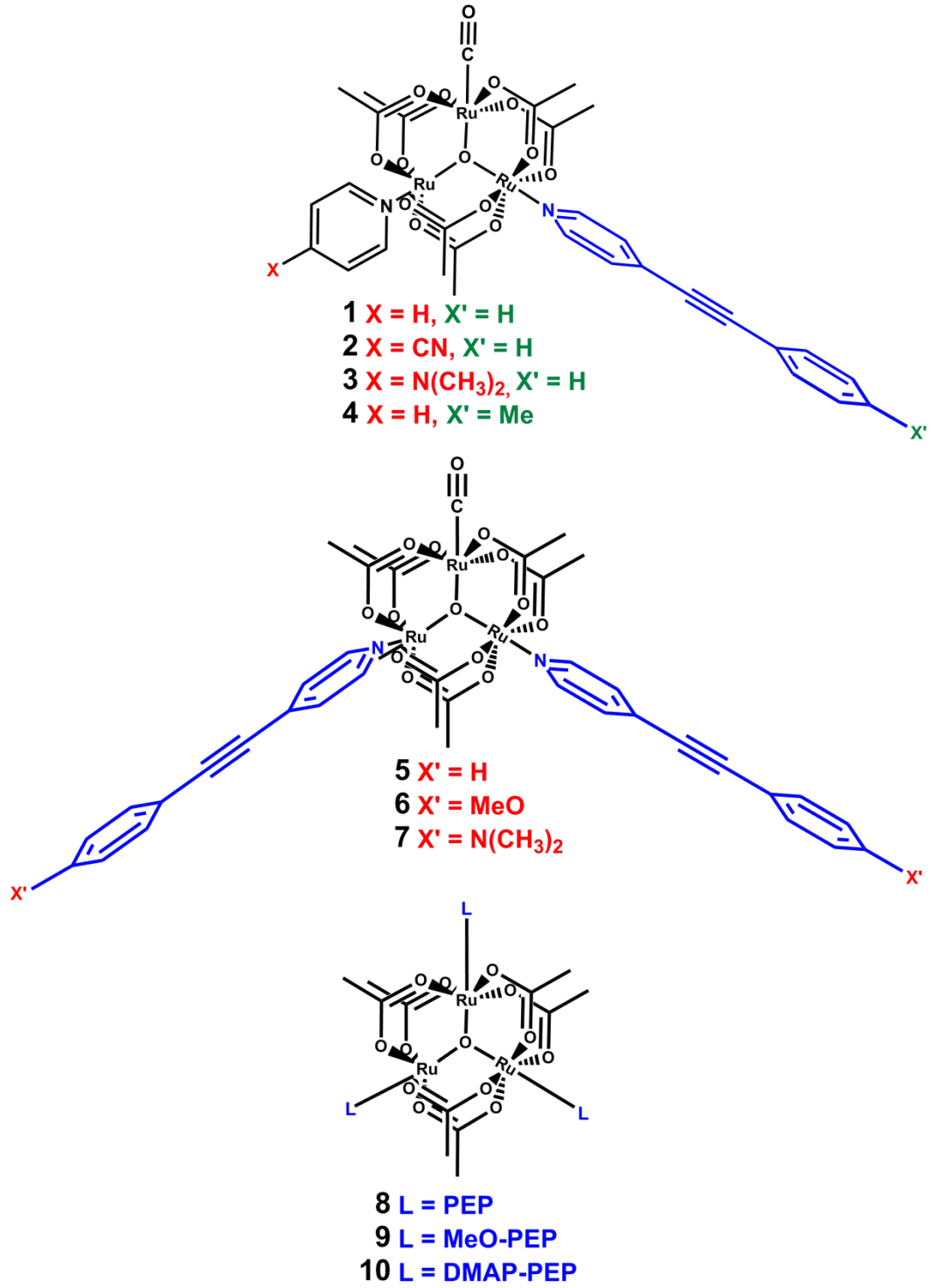

Figure 6.7. Structures of the Ru_3O systems used in this study. **1-4** are asymmetric systems with pyridine ancillary ligands. **5-7** are doubly substituted clusters with a CO ligand. **8-10** Triply substituted clusters with symmetric ligand substitution.

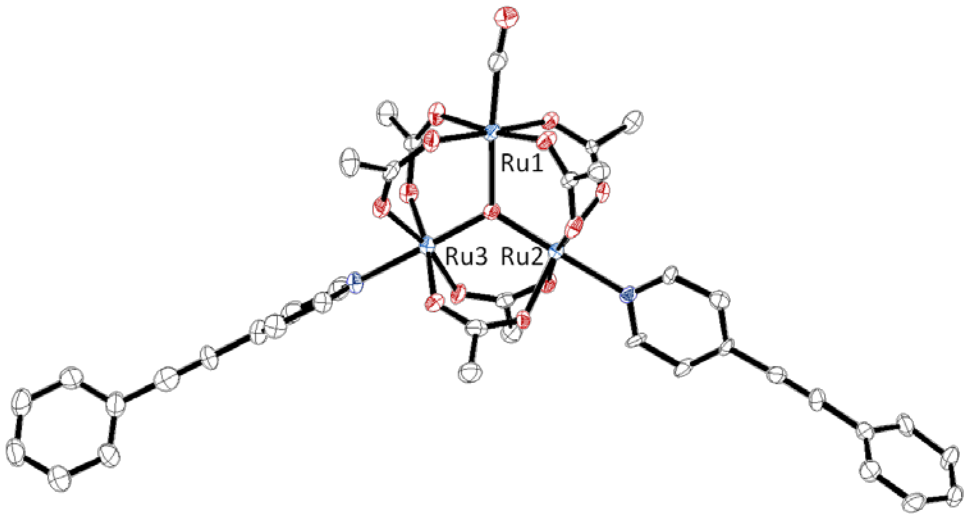

Figure 6.8. Molecular structure of $Ru_3O(CO)$[4-(phenylethynyl)pyridine]$_2$, ($[Ru_3O(CO)(PEP)_2]$), hydrogen atoms are omitted for clarity. Ellipsoids are set at 50% probability.

Electrochemistry

The electrochemistry of these assemblies is particularly telling of the overall mechanism for the ground state ET reaction. The oxidative side of the cyclic voltammetry features two reversible single electron oxidations, indicating changes in the Ru oxidations states from $Ru^{III,III,II}/Ru^{III,III,III}$ and, because Ru (IV) is stabilized by the oxo center, $Ru^{III,III,III}/Ru^{III,III,IV}$. In the reductive side, two distinct reversible one electron reductions are apparent. This is somewhat surprising as only one metal based reduction is usually observed in the electrochemical responses of $Ru_3O(CO)(L)(L')$ and $Ru_3O(CO)(L)_2$ complexes.[18-20]

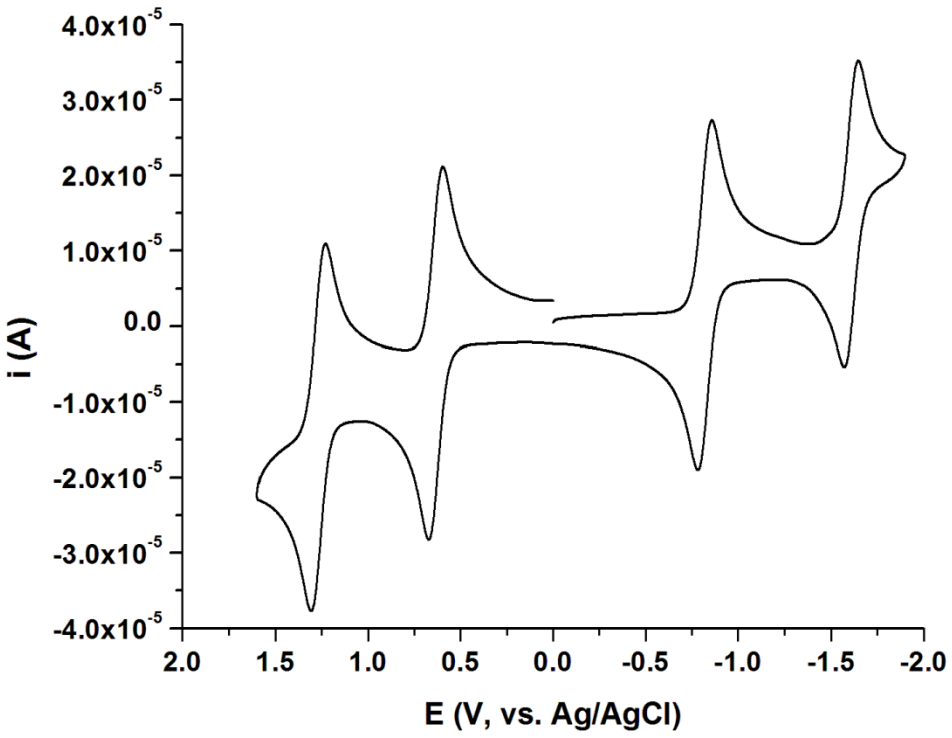

Figure 6.9. Electrochemical response of **1** (0.3mM) in acetonitrile with 0.1M TBAH as the supporting electrolyte at a scan rate of 200mV/s with a 3 mm glassy carbon working electrode, a Pt counter electrode, and a Ag/AgCl reference.

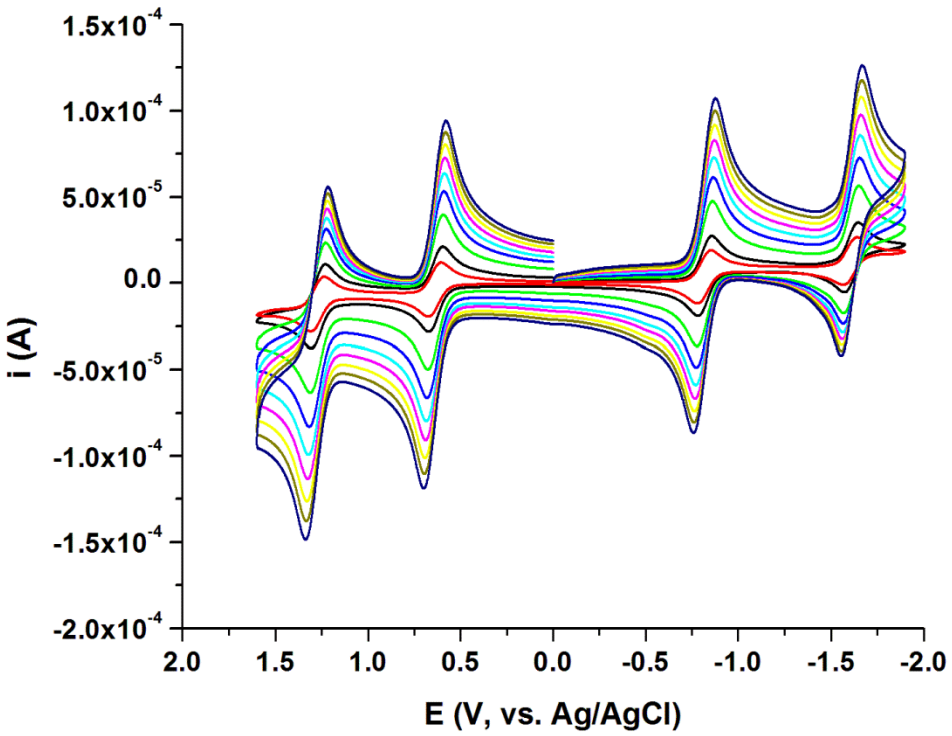

Figure 6.10. Scan rate dependence of complex **1**. Scan rates from 100mV/s to 2000mV/s, with 0.3mM cluster concentration, 0.1M TBAH, with a 0.3mm GC working electrode, Pt wire counter electrode, and a Ag/AgCl wire as the reference electrode.

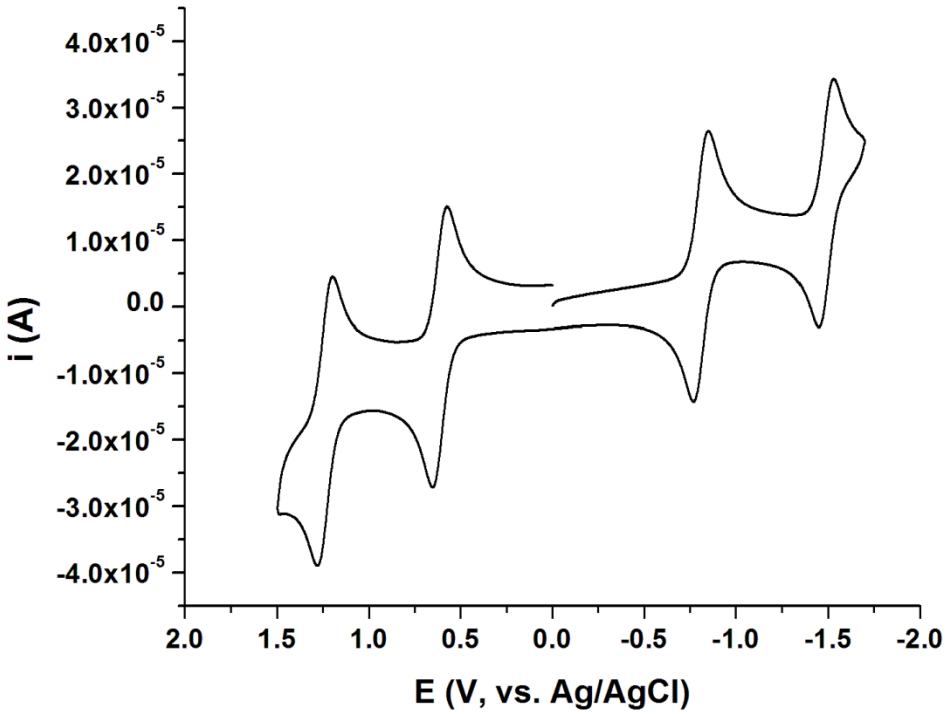

Figure 6.11. Electrochemical response of **5** (0.3mM) in acetonitrile with 0.1M TBAH as the supporting electrolyte at a scan rate of 200mV/s with a 3 mm glassy carbon working electrode, a Pt counter electrode, and a Ag/AgCl reference.

Meyer reported in 1978 that in dry acetonitrile for complexes of the form $[Ru_3O(OAc)_6(L)_3]$ both 0/-1 and -1/-2 couples were observed to be reversible.[19]

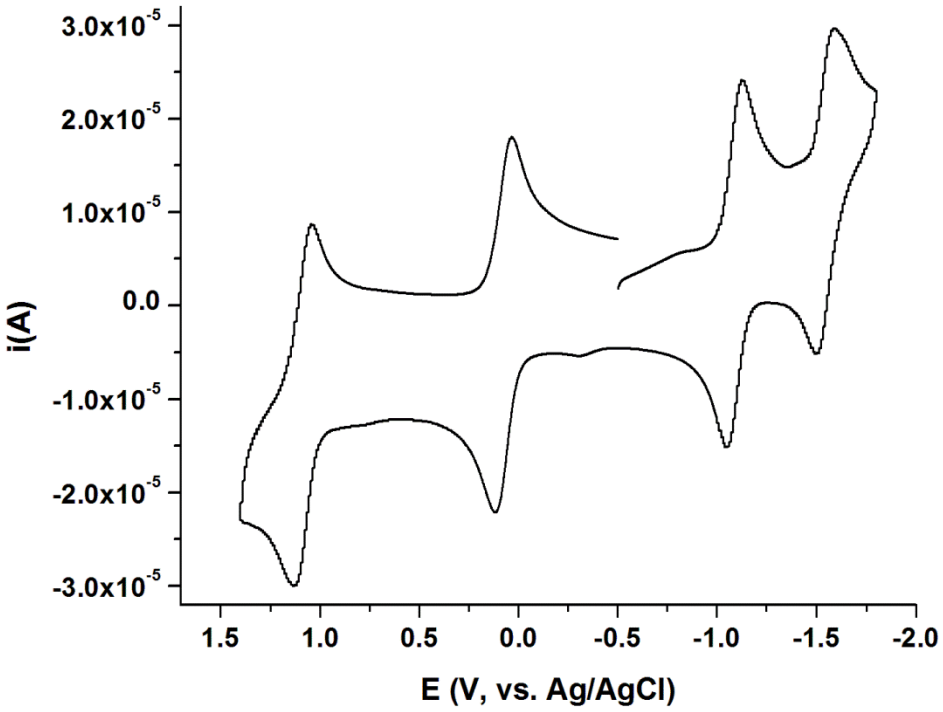

Figure 6.12. Electrochemical response of **8** (0.3mM) in acetonitrile with 0.1M TBAH as the supporting electrolyte at a scan rate of 200mV/s with a 3 mm glassy carbon working electrode, a Pt counter electrode, and a Ag/AgCl reference.

They argue that the -1/-2 couple is ligand based due to the fact that the $E_{1/2}$ track with the ease of reduction of the free ligand. The second reduction observed in our system (**1**-**7**) cannot be ligand based as we observe the ligand reduction when we scan more negatively (Figure 6.13). The electrochemical responses suggest that second reduction is metal based.

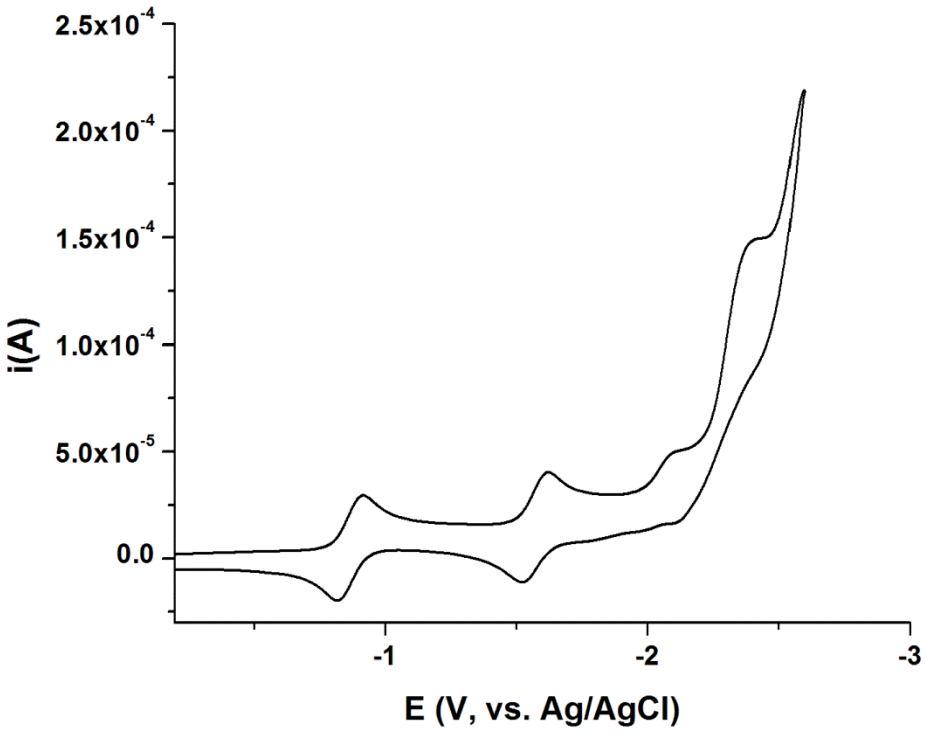

Figure 6.13. Electrochemical response of **5** (0.3mM) in DMF with 0.1M TBAH as the supporting electrolyte at a scan rate of 200mV/s with a 3 mm glassy carbon working electrode, a Pt counter electrode, and a Ag/AgCl reference. The reductions of the ligand are apparent at -2.1 V and -2.3 V.

This clearly indicates that we have two possible scenarios. The first could be that the -1/-2 couple is indeed metal based but is strongly susceptible to ancillary ligand substitution, therefore widely varying depending on the electronics of the clusters. The other case would be that the second reduction peak in the electrochemical responses corresponds to a metal based reduction caused by the formation of a thermodynamically stable mixed valence state due to π-π interactions between the phenylethynyl ligands. The splitting is extremely large for such a weak interaction,

even larger than the splitting observed in molecularly bridges systems. In molecularly bridged dimer systems the splitting in the reduction waves is mostly due to electronic delocalization between the two metal centers. The splitting in this case is too large to be solely due to electronic coupling, we believe that it is due to a combination of factors as we will explain in the following section of this chapter.

Table 6.1 Electrochemical splitting in mV of the reduction waves for complexes **1-9**

Complex	***Splitting***
1	774
2	550
3	820
4	798
5	671
6	718
7	743
8	472
9	485

6.3 Comproportionation constant (K_c) for mixed valence ion

The observed splitting of the reduction waves in the cyclic voltammetry is indicative of the comproportionation constant, K_c, for a mixed valence ion. The large splitting is attributed to the increased electronic communication between clusters and the formation of a thermodynamically stable mixed valence state due to strong π-π interactions. K_c is given by $K_c = e^{\frac{nF\Delta E_{\frac{1}{2}}}{RT}}$, which is obtained from the simple relationship, $\Delta G^o = -nFE = -RT(\ln K_c)$.

For a mixed valence compound that resides in the classical class I, K_c is expected to be low.[43] It has been shown in the past that the comproportionation constant can be obtained from electrochemical and spectroscopic measurements, with four major components being identified to break down the contributions to the comproportionation free energy.[43-45] There is a statistical contribution, an electrostatic factor, which arises from the repulsion of the two bridged metal centers, a synergistic factor due to metal-metal backbonding, and a resonance stabilization factor due to electronic delocalization. Our group has shown in the past that for molecular dimers-of-trimers systems that the statistical, synergistic, and electrostatic factors are about the same for all of molecular dimers, meaning that in highly coupled systems that reside at the class II/III borderline the delocalization factor is the main contribution in the reduction potential differences observed.[44,46] On the other hand, in a localized, moderately coupled class II system the synergetic factor is expected to predominate, as all the other contributions are weak.[43] This

indicates that in such systems the stabilization of one of the redox states is the main contribution to the comproportionation free energy.

As shown in Table 6.1, ancillary ligand substitution affects the splitting in the electrochemical responses. Complexes **1-3** show a trend with increasing donor ability of the ancillary ligand on the splitting. This illustrates a clear dependence on the electronic properties of the pyridyl ancillary ligands. An cluster having an electron withdrawing ligand such as 4-cyanopyridine (CPY), **2**, is shown to have the smallest splitting, while a cluster having the most electron donating ligand, 4-dimethylaminopyridine (DMAP), **3**, shows the largest splitting between reduction waves. This indicates that with more donating ligands additional electron density is available on the cluster and can be "pushed" onto the adjacent PEP ancillary ligand. The increased electron density will then increase the strength of the π-π interaction. This will lead to a greater stabilization which subsequently results in increased electrochemical splitting. Additionally, substitution at the *para* position on the PEP ligand affects the splitting in a similar way as ancillary ligand substitution. Comparing the splitting in the reduciton waves for complexes **1** and **4** and **5-7** we can see that there is a clear trend between the magnitude of splitting and activating ability of the substituent group at the *para* position of the phenyl ring. The weakly activating CH_3 group shows the least amount of splitting, followed by the moderately activating MeO, and finally the strongly activating $N(CH_3)_2$ group. This indicates that increasing the donor ability of the R group on the phenyl ring increases the delocalization of charge onto the whole PEP framework. This

additional electron density strengthens the π-stacking interaction, and increases the observed splitting in the electrochemical responses.

6.4 Solvent dependence of electrochemical responses

Hunter and Sanders in 1990 developed a model to clearly describe the nature of the π-π interaction.[47] They showed, with the aid of ab initio studies, that π-π interactions can be simply represented as a positive σ-framework sandwiched by two π electrons.[47] Their findings clearly showed that π-π interactions are controlled by electrostatics, but there are other major factors that also have to be taken in consideration.[47] van der Waals interactions were found to be extremely important and greatly contribute to the magnitude of the observed interaction. Since we expect electrostatics to provide a large contribution to the π-π interaction, we expect solvent choice to directly affect the strength of that interaction. We have shown previously that the electron transfer rate in symmetric mixed valence ions is given by:[36,48]

$$k_{el} = \kappa \nu_n \exp\left[\frac{-(\Delta G_\lambda^* - H_{ab} + H_{ab}^2)}{\frac{4\Delta G_\lambda^*}{RT}}\right]$$

and that the reorganization energy, λ, which is part of the ΔG^* term is described as $\lambda = \lambda_i + \lambda_o$, where λ_i is the innersphere reorganization energy concerned with the molecular rearrangement upon ET and λ_o the outersphere reorganization energy which represents the energy contributions of the solvent to the barrier for ET and is given by:[36,48]

$$\lambda_o = \frac{(\Delta e)^2}{8\pi}\left(\frac{1}{\varepsilon_{op}} - \frac{1}{\varepsilon_s}\right)\int (D_A - D_B)^2 d\tau$$

where Δe is the energy transferred, ε_{op} is the optical dielectric, ε_s is the static dielectric constant, and the integral represents the ET distance. As discussed in previous chapters the only variable portion of λ_o is the $\left(\frac{1}{\varepsilon_{op}} - \frac{1}{\varepsilon_s}\right)$ term. Since λ_o contributes to the barrier for ET, there is normally good correlation between the solvent dependent parameters and ET rates in mixed valence complexes.[28-31,36] Since we know that ET in these systems is slower than picoseconds, we focused on the ε_s term because it describes how changes in the dipole moment upon ET affect the nature of the solvent. In particular it describes the response to an applied field that is oscillating slower than $10^{-11}s^{-1}$.[30,36] We believe that the static dielectric would provide the best metric for demonstrating how solvent affects the electrostatics of the π-π interaction. ε_s is given by:[36]

$$\varepsilon_s = \frac{4\pi}{3}N_o\left(\alpha_o + \frac{\mu^2}{3KT}\right)$$

where μ is the dipole moment orientation response to an applied field, α_o is the polarizability of the solvent itself. Good agreement between the dielectric constant of the solvents used in this study versus the magnitude of the splitting of the reduction waves is found. Figure 6.14 illustrates that more polar solvents, having large dielectric constants, have a bigger role in disrupting the electrostatic π-stacking interaction yielding to lower degrees of splitting. Less polar solvents,

having small dielectric constants, interfere less with the π-stacking interaction and show larger splittings in the electochemical responses.

Table 6.2 Electrochemical splitting in mV of the reduction waves for complex **5** in the solvents used in this study and selected solvent parameters

Solvent	**Splitting (mV)**	**Dielectric**	**D**	**E_T**
THF	803	7.58	1.75	37.4
DCM	743	8.93	1.6	40.7
ACN	671	37.5	3.92	45.6
DMF	699	36.7	3.82	43.2
DMSO	665	46.7	3.96	45.1

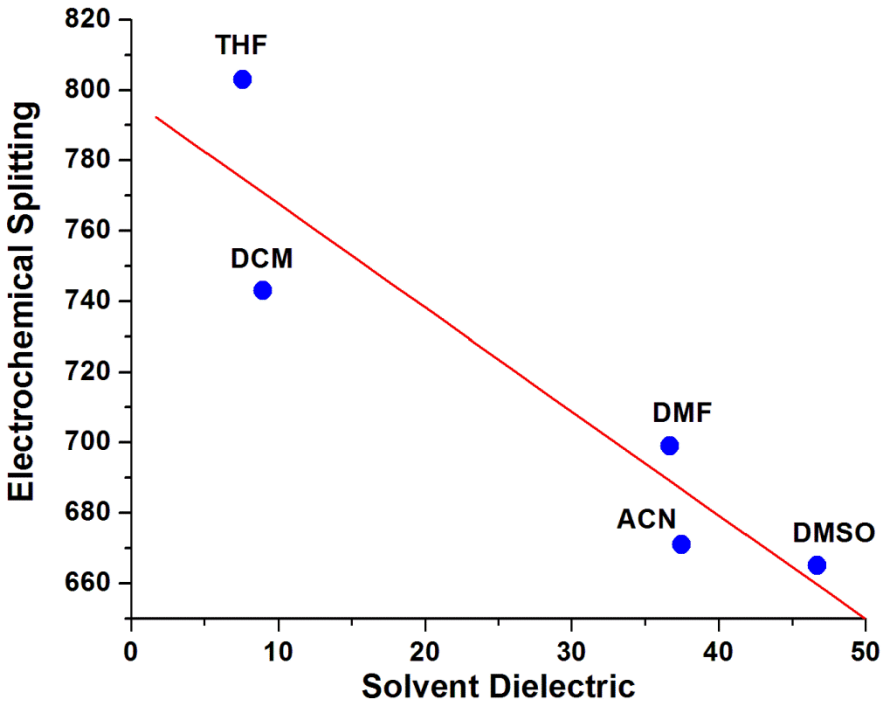

Figure 6.14. Plot of solvent dielectric versus electrochemical splitting (in mV) between the reduction waves of complex **5**.

Dielectric constants are not the only measure of solvent polarity, therefore we looked at other solvent thermodynamic parameters including the solvent dipole moment, and the microscopic solvent polarity.[36] We know that the electron transfer event causes a response in the solvent due to the change in charge distribution.[36] Therefore we focused on this response by investigating the effects of the microscopic polarity of the solvents with the electrochemical splitting. As shown in Figure 6.16, excellent agreement (R^2 = 0.995) was found. This further strengthens our conclusion that the splitting observed in the electrochemical responses is in part

due to the π-π interaction between the two clusters upom ET, and that the microscopic polarity of the solvent directly affects the strength of the interaction.

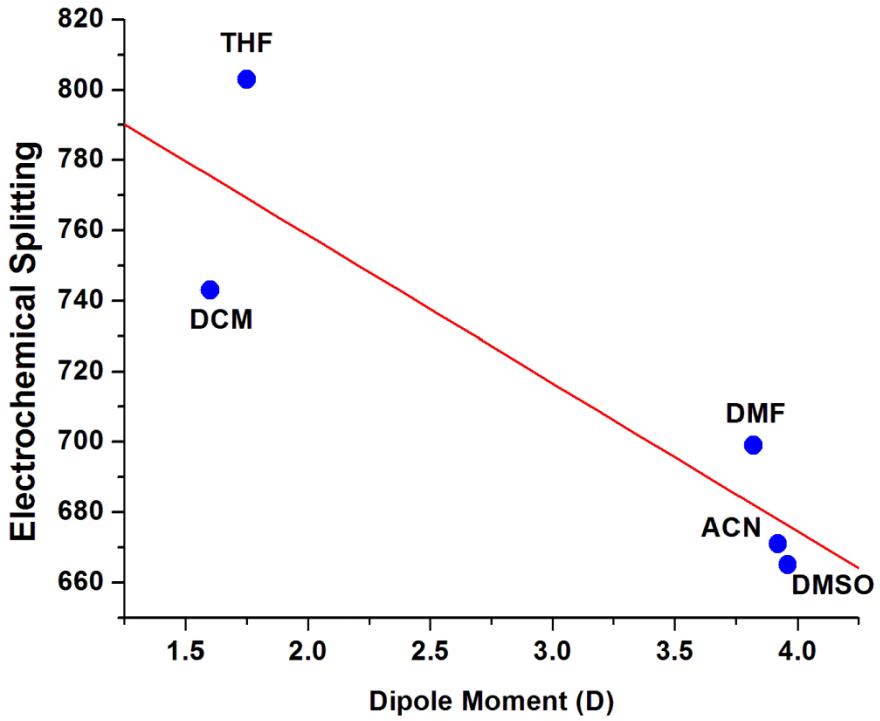

Figure 6.15. Plot of solvent dipole moment (D) versus electrochemical splitting (in mV) between the reduction waves of complex **5**.

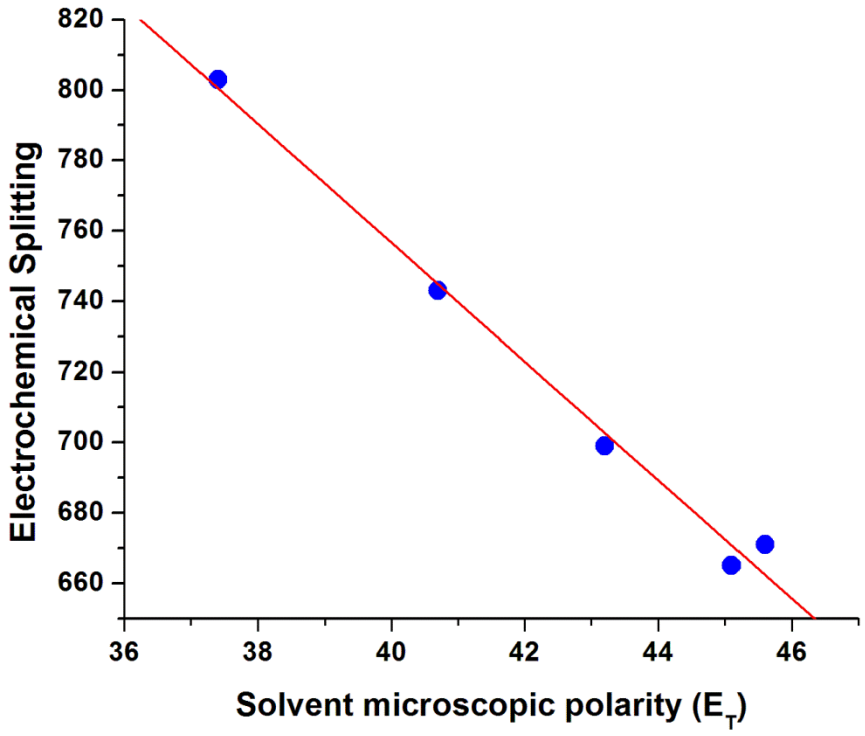

Figure 6.16. Plot of solvent microscopic polarity (E_T) versus electrochemical splitting (in mV) between the reduction waves of complex **5**.

Electronic Spectroscopy

Electronic absorption spectra for these systems is analogous to previously reported ruthenium monomers.[18-20] Clusters of the type $[Ru_3O(OAc)_6(CO)(L)_2]$ and $[Ru_3O(OAc)_6(CO)(L)(L')]$ have strongly absorbing bands in the near and middle UV. Higher energy bands from 200-350nm are very intense and are typically assigned as π-π^* transitions.[39] A band at 400-450nm is present and is usually assigned as metal-to-ligand charge transfer (MLCT), and is due to Ru_3O cluster π to ancillary ligand π^* transitions.[39] This band is sensitive to ancillary ligand

substitution as shown in Figure 6.17. An additional lower energy broad band is present at 550-650nm, and is assigned as intracluster charge transfer band (ICCT) and is due to Ru dπ and O p mixing.[39] On the contrary to the MLCT, this band is found to be insensitive to ancillary ligand substitution. This is clearly shown in Figures 6.17 and 6.18. The effects of ancillary ligand substitution on the clusters energetics have been previously reported and discussed by our laboratory.[29,32,36,39] The pyridyl ligands shift the energy levels of the Ru clusters based on their donor ability.[28,29,36,39] With more electron donating ligands MLCT transitions are more intense and are blue shifted.

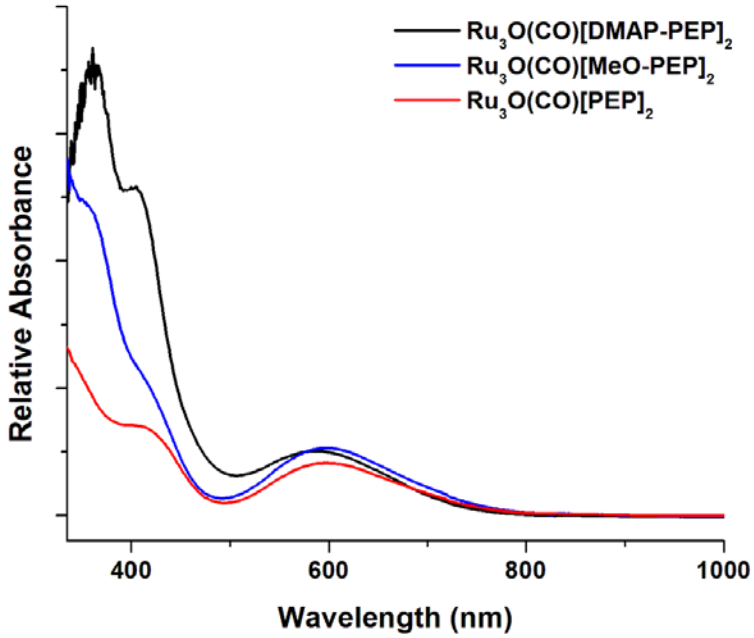

Figure 6.17. UV-vis of neutral doubly substituted clusters (**5-7**) showing differences in intensity of MLCT band upon ancillary ligand substitution and insensitivity of ICCT to ancillary ligand substitution.

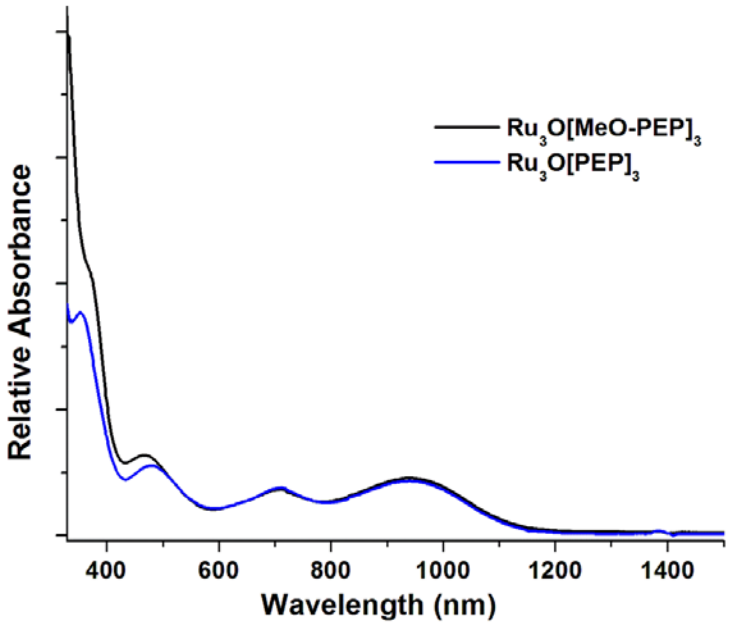

Figure 6.18. UV-vis of neutral triply substituted clusters (**8-9**). Low energy bands are observed and represent cluster excitations from low energy d-Ru levels.

Triply substituted symmetric $[Ru_3O(OAc)_6(L)_3]$ clusters have been shown to have very different electronic structure than CO clusters, mostly due to the backbonding between the Ru and the CO.[19] The optical spectra for symmetric triply substituted clusters exhibit high energy bands which are assigned as π to π^* pyridine in addition to the aforementioned MLCT band. Low energy bands are also observed for these clusters and are consistent with literature precedent.[19] These low energy bands were first observed by Meyer in 1978 and tentatively assigned as cluster excitations from low energy d-Ru levels.[19]

Upon a single electron reduction of the clusters, using a chemical reducing agent, 2e observe a shift and intensification of the ICCT band, a dampening of the

MLCT, and characteristic bands appear in the NIR region as shown in Figure 6.19. The NIR region has been fit to multiple bands and the band profile suggests two bands, not an asymmetric CT band as might be expected in moderately coupled systems described by a Marcus-Hush two-state formalism.[49-53] These bands have been tentatively assigned as allowed MLCT bands by Meyer,[19,20] although further investigation into the nature of these *two* bands is necessary. No change in these NIR bands was observed between acetonitrile and methylene chloride, consistent with the electron and solvent localized Robin Day class II nature of these dimers.[54]

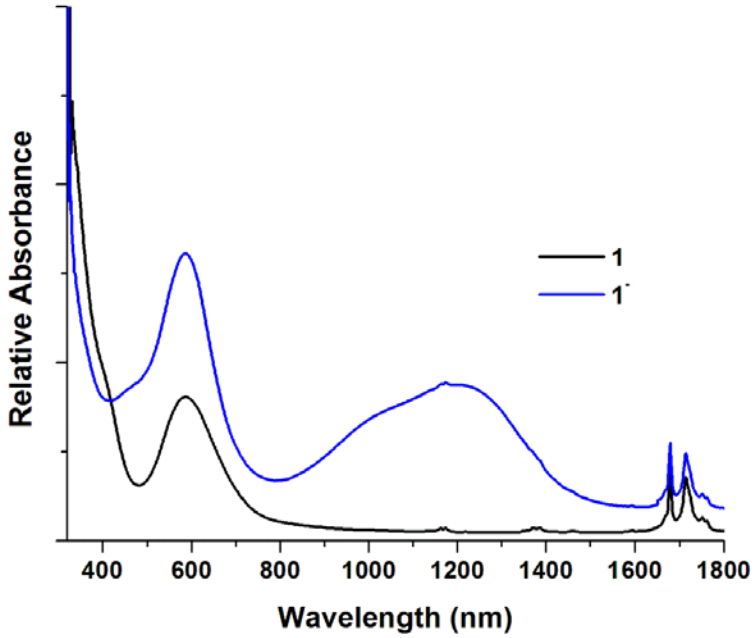

Figure 6.19. UV/vis/NIR spectra of **1** and its reduced form **1**$^{-}$ (3mM) in DCM. Upon reduction two large bands are observed in the NIR region.

6.5 Conclusions.

Complexes **1-10** have been characterized spectroscopically and electrochemically and are shown to exhibit very interesting behavior in solution upon a one electron reduction of the metal center. Electrochemical responses show two reduction waves that are metal based as opposed to the single reductive wave that would be expected for $[Ru_3O(OAc)_6(CO)(L)(L')]$ and $[Ru_3O(OAc)_6(CO)(L)_2]$ systems.[19,32,34] The splitting observed in the cyclic voltammograms is unusually large and is attributed to a combination of electrostatics and electronic delocalization factors due to strong π-π interactions. Since these systems are not Robin and Day Class III,[54] the large K_c values are mostly due to electrostatics with a smaller contribution from electronic delocalization, as opposed to highly coupled systems where electronic delocalization is the main contributor to the comproportionation constant.[36] The presence of some electronic coupling in these systems should not be unexpected, as we have shown in Chapter 5 that considerable electronic coupling can be present and strengthen otherwise weak non-covalent interactions.

There is undoubtedly more work to be done to fully hammer out all of the specifics and subtleties of these very interesting systems. This serves as a good introduction to the possibility of using π-stacking to create higher order supramolecular strucutres. Although this chapter comes to an end by no means is this the end of this project. There are so many more things to learn about the systems discussed here. The more we learn the less we seem to know. I am

particularly fond of the ET across weak interactions work. I think that studying other hydrogen bonding groups or ET across multiple hydrogen, as discussed in Chapter 5, bonds would be of high impact. The π-stacking work is also of high interest and begs for more systematic studies of some of the fundamental properties of these systems. This chapter has barely scratched the surface, and these complexes have proved to be quite interesting, although at times challenging to work with.

6.6 Experimental

General

All chemicals were used as received unless otherwise noted. Electrochemistry and spectroscopy solvents were sparged with argon and dried over alumina.

Synthesis and characterization

The bridging ligands were synthesizes using a modified Sonogashira coupling reaction with reduced homocoupling.[23] In brief, 4-bromopyridine, bis(triphenylphopshine)palladium(II) chloride, and CuI were added in a flask and degassed by three consecutive freeze-pump-thaw cycles. TEA was added to the reaction mixture, and subsequently phenyl acetylene was added to the reaction mixture in ACN. The mixture was allowed to react with stirring over 72hrs. Upon drying, the product was extracted using column chromatography with 95-5% hexanes-ethyl acetate.

4-phenylethynylpyridine **(PEP)** ^{1}H NMR ($CDCl_3$, 500 MHz): δ (ppm)= 8.59 (d,2H); 7.55 (d,2H); 7.38 (m, 5H) IR: 2226 cm^{-1} ν(CC) Single crystals suitable for XRD studies were obtained by vapor diffusion of ACN/ether.

4-(p-tolylethynyl)pyridine (Me-PEP) ^{1}H NMR ($CDCl_3$, 500 MHz): δ (ppm)= 8.57 (d,2H); 7.43 (d,2H); 7.35 (d, 2H); 7.17 (d,2H); 2.35 (s,3H) Single crystals suitable for XRD studies were obtained by vapor diffusion of ACN/ether.

4-((4-methoxyphenyl)ethynyl)pyridine (MeO-PEP) ^{1}H NMR ($CDCl_3$, 500 MHz): δ (ppm)= 8.57 (d,2H); 7.49 (d,2H); 7.35 (d, 2H); 6.91 (d,2H); 3.84 (s,3H) Single crystals suitable for XRD studies were obtained by layering of ether and frozen CH_2Cl_2.

N,N-dimethyl-4-(pyridin-4-ylethynyl)aniline (DMAP-PEP) ^{1}H NMR ($CDCl_3$, 500 MHz): δ (ppm)= 8.56 (d,2H); 7.41 (d,2H); 7.33 (d, 2H); 6.65 (d,2H); 3.02 (s,6H) Single crystals suitable for XRD studies were not obtained despite numerous attempts.

Synthesis of substituted Ru3O clusters.

The asymmetric substituted oxo-centered ruthenium clusters were synthesized using previously published procedures.[13,32-35,37-39] The singly substituted $Ru_3O(CO)(L)(S)$ clusters are easily synthesized by adding 0.8 equivalents of desired ligand to the parent $Ru_3O(CO)(S)_2$ cluster, where S = solvent molecule. Once the complex is purified with column chromatography (99-1% chloroform to methanol)

the PEP bridges are added in small excess (10Eq.) in an ice bath and allowed to react overnight with stirring. The complexes are filtered through celite, crashed out in hexanes and filtered on a medium porosity fritted glass filter. The product is then washed copiously with hexanes and rinsed with ether. Usual yields range from 55 to 65%.

The doubly substituted oxo-centered ruthenium clusters were synthesized using previously published procedures.[13,32-35,37-39] The ancillary ligands were added in excess (20 Eq.) and allowed to react over 24hrs. The product was separated by column chromatography using 99-1% chloroform to methanol. The product was dried and re-dissolved in CH_2Cl_2 and crashed out with hexanes. The product was then filtered, washed with hexanesm and dried over a fine porosity glass fritted filter. Usual yields ranged from 70 to 60%. Single crystals suitable for XRD studies were obtained by layering ether over frozen CH_2Cl_2.

$Ru_3O(CO)(PEP)_2$ ^{1}H NMR ($CDCl_3$, 500 MHz): δ (ppm)= 8.96 (d,4H); 8.07 (d,4H); 7.66 (d, 4H); 7.44 (d,4H); 2.11 (s,12H); 1.84 (s,6H) Single crystals suitable for XRD studies were obtained by layering of ether and frozen CH_2Cl_2.

$Ru_3O(CO)(MeO\text{-}PEP)_2$ ^{1}H NMR ($CDCl_3$, 500 MHz): δ (ppm)= 8.98 (d,4H); 8.05 (d,4H); 7.60 (d, 4H); 6.97 (d,4H); 3.88 (s,6H); 2.11 (s,12H); 1.84 (s,6H)

$Ru_3O(CO)(DMAP\text{-}PEP)_2$ ^{1}H NMR ($CDCl_3$, 500 MHz): δ (ppm)= 8.94 (d,4H); 7.95 (d,4H); 7.74 (d, 4H); 7.02 (d,4H); 3.01 (s,12H); 2.13 (s,12H); 1.88 (s,6H)

The triply substituted ruthenium clusters were synthesized following the procedure published by Baumann et al.[18-20] Briefly, 150mg of $[Ru_3O(OAc)_6(MeOH)_3]^+$ was diluted in 50mL of methanol. The chosen ancillary ligand (270mg) was then added to the solution. The mixture was heated to reflux for 10 minutes. The solution turned from green to yellow/green. After the reflux was completed, the solution was cooled in an ice bath to 0C. Upon cooling hydrazine monohydrate was added dropwise. The brown mixture was then stirred for an additional 15 minutes to allow for the reduction to go to completion. After 15 minutes 3 additional drops of hydrazine monohydrate were added to ensure completion of the reaction. The solid that crashed out of solution was filtered on a medium porosity fritted glass filter and washed extensively with deionized water, methanol, and diethyl ether. The solid was then dried under vacuum for 12hrs. and stored away from light.

$Ru_3O(PEP)_3$ ^{1}H NMR ($CDCl_3$, 500 MHz): δ (ppm)= 8.73 (d,6H); 8.10 (d,6H); 7.65 (d, 6H); 7.41 (d,6H); 2.26 (s,18H)

$Ru_3O(MeO\text{-}PEP)_3$ ^{1}H NMR ($CDCl_3$, 500 MHz): δ (ppm)= 9.05 (d,6H); 7.69 (d,6H); 7.58 (d,6H); 6.94 (d,6H); 3.87 (s,9H); 2.16 (s,18H).

Spectroscopy

IR spectra were collected on a Bruker Equinox 55 FTIR spectrometer. IR-SEC was performed with a custom built reflectance cell mounted on a specular reflectance unit.[55] UV/vis data were collected on a Shimadzu UV-3600 UV/vis/NIR

spectrophotometer. Samples were enclosed in a Specac sealed liquid IR cell with CaF_2 windows with 0.5 mm path length. Curve fitting of spectra to multiple Gaussian peaks was performed in Origin 6.0. Chemical reductions were performed using decamethylcobaltocene as the reducing agent

Electrochemical Measurements.

Electrochemistry was performed with a BAS Epsilon potentiostat in dried deoxygenated CH_2Cl_2 with 0.1 M tetrabutylammonium hexafluorophosphate (TBAH, recrystallized from MeOH and dried under vacuum at 80 °C) and 0.3-5 mM sample concentrations at a scan rate of 100 mV/s under N_2 atmosphere. The working electrode was a platinum disk (1.6mm diameter), the counter electrode a platinum wire, and the reference a Ag/AgCl wire.

X-Ray Diffraction Studies.

The single crystal X-ray diffraction studies were carried out on a Bruker Kappa APEX-II CCD diffractometer equipped with Mo Kα radiation (λ = 0.710 73 Å) or a Bruker Kappa APEX CCD diffractometer equipped with Cu Kα radiation (λ = 1.54184 Å). The crystals were mounted on a Cryoloop with Paratone oil, and data were collected under a nitrogen gas stream at 100(2) K using ω and φ scans. Data were integrated using the Bruker SAINT software program and scaled using the software program. Solution by direct methods (SHELXS) produced a complete phasing model consistent with the proposed structure. All non hydrogen atoms were refined anisotropically by full-matrix least squares (SHELXL-97).[56] All hydrogen

atoms were placed using a riding model. Their positions were constrained relative to their parent atom using the appropriate HFIX command in SHELXL-97.

Note: Much of the material for this chapter comes directly from a manuscript in preparation entitled: "Spectroscopic and Electrochemical Studies of Ru_3O clusters with π-stacking ligands" by Gabriele Canzi, David Ung, and Clifford P. Kubiak. The dissertation author is the primary author of this manuscript.

6.7 Appendix

Table 6.3 Crystal data and structure refinement for PEP ligand

Identification code	SUPERBRIDGE
Empirical formula	$C_{13}H_9N$
Formula weight	179.21
Temperature/K	296.15
Crystal system	orthorhombic
Space group	$P2_12_12_1$
a/Å	5.7714(5)
b/Å	7.4143(7)
c/Å	22.811(2)
α/°	90.00
β/°	90.00
γ/°	90.00
Volume/$Å^3$	976.12(15)
Z	4
$\rho_{calc}mg/mm^3$	1.219
m/mm^{-1}	0.072
F(000)	376.0
Crystal size/mm^3	0.1 × 0.1 × 0.04
Radiation	MoKα (λ = 0.71073)
2Θ range for data collection	3.58 to 58.62°

Table 6.3 Crystal data and structure refinement for PEP ligand continued

Index ranges	$-7 \leq h \leq 7, -9 \leq k \leq 9, -19 \leq l \leq 31$
Reflections collected	5266
Independent reflections	2280 [R_{int} = 0.0188, R_{sigma} = 0.0248]
Data/restraints/parameters	2280/0/163
Goodness-of-fit on F^2	1.047
Final R indexes [I>=2σ (I)]	R_1 = 0.0353, wR_2 = 0.0830
Final R indexes [all data]	R_1 = 0.0437, wR_2 = 0.0883
Largest diff. peak/hole / e $Å^{-3}$	0.21/-0.17
Flack parameter	-1(3)

Table 6.4 Bond lengths and bond lengths for PEP ligand

C13	C12	1.3851(18)	C1	N1	1.3422(19)
C13	C8	1.4013(19)	C2	C3	1.3977(18)
C12	C11	1.394(2)	C4	C3	1.399(2)
C8	C9	1.401(2)	C3	C6	1.4346(18)
C8	C7	1.4370(18)	C9	C10	1.3891(19)
C5	C4	1.3867(19)	C10	C11	1.385(2)
C5	N1	1.3419(17)	C6	C7	1.1979(18)
C1	C2	1.3838(19)			

C12	C13	C8	120.08(13)	C2	C3	C4	117.70(12)
C13	C12	C11	120.04(13)	C2	C3	C6	120.92(12)
C13	C8	C7	119.53(12)	C4	C3	C6	121.36(12)
C9	C8	C13	119.57(12)	C10	C9	C8	119.80(13)
C9	C8	C7	120.89(12)	C11	C10	C9	120.34(13)
N1	C5	C4	123.97(13)	C7	C6	C3	177.32(14)
N1	C1	C2	123.83(13)	C6	C7	C8	177.43(14)
C1	C2	C3	119.04(13)	C5	N1	C1	116.70(12)
C5	C4	C3	118.74(12)	C10	C11	C12	120.16(12)

Table 6.5 Crystal data and structure refinement for Me-PEP ligand.

Identification code	P212121_a
Empirical formula	$C_{20}H_{20}N_2O_2$
Formula weight	320.38
Temperature/K	273.15
Crystal system	orthorhombic
Space group	$P2_12_12_1$
a/Å	6.0111(12)
b/Å	7.5221(12)
c/Å	23.049(5)
α/°	90.00
β/°	90.00
γ/°	90.00
Volume/Å^3	1042.2(3)
Z	2
ρ_{calc}mg/mm^3	1.021
m/mm^{-1}	0.067
F(000)	340.0
Crystal size/mm^3	? × ? × ?
Radiation	MoKα (λ = 0.71073)
2Θ range for data collection	5.7 to 52.74°
Index ranges	$-7 \leq h \leq 7$, $-9 \leq k \leq 8$, $-20 \leq l \leq 28$
Reflections collected	6663
Independent reflections	2131 [R_{int} = 0.0334, R_{sigma} = 0.0443]
Data/restraints/parameters	2131/36/137
Goodness-of-fit on F^2	1.055
Final R indexes [I>=2σ (I)]	R_1 = 0.0395, wR_2 = 0.0913
Final R indexes [all data]	R_1 = 0.0540, wR_2 = 0.0963
Largest diff. peak/hole / e Å^{-3}	0.18/-0.20
Flack parameter	0(4)

Table 6.6 Bond lengths for Me-PEP ligand.

Atom	Atom	Length/Å	Atom	Atom	Length/Å
N1	C5	1.337(2)	C8	C9	1.398(2)
N1	C1	1.341(2)	C7	C6	1.202(2)
C13	C12	1.377(2)	C3	C2	1.390(2)
C13	C8	1.400(2)	C3	C6	1.433(2)
C4	C5	1.377(2)	C11	C10	1.390(2)
C4	C3	1.393(2)	C11	C14	1.503(2)
C12	C11	1.393(2)	C9	C10	1.383(2)
C8	C7	1.430(2)	C2	C1	1.374(2)

Table 6.7 Bond angles for Me-PEP ligand.

Atom	Atom	Atom	Angle/°	Atom	Atom	Atom	Angle/°
C5	N1	C1	115.93(14)	C2	C3	C4	117.34(14)
C12	C13	C8	120.66(15)	C2	C3	C6	120.87(15)
C5	C4	C3	118.68(15)	C12	C11	C14	120.43(14)
C13	C12	C11	120.92(15)	C10	C11	C12	118.20(15)
N1	C5	C4	124.63(16)	C10	C11	C14	121.37(14)
C13	C8	C7	120.69(14)	C10	C9	C8	119.67(15)
C9	C8	C13	118.80(14)	C1	C2	C3	119.49(15)
C9	C8	C7	120.50(14)	C9	C10	C11	121.75(15)
C6	C7	C8	179.63(18)	C7	C6	C3	176.51(17)
C4	C3	C6	121.75(14)	N1	C1	C2	123.90(15)

Table 6.8. Crystal data and structure refinement for MeO-PEP ligand.

Identification code	MeOPEP2_Cc
Empirical formula	$C_{14}H_{11}NO$
Formula weight	209.25
Temperature/K	296.15
Crystal system	monoclinic
Space group	Cc
a/Å	25.4469(15)
b/Å	7.2419(4)
c/Å	6.0684(3)
α/°	90
β/°	93.301(3)
γ/°	90
Volume/Å^3	1116.45(11)
Z	4
ρ_{calc}mg/mm^3	1.2448
m/mm^{-1}	0.079
F(000)	440.2
Crystal size/mm^3	0.3 × 0.2 × 0.2
Radiation	Mo Kα (λ = 0.71073)
2Θ range for data collection	3.2 to 56.98°
Index ranges	$-30 \leq h \leq 33$, $-9 \leq k \leq 9$, $-8 \leq l \leq 4$
Reflections collected	6209
Independent reflections	1841 [R_{int} = 0.0322, R_{sigma} = 0.0346]
Data/restraints/parameters	1841/0/145
Goodness-of-fit on F^2	1.222
Final R indexes [I>=2σ (I)]	R_1 = 0.0553, wR_2 = 0.1445
Final R indexes [all data]	R_1 = 0.0745, wR_2 = 0.1773
Largest diff. peak/hole / e Å^{-3}	0.51/-0.34
Flack parameter	-1.5(10)

Table 6.9. Bond lengths for MeO-PEP ligand

Atom	Atom	Length/Å	Atom	Atom	Length/Å
C6	C7	1.202(4)	C4	C3	1.404(5)
C6	C3	1.433(5)	C12	C11	1.389(5)
C2	C1	1.382(5)	C12	C13	1.386(5)
C2	C3	1.389(5)	C10	C11	1.396(5)
O1	C11	1.386(4)	C10	C9	1.387(5)
O1	C14	1.434(4)	C8	C7	1.432(5)
N1	C1	1.347(5)	C8	C9	1.407(5)
N1	C5	1.338(5)	C8	C13	1.406(5)
C4	C5	1.376(5)			

Table 6.10. Bond angles for MeO-PEP ligand**.**

Atom	Atom	Atom	Angle/°	Atom	Atom	Atom	Angle/°
C3	C6	C7	177.5(3)	C8	C7	C6	176.7(3)
C3	C2	C1	119.0(3)	C4	C5	N1	124.9(3)
C14	O1	C11	118.1(3)	C12	C11	O1	125.1(3)
C5	N1	C1	116.1(4)	C10	C11	O1	114.4(3)
C3	C4	C5	118.1(3)	C10	C11	C12	120.5(3)
C13	C12	C11	119.7(3)	C2	C3	C6	121.5(3)
C9	C10	C11	119.5(3)	C4	C3	C6	120.4(3)
C9	C8	C7	120.3(3)	C4	C3	C2	118.1(3)
C13	C8	C7	121.8(3)	C8	C9	C10	121.2(3)
C13	C8	C9	117.8(3)	C8	C13	C12	121.3(3)
N1	C1	C2	123.8(4)				

Table 6.11 Crystal data and structure refinement for $Ru_3O(PEP)_2$.

Identification code	KUBVG01B5R
Empirical formula	$C_{39}H_{36}O_{14}Ru_3N_2$
Formula weight	1059.91
Temperature/K	100.15
Crystal system	monoclinic
Space group	$P2_1/c$
a/Å	27.751(12)
b/Å	8.048(3)
c/Å	19.865(8)
α/°	90.00
β/°	91.694(5)
γ/°	90.00
Volume/Å^3	4435(3)
Z	4
ρ_{calc}mg/mm^3	1.587
m/mm^{-1}	1.072
F(000)	2112.0
Crystal size/mm^3	0.2 × 0.15 × 0.1
Radiation	MoKα (λ = 0.71073)
2Θ range for data collection	4.4 to 51.62°
Index ranges	$-33 \leq h \leq 33$, $0 \leq k \leq 9$, $0 \leq l \leq 24$
Reflections collected	8108
Independent reflections	8118 [R_{int} = 0.0000, R_{sigma} = 0.1251]
Data/restraints/parameters	8118/0/524
Goodness-of-fit on F^2	1.147
Final R indexes [I>=2σ (I)]	R_1 = 0.0808, wR_2 = 0.1764
Final R indexes [all data]	R_1 = 0.1204, wR_2 = 0.1944
Largest diff. peak/hole / e Å^{-3}	1.31/-1.56

Table 6.12 Bond lengths for $Ru_3O(PEP)_2$.

Atom	Atom	Length/Å	Atom	Atom	Length/Å
Ru1	O1	2.051(7)	N2	C31	1.377(12)
Ru1	O3	2.047(7)	C1	C2	1.520(14)
Ru1	O10	2.040(7)	C3	C4	1.522(14)
Ru1	O12	2.053(7)	C5	C6	1.504(13)
Ru1	O13	1.901(6)	C7	C8	1.550(13)
Ru1	N1	2.116(8)	C9	C10	1.530(14)
Ru2	O2	2.043(6)	C11	C12	1.531(14)
Ru2	O4	2.074(6)	C14	C15	1.389(15)
Ru2	O5	2.070(6)	C15	C16	1.395(18)
Ru2	O7	2.046(7)	C16	C17	1.435(19)
Ru2	O13	1.913(6)	C16	C19	1.444(15)
Ru2	N2	2.129(8)	C17	C18	1.392(15)
Ru3	O6	2.080(7)	C19	C20	1.205(16)
Ru3	O8	2.072(7)	C20	C21	1.453(16)
Ru3	O9	2.095(7)	C21	C22	1.419(17)
Ru3	O11	2.089(7)	C21	C26	1.435(17)
Ru3	O13	2.035(6)	C22	C23	1.390(16)
Ru3	C13	1.829(11)	C23	C24	1.395(17)
O1	C1	1.283(12)	C24	C25	1.424(17)
O2	C1	1.277(11)	C25	C26	1.401(16)
O3	C3	1.283(12)	C27	C28	1.403(13)
O4	C3	1.277(12)	C28	C29	1.417(13)
O5	C5	1.256(11)	C29	C30	1.399(13)
O6	C5	1.265(11)	C29	C32	1.443(13)
O7	C7	1.272(11)	C30	C31	1.389(13)
O8	C7	1.250(11)	C32	C33	1.198(13)
O9	C9	1.269(11)	C33	C34	1.454(13)
O10	C9	1.271(11)	C34	C35	1.417(13)
O11	C11	1.252(12)	C34	C39	1.408(14)
O12	C11	1.271(12)	C35	C36	1.382(14)
O14	C13	1.158(12)	C36	C37	1.422(15)

Table 6.13 Bond angles for $Ru_3O(PEP)_2$.

Atom	Atom	Atom	Angle/°	Atom	Atom	Atom	Angle/°
O1	Ru1	O12	167.6(3)	C14	N1	Ru1	121.1(7)
O1	Ru1	N1	84.2(3)	C18	N1	Ru1	119.9(8)
O3	Ru1	O1	93.6(3)	C18	N1	C14	119.0(9)
O3	Ru1	O12	84.3(3)	C27	N2	Ru2	122.4(6)
O3	Ru1	N1	86.7(3)	C27	N2	C31	118.0(8)
O10	Ru1	O1	86.8(3)	C31	N2	Ru2	119.6(6)
O10	Ru1	O3	171.6(3)	O1	C1	O2	126.4(9)
O10	Ru1	O12	93.5(3)	O1	C1	C2	116.2(9)
O10	Ru1	N1	85.0(3)	O2	C1	C2	117.3(9)
O12	Ru1	N1	83.6(3)	O3	C3	O4	126.0(9)
O13	Ru1	O1	96.3(3)	O3	C3	C4	117.0(9)
O13	Ru1	O3	93.8(3)	O4	C3	C4	116.9(9)
O13	Ru1	O10	94.5(3)	O5	C5	O6	125.3(8)
O13	Ru1	O12	96.0(3)	O5	C5	C6	117.8(8)
O13	Ru1	N1	179.3(3)	O6	C5	C6	116.9(8)
O2	Ru2	O4	90.8(3)	O7	C7	C8	114.5(8)
O2	Ru2	O5	88.3(3)	O8	C7	O7	128.2(8)
O2	Ru2	O7	171.8(3)	O8	C7	C8	117.3(8)
O2	Ru2	N2	85.6(3)	O9	C9	O10	128.0(9)
O4	Ru2	N2	84.7(3)	O9	C9	C10	115.6(9)
O5	Ru2	O4	168.7(3)	O10	C9	C10	116.3(8)
O5	Ru2	N2	84.0(3)	O11	C11	O12	127.9(10)
O7	Ru2	O4	87.9(3)	O11	C11	C12	117.1(9)
O7	Ru2	O5	91.4(3)	O12	C11	C12	115.0(9)
O7	Ru2	N2	86.2(3)	O14	C13	Ru3	172.9(9)
O13	Ru2	O2	95.0(3)	N1	C14	C15	121.8(11)
O13	Ru2	O4	96.3(3)	C16	C15	C14	118.8(12)
O13	Ru2	O5	95.0(3)	C15	C16	C17	120.0(11)
O13	Ru2	O7	93.1(3)	C15	C16	C19	122.2(13)
O13	Ru2	N2	178.8(3)	C17	C16	C19	117.8(13)
O6	Ru3	O9	86.6(3)	C18	C17	C16	117.5(12)

Table 6.13 Bond angles for $Ru_3O(PEP)_2$ continued.

O6	Ru3	O11	177.6(3)	N1	C18	C17	122.9(12)
O8	Ru3	O6	93.1(3)	C20	C19	C16	174.1(17)
O8	Ru3	O9	173.4(3)	C19	C20	C21	176.3(17)
O8	Ru3	O11	88.9(3)	C22	C21	C20	119.0(11)
O11	Ru3	O9	91.2(3)	C22	C21	C26	121.1(10)
O13	Ru3	O6	89.5(3)	C26	C21	C20	119.9(11)
O13	Ru3	O8	92.5(3)	C23	C22	C21	118.6(12)
O13	Ru3	O9	94.0(3)	C24	C23	C22	121.5(12)
O13	Ru3	O11	91.7(3)	C23	C24	C25	120.2(10)
C13	Ru3	O6	88.1(4)	C24	C25	C26	120.0(11)
C13	Ru3	O8	83.7(4)	C25	C26	C21	118.6(11)
C13	Ru3	O9	89.7(4)	N2	C27	C28	123.2(9)
C13	Ru3	O11	90.9(4)	C27	C28	C29	117.9(9)
C13	Ru3	O13	175.4(4)	C28	C29	C32	119.8(9)
C1	O1	Ru1	132.4(6)	C30	C29	C28	119.5(8)
C1	O2	Ru2	127.1(6)	C30	C29	C32	120.6(8)
C3	O3	Ru1	127.7(6)	C29	C30	C31	118.1(8)
C3	O4	Ru2	130.3(6)	N2	C31	C30	123.1(8)
C5	O5	Ru2	133.0(6)	C33	C32	C29	177.8(10)
C5	O6	Ru3	129.6(6)	C32	C33	C34	178.1(10)
C7	O7	Ru2	127.4(6)	C35	C34	C33	118.7(9)
C7	O8	Ru3	133.7(6)	C35	C34	C39	120.7(9)
C9	O9	Ru3	131.7(7)	C39	C34	C33	120.5(9)
C9	O10	Ru1	128.5(6)	C36	C35	C34	120.3(10)
C11	O11	Ru3	128.9(7)	C35	C36	C37	119.8(10)
C11	O12	Ru1	132.6(6)	C38	C37	C36	119.5(10)
Ru1	O13	Ru2	119.8(3)	C37	C38	C39	122.0(10)
Ru1	O13	Ru3	119.6(3)	C38	C39	C34	117.7(9)
Ru2	O13	Ru3	120.6(3)				

6.8 References

(1) McGaughey, G. B.; Gagné, M.; Rappé, A. K. *Journal of Biological Chemistry* **1998**, *273*, 15458.

(2) Coropceanu, V.; Cornil, J.; da Silva Filho, D. A.; Olivier, Y.; Silbey, R.; Brédas, J.-L. *Chemical Reviews* **2007**, *107*, 926.

(3) Geng, W. T.; Oda, M.; Nara, J.; Kondo, H.; Ohno, T. *The Journal of Physical Chemistry B* **2008**, *112*, 2795.

(4) Kang, Y. K.; Iovine, P. M.; Therien, M. J. *Coordination Chemistry Reviews* **2011**, *255*, 804.

(5) Solomon, G. C.; Herrmann, C.; Vura-Weis, J.; Wasielewski, M. R.; Ratner, M. A. *Journal of the American Chemical Society* **2010**, *132*, 7887.

(6) Boehr, D. D.; Farley, A. R.; Wright, G. D.; Cox, J. R. *Chemistry & Biology* **2002**, *9*, 1209.

(7) Ohndorf, U.-M.; Rould, M. A.; He, Q.; Pabo, C. O.; Lippard, S. J. *Nature* **1999**, *399*, 708.

(8) Solomon, G. C.; Vura-Weis, J.; Herrmann, C.; Wasielewski, M. R.; Ratner, M. A. *The Journal of Physical Chemistry B* **2010**, *114*, 14735.

(9) Vura-Weis, J.; Ratner, M. A.; Wasielewski, M. R. *Journal of the American Chemical Society* **2010**, *132*, 1738.

(10) Brédas, J.-L.; Beljonne, D.; Coropceanu, V.; Cornil, J. *Chemical Reviews* **2004**, *104*, 4971.

(11) Delgado, M. C. R.; Kim, E.-G.; Filho, D. A. d. S.; Bredas, J.-L. *Journal of the American Chemical Society* **2010**, *132*, 3375.

(12) Canzi, G.; Goeltz, J. C.; Henderson, J. S.; Park, R. E.; Maruggi, C.; Kubiak, C. P. *Journal of the American Chemical Society* **2014**, *136*, 1710.

(13) Goeltz, J. C.; Kubiak, C. P. *J. Am. Chem. Soc.* **2010**, *132*, 17390.

(14) Spencer, A.; Wilkinson, G. *Journal of the Chemical Society, Dalton Transactions* **1972**, 1570.

(15) Spencer, A.; Wilkinson, G. *Journal of the Chemical Society, Dalton Transactions* **1974**, 786.

(16) Abe, M.; Sasaki, Y.; Yamada, Y.; Tsukahara, K.; Yano, S.; Ito, T. *Inorganic Chemistry* **1995**, *34*, 4490.

(17) Abe, M.; Sasaki, Y.; Yamada, Y.; Tsukahara, K.; Yano, S.; Yamaguchi, T.; Tominaga, M.; Taniguchi, I.; Ito, T. *Inorg. Chem.* **1996**, *35*, 6724.

(18) Baumann, J. A.; Salmon, D. J.; Wilson, S. T.; Meyer, T. J. *Inorganic Chemistry* **1979**, *18*, 2472.

(19) Baumann, J. A.; Salmon, D. J.; Wilson, S. T.; Meyer, T. J.; Hatfield, W. E. *Inorganic Chemistry* **1978**, *17*, 3342.

(20) Baumann, J. A.; Wilson, S. T.; Salmon, D. J.; Hood, P. L.; Meyer, T. J. *Journal of the American Chemical Society* **1979**, *101*, 2916.

(21) Ito, T.; Hamaguchi, T.; Nagino, H.; Yamaguchi, T.; Washington, J.; Kubiak, C. P. *Science (USA)* **1997**, *277*, 660.

(22) Kubiak, C. P. *Inorganic Chemistry* **2013**.

(23) Elangovan, A.; Wang, Y.-H.; Ho, T.-I. *Organic Letters* **2003**, *5*, 1841.

(24) Sonogashira, K.; Tohda, Y.; Hagihara, N. *Tetrahedron Letters* **1975**, *16*, 4467.

(25) Takahashi, S.; Kuroyama, Y.; Sonogashira, K.; Hagihara, N. *Synthesis* **1980**, *1980*, 627.

(26) Sonogashira, K. *Journal of Organometallic Chemistry* **2002**, *653*, 46.

(27) Chinchilla, R.; Nájera, C. *Chemical Reviews* **2007**, *107*, 874.

(28) Glover, S. D.; Goeltz, J. C.; Lear, B. J.; Kubiak, C. P. *Eur. J. Inorg. Chem.* **2009**, 585.

(29) Glover, S. D.; Goeltz, J. C.; Lear, B. J.; Kubiak, C. P. *Coord. Chem. Rev.* **2010**, *254*, 331.

(30) Glover, S. D.; Kubiak, C. P. *J. Am. Chem. Soc.* **2011**, *133*, 8721.

(31) Glover, S. D.; Lear, B. J.; Salsman, C.; Londergan, C. H.; Kubiak, C. P. *Phil.Trans. Roy. Soc. A.* **2008**, *366*, 177.

(32) Goeltz, J. C.; Benson, E. E.; Kubiak, C. P. *Journal of Physical Chemistry B* **2010**, *114*, 14729.

(33) Goeltz, J. C.; Glover, S. D.; Hauk, J.; Kubiak, C. P.; Putman, R. D.; Rauchfuss, T. B. In *Inorg. Synth.* 2010; Vol. 35, p 156.

(34) Goeltz, J. C.; Hanson, C. J.; Kubiak, C. P. *Inorganic Chemistry* **2009**, *48*, 4763.

(35) Goeltz, J. C.; Kubiak, C. P. *J. Phys. Chem. C* **2008**, *112*, 8114.

(36) Lear, B. J.; Glover, S. D.; Salsman, J. C.; Londergan, C. H.; Kubiak, C. P. *J. Am. Chem. Soc.* **2007**, *129*, 12772.

(37) Salsman, J. C.; Kubiak, C. P. In *Spectroelectrochemisty*; Kaim, W., Klein, A., Eds.; Royal Society of Chemistry: Cambridge, 2008, p 123.

(38) Salsman, J. C.; Kubiak, C. P.; Ito, T. *J. Am. Chem. Soc.* **2005**, *127*, 2382.

(39) Salsman, J. C.; Ronco, S.; Londergan, C. H.; Kubiak, C. P. *Inorganic Chemistry* **2006**, *45*, 547.

(40) Canzi, G.; Kubiak, C. P. *Small* **2011**, *7*, 1967.

(41) Canzi, G.; Kubiak, C. P. *The Journal of Physical Chemistry C* **2012**, *116*, 6560.

(42) Morris-Cohen, A. J.; Aruda, K. O.; Rasmussen, A. M.; Canzi, G.; Seideman, T.; Kubiak, C. P.; Weiss, E. A. *Physical Chemistry Chemical Physics* **2012**, *14*, 13794.

(43) Astruc, D. *Electron Transfer and Radical Processes in Transition-Metal Chemistry*; Wiley-VCH: New York, 1995.

(44) Sutton, J. E.; Taube, H. *Inorg. Chem.* **1981**, *20*, 3126.

(45) Sutton, J. E.; Sutton, P. M.; Taube, H. *Inorganic Chemistry* **1979**, *18*, 1017.

(46) Londergan, C. H.; Salsman, J. C.; Lear, B. J.; Kubiak, C. P. *Chemical Physics* **2006**, *324*, 57.

(47) Hunter, C. A.; Sanders, J. K. M. *Journal of the American Chemical Society* **1990**, *112*, 5525.

(48) Sutin, N. J. *Prog. Inorg. Chem.* **1983**, *30*, 441.

(49) Hush, N. S. *Transactions of the Faraday Society* **1961**, *57*, 557.

(50) Hush, N. S. *Prog. Inorg. Chem.* **1967**, *8*, 391.

(51) Marcus, R. A. *The Journal of Chemical Physics* **1956**, *24*, 966.

(52) Marcus, R. A. *Annu. Rev. Phys. Chem.* **1964**, *15*, 155.

(53) Marcus, R. A. *Angew. Chem. Int.- Ed.* **1993**, *32*, 1111.

(54) Robin, M. B.; Day, P. *Adv. Inorg. Chem. Radiochem.* **1967**, *10*, 247.

(55) Zavarine, I. S.; Kubiak, C. P. *J. Electroanal. Chem.* **2001**, *495*, 106.

(56) Sheldrick, G. *Acta Crystallographica Section A* **2008**, *64*, 112.

Chapter 7

Diffusion ordered NMR spectroscopy as a reliable alternative to TEM for determining the size of gold nanoparticles in organic solutions

7.1 Introduction

Sometimes while doing research you stumble upon a project that's unexpected yet fruitful and rewarding. This chapter describes exactly that, in fact, this is a project that started from a lecture during Cliff's Chem 262 Inorganic NMR class. Some might think that this chapter might not belong in this thesis or that it will stick out like a sore thumb, but I truly believe that it does belong and adds to the overall story of my graduate career. The newly developed analytical technique that will be described in this chapter served as an important characterization technique for all of the nanoparticle and nanocluster work. In addition, it proved extremely useful in determining diffusion coefficients for the

hydrogen bonded assemblies. As presented in previous chapters, we used this technique to show that upon reduction, a hydrogen-bonded dimer of Ru_3O clusters is formed in solution. So I would say that this technique has served us well and it ties in nicely with all the other work presented in the previous chapters.

While working on the nanocluster work that was highlighted in the early chapters of this thesis, I began looking at ways to characterize the gold nanoparticles that I was preparing in the laboratory. Although I was fortunate enough to use the top-notch TEM facilities here at UCSD I spent 80 hours on just training in order to use Sphera, the simplest TEM in the department. Looking at the time and cost of all of this I started to inform myself about alternative techniques used to characterize the nanoparticles I had just made. One quick literature search showed that other than dynamic light scattering (DLS) there were very few alternatives to TEM. Then on a Tuesday night while sitting in Chem 262 the alternative that I was looking for came to me. In the second half of the lecture series in the Inorganic NMR course, it is customary to examine case studies where real life examples are utilized to show the common uses of the techniques studied in the first half of the course. I remember that night as if it were yesterday, we were looking at a Paul S. Pregosin, who is most famous for his work on NMR spectroscopic studies of transition metal complezes, *Chem. Rev.* article where diffusion ordered NMR spectroscopy (DOSY) was used to determine sizes of metal complexes in solution by using the Stokes-Einstein equation and extracting an hydrodynamic radius from the diffusion coefficient observed in the 2D NMR

spectrum.[1] The connection was instant, why not use this very simple and inexpensive technique to calculate Au nanoparticle sizes from ^{1}H signals of functional groups on the nanoparticle surface? That's exactly what I set out to attempt and the results are highlighted in this chapter.

Gold nanoparticles (NPs) have been studied extensively in recent years, and have become very useful in a wide range of chemical and engineering applications.[2-5] Nanoparticles synthesized using the Brust-Schiffrin method[6] range from 1-7 nm in size. Characterization and sizing of nanoparticles is principally done by transmission electron microscopy, TEM, and occasionally with electronic spectroscopy and scanning mobility particle sizer (SMPS) spectrometers. While essential to the nanoscience community since its development, TEM access can be limited to some researchers due to high costs and significant learning curves. Herein, we present a time and cost effective way to characterize alkanethiol protected Au nanoparticles via 2D diffusion-based NMR. 2D NMR has been used to study nanomaterials in a multitude of ways recently, including ligand exchange kinetics of organics bound to NP surfaces, along with composition and purification of nanomaterials.[7-9] 2D diffusion-ordered NMR (DOSY) spectroscopy has previously been used as an effective tool in bridging imaging and species characterization.[1,10-14] The technique is especially powerful when dealing with mixtures containing large distributions of particle size, as is often the case in nanoparticle studies.[8] Using 2D DOSY NMR, size estimates of varying length alkanethiol protected nanoparticles were obtained using correlated

diffusion coefficients of nanoparticle capping thiols as referenced to an internal standard (ferrocene). The resulting size estimates correlate well with size distributions obtained via TEM. NMR is shown to yield nanoparticle size distributions in a way few other techniques can.[15,16] This is noteworthy as only very approximate size distributions can be made by observing plasmon resonance behavior of NPs in electronic spectroscopy.[17-19] A significant finding is that protecting thiols do not have a direct effect on the hydrodynamic radii of the nanoparticles in the solvents studied, and thus the measurements obtained from DOSY are in direct agreement with the visual measurements from TEM and are a true estimate of the metal core size. To the best of our knowledge this is the first method of direct measurements of nanoparticle sizes by studying the protecting ligands using 2D DOSY NMR, a method that could easily be expanded to other metal and seminconductor nanoparticles.

7.2 Results and discussion

Thiol capped gold nanoparticles prepared by the Brust method[6], C_{12}-Au and C_8-Au, were found by TEM to show significant size differences. Figure 7.1 shows C_{12}-Au NPs at 200,000x magnification, and C_8-Au NPs at 175,000x magnification. Both images show well defined metal cores, which aided with size determination by TEM. The sizes were controlled by the preparation conditions in order to show the effectiveness of the method. Nanoparticles capped with different thiols, but of the same Au core diameters were also examined to show that the thiols do not interfere with the metal core measurements. The size distributions of the two alkanethiol

capped nanoparticles are shown in Figure 7.2. The average size for a sample of C_{12}-Au was found to be 4.6 nm, and 2.7 nm for C_8-Au. These images serve as a point of reference to determine the accuracy of DOSY size estimates.

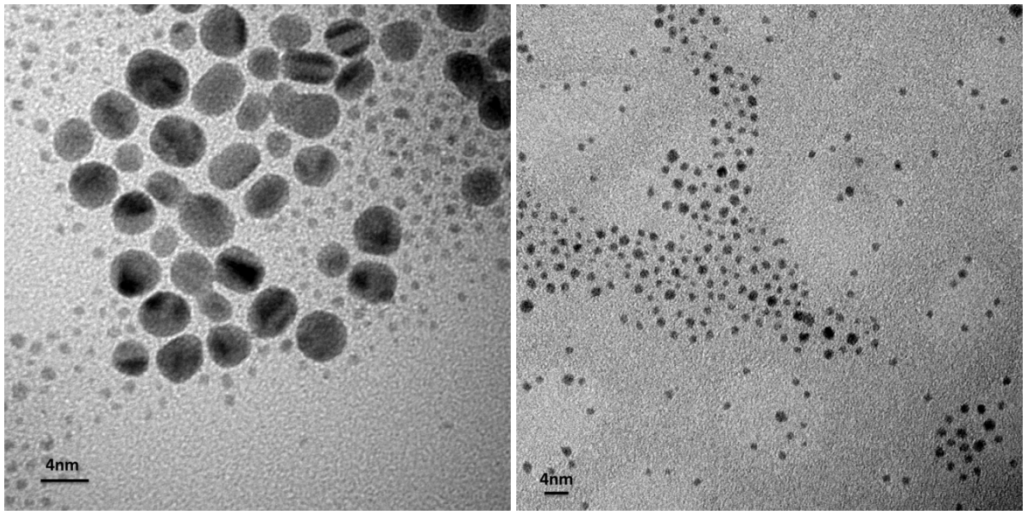

Figure 7.1. TEM image of 1-dodecathiol protected Au nanoparticles (Au-C_{12}) at 200kx (left) and TEM image of 1-octanethiol protected Au nanoparticles (Au-C_8) at 175kx. (right)

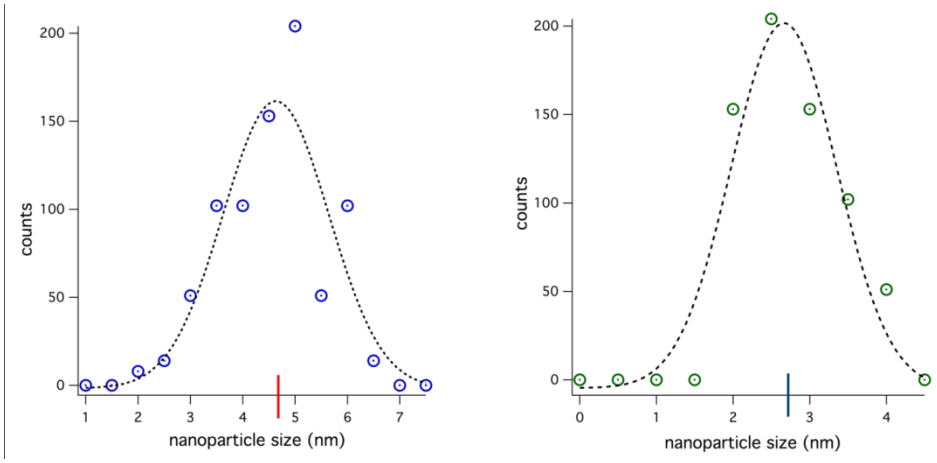

Figure 7.2. Au nanoparticle C_{12} (blue) and C_8 (green) size distributions and fit for a dilute sample in $CHCl_3$ taken from a TEM image on a copper 3x3 mm carbon coated grid. Average sizes of 4.63 nm and 2.66 nm are indicated on the x-axis in red (left) and blue (right) respectively.

For the DOSY measurements, ferrocene was chosen as the standard for several reasons: its well understood behavior in solution, the availability of reported diffusion coefficients under varied conditions[20], its symmetry-derived non-polarity, its distinct ^1H NMR resonance, and its known hydrodynamic radius. Another essential feature of ferrocene is that its NMR signal is located in an area of the ^1H NMR spectrum that is well isolated from any thiol and solvent resonances.

Au nanoparticles prepared by the Brust-Schiffrin method are soluble in non-polar solvents, therefore the three solvents used in this study were chloroform, benzene, and dichloromethane. Based on the polarity indices, we are confident that the method presented is general in varying degrees of solvent polarity. The polarity indices are 4.1, 3.1 and 2.7 for chloroform, dichloromethane, and benzene respectively.[20] The use of a non polar standard and solvents of no or low polarity

ensured that specific solvent-solute interactions would not interfere with the measurements. Variations in viscosity can be ignored since the experiments are performed in one solvent, only the observed diffusion coefficients will be impacted by varying solvents. The viscosity for benzene, chloroform, and dichloromethane are 0.602 x 10^{-3}, 0.54 x 10^{-3} and 1.6x 10^{-3} Pa·s, respectively.[20]

Diffusion is related to the size and shape of individual species by the well-known Debye-Einstein equation:

$$D = \frac{k_b T}{f_T} \quad (1)$$

where k_b is the Boltzmann constant, T is temperature reported in Kelvin, and f_T is the friction factor.

The Debye-Einstein equation can be further simplified assuming the diffusing species are spherical in shape.[21]

$$D = \frac{k_b T}{c\pi\eta r_H} \quad (2)$$

which is commonly known as the Stokes Einstein equation, where c is a parameter that approaches 6 as the hydrodynamic radius reaches 1nm[22], r_H is the hydrodynamic radius, and η is the viscosity of the solvent used. An estimate of molecular sizes can be obtained using the Stokes Einstein equation assuming that all the species are spherical, and methods exist for calculating non-spherical diffusion coefficients as well.[23,24]

The method proposed here further simplifies this relationship, by using the ratio of ferrocene's diffusion coefficient to that of the observed for the signals of the

thiols attached to the nanoparticles. Thus, from the known hydrodynamic radius of ferrocene, 0.3nm[20,25], the nanoparticles' hydrodynamic radius is calculated using Eq 3:

$$r_{H_{NP}} = \frac{D_{Fc}}{D_{NP}} \times r_{H_{Fc}} \quad (3)$$

where $r_{H_{NP}}$ is the hydrodynamic radius of the nanoparticles, $r_{H_{Fc}}$ is ferrocene's hydrodynamic radius, D_{Fc} is the diffusion coefficient of ferrocene, and D_{NP} is the diffusion coefficient of the Au nanoparticles. The measurement of *relative* diffusion coefficients allows the investigator to ignore the differences in viscosity between samples.

The 1D ^{1}H NMR spectra of 1-dodecanethiol capped and 1-octanethiol in deuterated chloroform are shown in Figures 7.3 and 7.5, respectively to show the unbound thiol resonances in solution. The 1D ^{1}H NMR spectra of 1-dodecanethiol capped Au nanoparticles and 1-octanethiol capped Au nanoparticles in deuterated chloroform are shown in Figures 7.4 and 7.6 respectively. The α,β, and γ signals are noticeably absent, as compared with Figure 7.3 and 7.5, serving as evidence that the thiols are bound to the NPs. Both samples contain ferrocene, where the single cyclopentadienyl ^{1}H resonance appears at 4.16 ppm in the spectra. Characteristic resonances for both methyl-terminated C_8 and C_{12} alkanethiols appear at 1.2 and 0.89 ppm. These resonances, along with the ferrocene resonance, were used to trace the diffusion of the Au nanopartices thorough solutions of deuterated chloroform, benzene and dichloromethane via DOSY NMR spectroscopy.

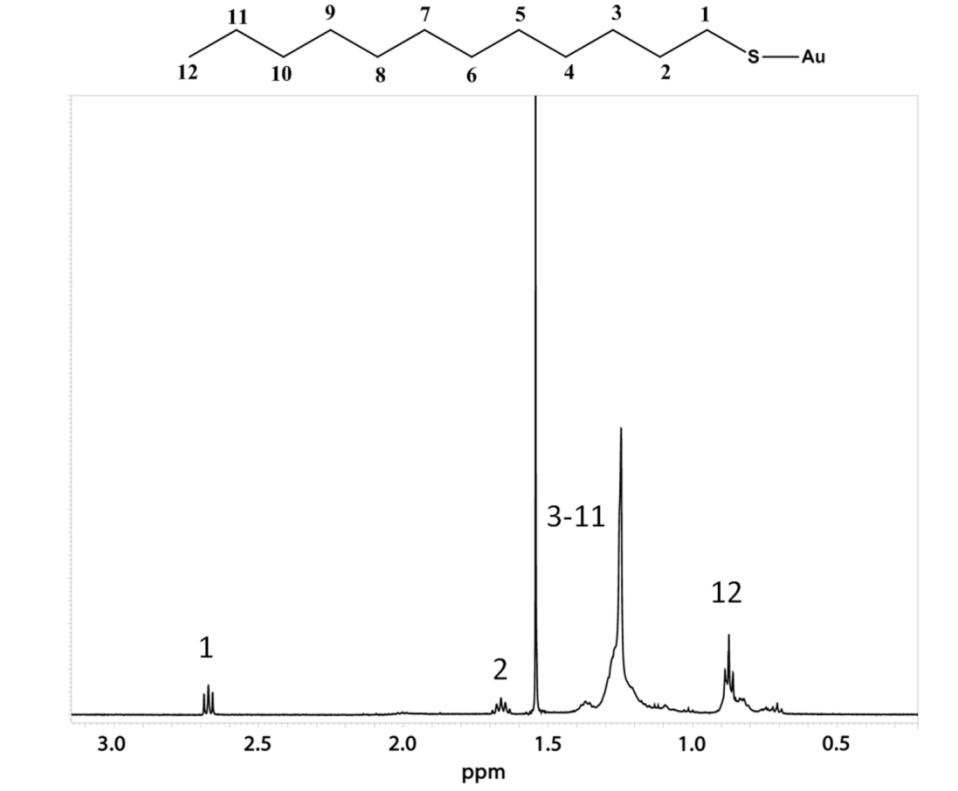

Figure 7.3. ^{1}H NMR spectrum of 1-dodecanethiol in chloroform. The ferrocene signal is omitted for clarity, but it is present at 4.16 ppm.

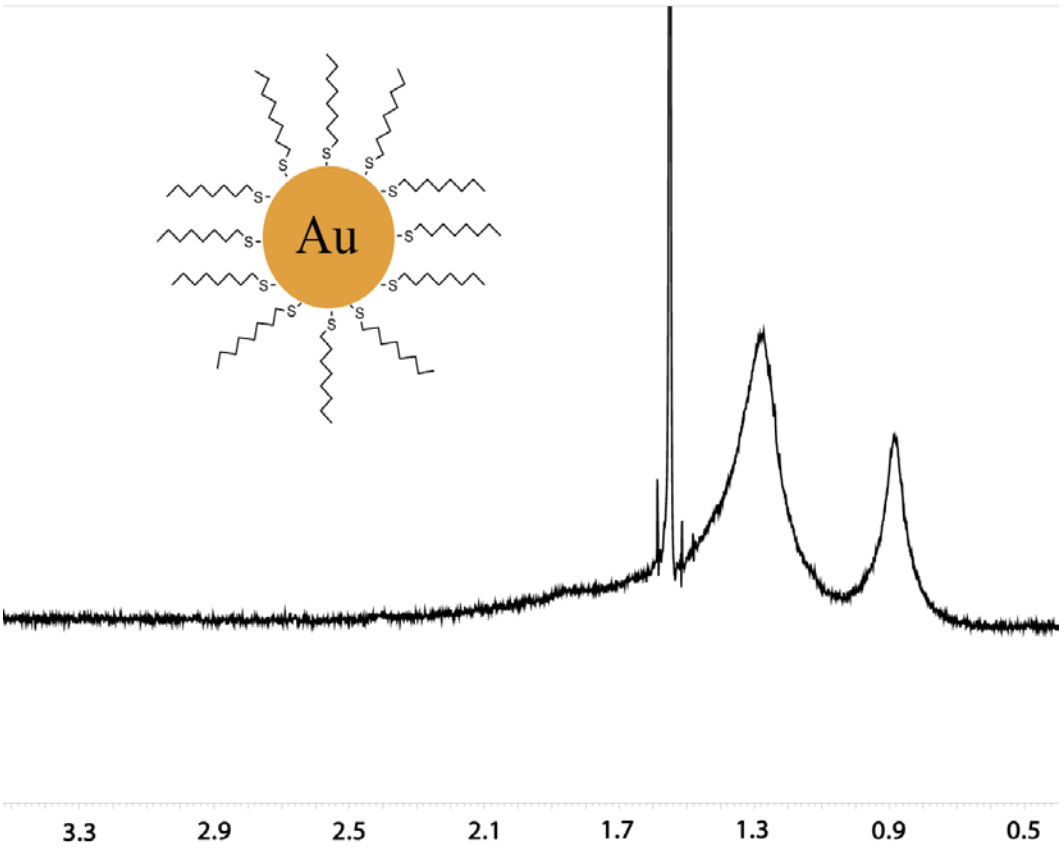

Figure 7.4. ^{1}H NMR spectrum of 1-dodecanethiol capped Au NPs. The large line broadening observed is evidence of surface attachment. The α,β, and γ signals are noticeably absent as expected for thiol signals on NPs.

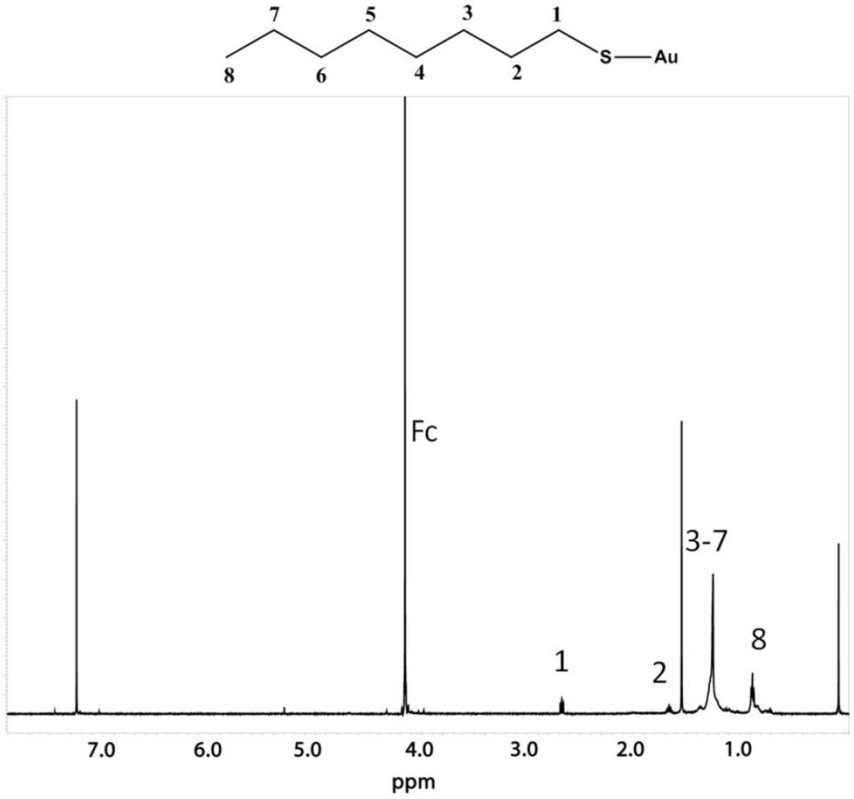

Figure 7.5. ^{1}H NMR spectrum of 1-octanethiol capped Au nanoparticles in chloroform. The ferrocene signal at 4.16ppm is denoted as Fc for clarity.

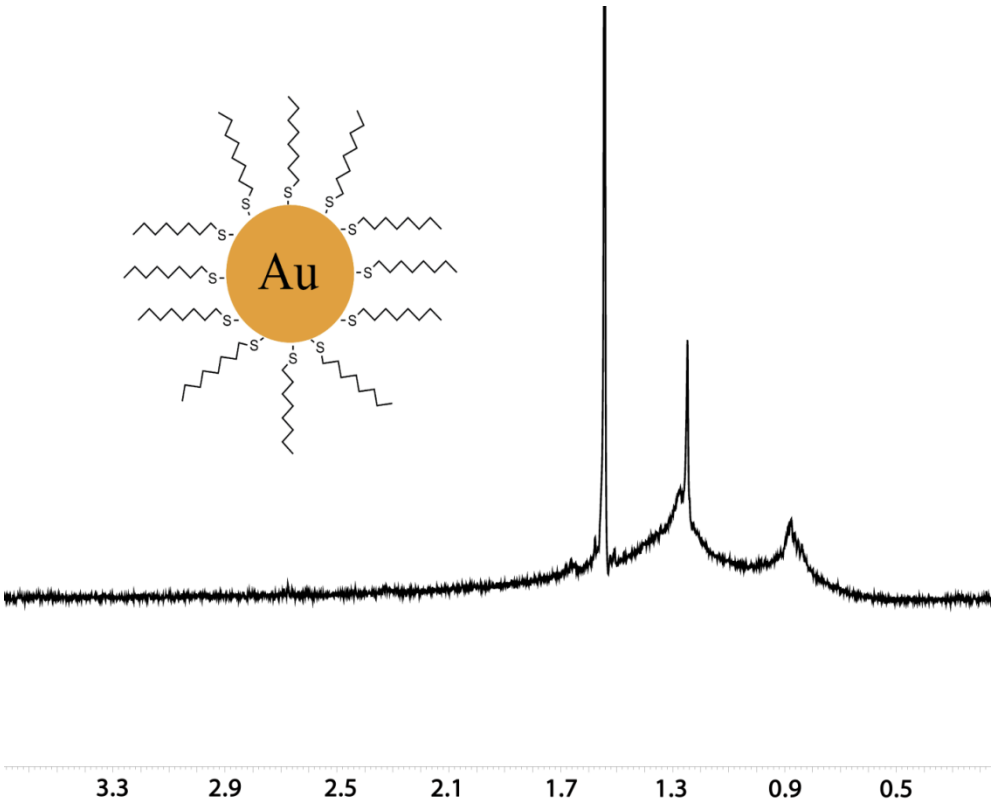

Figure 7.6. ^{1}H NMR spectrum of 1-octanethiol capped Au NPs. The large line broadening observed is evidence of surface attachment. The α,β, and γ signals are noticeably absent as expected for thiol signals on NPs.

All DOSY data were processed using the continuous method CONTIN[26] available in Delta, version 4.3.6. The CONTIN algorithm was chosen because of its ability to yield accurate diffusion coefficients without their prior knowledge for a large number of species as long as little overlap is present in their spectra.[27] The method is particularly useful for polydisperse samples. The synthesized nanoparticles have narrow size distributions yet they are still to be considered polydispersed.

A distinct difference in the diffusion coefficient between the larger and smaller nanoparticles is observed in Figures 7.7 and 7.8, suggesting a large disparity in overall particle size. Smaller 1-octanethiol protected particles diffuse faster, while the bigger 1-dodecanethiol protected particles diffuse slower. Figure 7.9 shows the DOSY NMR data of smaller, 2.3 nm Au nanoparticles synthesized using longer chain alkanethiol (C_{12}) protecting groups. The data show both good reproducibility for same-sized nanoparticles capped with different thiols and that the diffusion constant of the nanoparticles is unchanged by a variation in the thiol's chain length. This is consistent with the fact that thiol coverage on nanoparticles is typically less rigid than on a self assembled monolayer (SAM), and solvent can readily penetrate the relatively open thiol shell, due to the curvature of the NPs. This is also consistent with the experimental observation that thiolate substitution on nanoparticles is easier to achieve than thiolate substitution on a SAM. Figures 7.10 and 7.11 show data slices of the 2D DOSY data shown in Figures 7.7, 7.8, and 7.9. To determine the diffusion constants, the data were fit to Gaussian line-shapes using Origin[23] from which the error associated with each of the fits was obtained. The data fits are shown as dashed lines in the figures and the results are presented in Table 7.1.

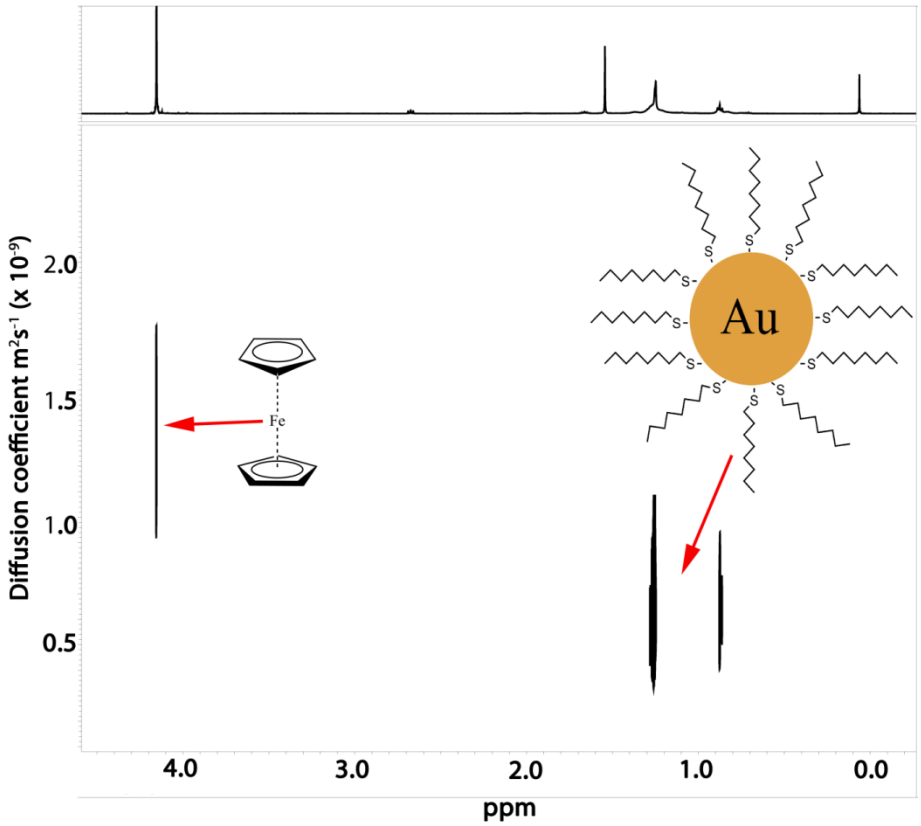

Figure 7.7. 2D DOSY NMR spectrum of C_8-Au nanoparticles in chloroform. The ferrocene signal at 4.16 ppm is clearly labeled. Each of run was 32768 and 32 points in t_2 and t_1 respectively, and each 2D slice represents the signal average of 32 scans. Each Y-slice for both the thiol signals and ferrocene was individually fit to Gaussian line-shapes.

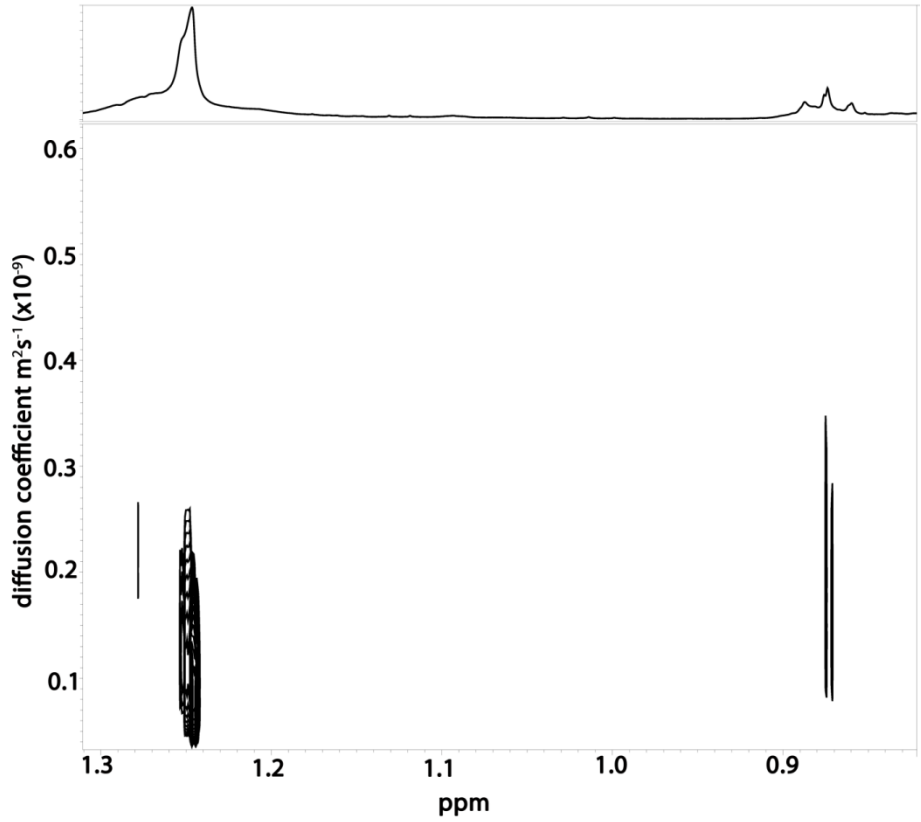

Figure 7.8. 2D DOSY NMR spectrum of large C_{12}-Au nanoparticles expanded to show the thiol signals in chloroform. Each of run was 32768 and 32 points in t_2 and t_1 respectively, and each 2D slice represents the signal average of 32 scans. Each Y-slice for both the thiol signals and ferrocene was individually fit to Gaussian line-shapes.

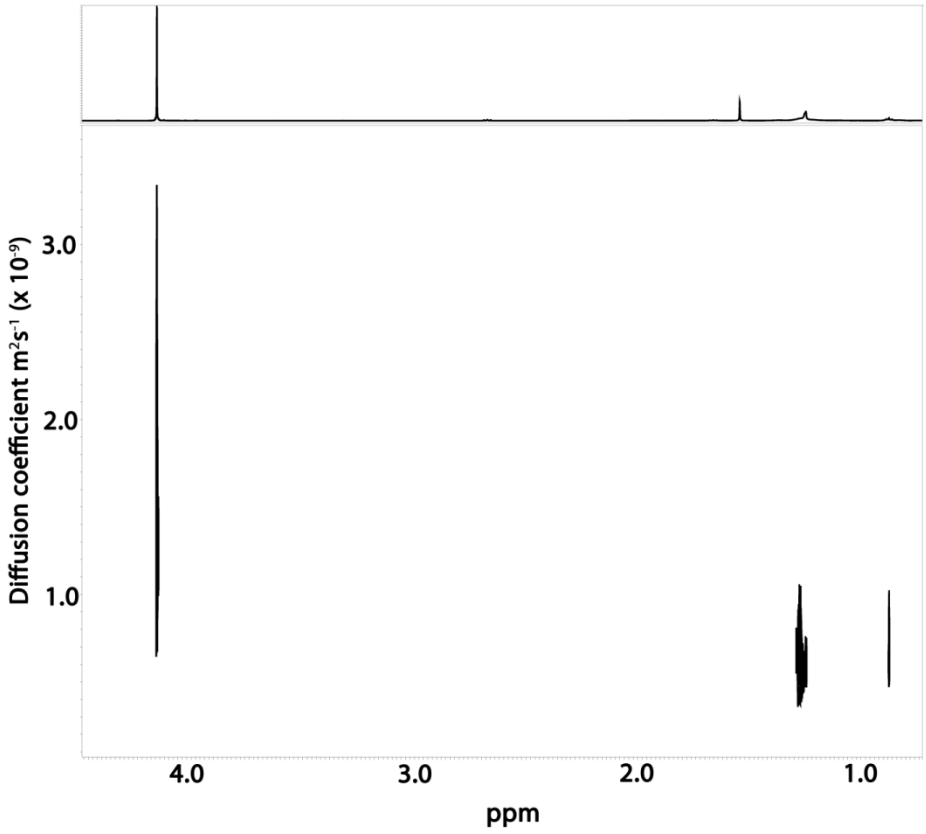

Figure 7.9. 2D DOSY NMR spectrum of small (2-3 nm) C_{12}-Au nanoparticles in chloroform. Each of run was 32768 and 32 points in t_2 and t_1 respectively, and each 2D slice represents the signal average of 32 scans. Each Y-slice for both the thiol signals and ferrocene was individually fit to Gaussian line-shapes.

The Gaussian fits to the data for the C_8-Au nanoparticles and ferrocene yield R^2 values of 0.99, and the fit to the data acquired on C_{12}-Au nanoparticles yields an R^2 value of 0.97. This good, but slightly lower R^2 value for the C_{12}-Au nanoparticles arises from the skewing of the left side of the trace shown in Figure 7.10. The data were re-acquired on a sample that did not contain ferrocene and the acquisition parameters, diffusion time specifically, were optimized and no skewing was observed.

Table 7.1. Results and error obtained from Gaussian curve fits of the projections obtained from DOSY experiments.

	Center	R^2	Area	Width	Error
C_{12}-Au NPs	$7.98x10^{-11}$	0.97	$3.74x10^{-7}$	$3.45x10^{-11}$	$\pm1.83x10^{-11}$
C_8-Au NPs	$4.74x10^{-10}$	0.99	$7.55x10^{-7}$	$8.12x10^{-11}$	$\pm6.55x10^{-11}$
Ferrocene	$1.39x10^{-9}$	0.99	$4.49x10^{-6}$	$3.57x10^{-10}$	$\pm1.49x10^{-11}$

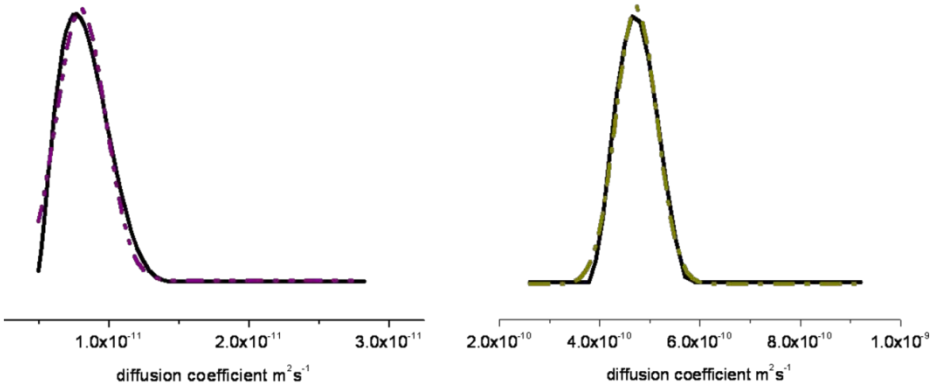

Figure 7.10. Gaussian curve fit (dotted lines) of f_1 slices (solid lines) for C_{12} (left) and C_8 (right) capped nanoparticles obtained from DOSY NMR data taken at 1.26 ppm.

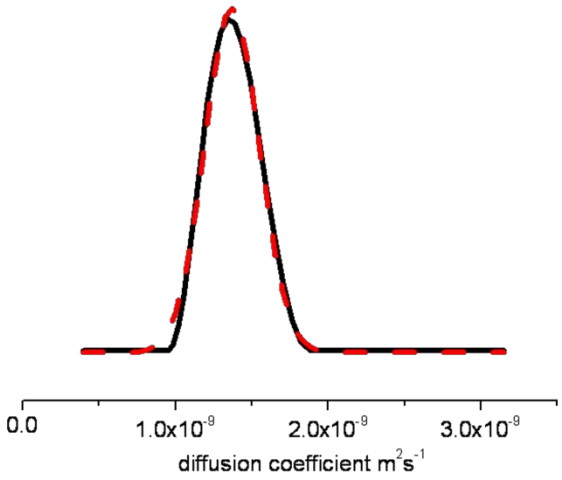

Figure 7.11. Gaussian curve fit (dotted line) of an f_1 data slice (solid line) for ferrocene in dichloromethane obtained from DOSY NMR data taken at 4.16 ppm.

Table 7.1 shows the DOSY diffusion coefficients, curve parameters, and fit R values used to establish sizes for the nanoparticles. As can be visually observed in the DOSY NMR data, the fit results in Table 7.1 show that the diffusion rates measured for samples of C_{12} (large) and C_8 nanoparticles are significantly different.

The diffusion coefficients obtained for ferrocene using DOSY NMR agree with previously reported diffusion coefficients of 1.4 x 10^{-9} m^2s^{-1} at 295.15 K in dichloromethane.[28] The diffusion coefficient of ferrocene in acetonitrile is reported as 2.24 x 10^{-9} m^2s^{-1} [20], which reflects the lower viscosity compared to dichloromethane [0.3409 x 10^{-3}Pa·s.[21]] This is consistent with the diffusion coefficient trend observed in the three solvents used in this study, as diffusion is expected to be slower in more viscous solvents. In summary, the results in Table 7.3 show that DOSY NMR gives sizes of Au NPs that are in excellent agreement with

TEM measurements on the same samples. Further, the sizes estimated by DOSY correspond to the sizes of the Au metal cores, irrespective of the alkane chain length of the attached alkane thiol shell.

Table 7.2. Diffusion coefficients [10^{-9} m^2s^{-1}] for Au NPs obtained from the DOSY NMR data for the three solvents used in the study. Error associated with each value is presented in parentheses. The diffusion coefficients represent an average of five separate experimental runs under the same conditions. The accuracy of determined coefficients from DOSY NMR were estimated using an average of the errors obtained from Gaussian curve fits.

	Benzene	Chloroform	Dichloromethane
Ferrocene	1.54(2)	1.62(2)	1.42(2)
C_{12}-Au NPs (large)	0.18(3)	0.20(2)	0.17(2)
C_8-Au NPs	0.37(7)	0.40(5)	0.35(7)
C_{12}-Au NPs (small)	N/A	0.45(6)	0.43(6)

Table 7.3. Au nanoparticle size in TEM images (in nm) and calculated from DOSY experiments using Eq. 3. DOSY calculated values were an average of five separate trials under identical conditions. Error associated with each value is presented in parentheses.

	TEM		DOSY	
	Size avg.	Benzene	Chloroform	Dichloromethane
C_{12}-Au NPs (large)	4.7(3)	5.1(4)	4.6 (3)	5.0 (4)
C_8-Au NPs	2.7(2)	2.5 (1)	2.4 (1)	2.5 (1)
C_{12}-Au NPs (small)	2.2(2)	N/A	2.2(2)	2.0(2)

7.3 Conclusions.

The results show the effectiveness of DOSY as an alternative to TEM for determining nanoparticle sizes. Size estimates can be obtained that agree with TEM image analysis by using diffusion coefficient ratios obtained from the proton signals from the alkyl thiolate groups bound to Au NPs and a ferrocene internal standard. The resulting diffusion coefficients were used to obtain hydrodynamic radii of Au nanoparticles. TEM images and DOSY results are in good agreement in varying solvents, showing the broad capability of this method. The DOSY NMR method presented here is a reliable alternative for obtaining nanoparticle sizes which is faster, and cost-effective compared to TEM. We expect that the DOSY method can be used to determine the sizes of a broad range of nanoparticles, including II-VI quantum dots, TiO_2, and metallic clusters; and that different nuclei, e.g. ^{29}Si, ^{31}P, ^{195}Pt, will prove to be useful for different applications.

7.4 Experimental

Nanoparticle synthesis

The alkanethiol protected nanoparticles were synthesized using the Schiffrin-Brust method. Sizes were controlled by varying reaction times. 0.595g of $HAuCl_4$ were dissolved in water (30mL, 0.03M) and mixed with the phase transfer reagent teraoctylammonium bromide (80mL, 0.05M) in toluene. The solution is stirred until all the gold is transferred to the organic phase, and the desired alkanethiol (150mg) is then added dropwise to the organic phase. After stirring, the

solution turns colorless, indicating that the Au-S polymer has formed. An aqueous $NaBH_4$ (25mL, 0.4M) solution is then added dropwise while stirring. The solution is then stirred for an additional 12hrs. For the smaller C_{12} particles, the solution is allowed to stir for about 3-6 hours, rather than 12. The solvent is evaporated to 10mL. Ethanol (400mL) is added to induce precipitation of the product. The solution is placed in a freezer overnight to aid the precipitation. The particles are then filtered over a fine porosity glass filter, washed copiously with about 500 mL of ethanol, dissolved in about 10mL of toluene and then reprecipitated. Washing extensively with ethanol ensures the complete removal of any unbound thiol, and also aids the removal of tetraoctylammonium bromide, the phase transfer reagent used during the synthesis. The product is then collected by dissolution in chloroform. It is imperative to use fresh nanoparticles as the UV-vis spectra suggest aggregation occurs. A distinct change in the plasmon resonance band is indicative of this aggregation. The band intensifies with the growing size of the nanoparticles. Therefore nanoparticles were disposed of after one month to preserve the integrity of these studies.

TEM imaging

TEM images were taken using a FEI Tecnai G2 Sphera equipped with a LaB_6 filament operating at an accelerating voltage of 200kV. Images were taken with a GatanUltrascan 1000 UHS CCD camera designed for a 200kV electron source. The camera has a 4 mega-pixel, Peltier cooled CCD chip and is equipped with an ultra-high sensitivity phosphor scintillator. The samples were prepared by

evaporating 3.5μL of a dilute $CHCl_3$ solution onto a 3x3 mm carbon coated copper grid. Images were analyzed using Image J software, available through the NIH.

NMR sample preparation and acquisition

NMR samples were prepared by vacuum drying 10-15mL of the Au nanoparticle solution, adding 1mL of the preferred deuterated solvent, and then transferring the solution to a 5 mm NMR tube. Approximately 0.2 mg of ferrocene was then added as an internal diffusion coefficient reference. All data were acquired using a JEOL ECA 500 MHz spectrometer equipped with an inverse-geometry broadband NMR probe and processed using JEOL's native Delta software. In preparation for acquisition, the probe was tuned and the 90° pulse time was calibrated for each diffusion measurement. Typical 90° pulse times were found to be between 10 and 13 us, and a 5 s pulse recycle delay was used on all experiments. The DOSY data shown were acquired with 32768 and 32 points in t_2 and t_1 respectively, and each 2D slice represents the signal average of 32 scans. Several different processing methods were used to deconvolute the exponential decays in the acquired DOSY data sets. The final results are reported using the CONTIN algorithm available in Delta.[26] The final, processed diffusion data were then fit using a Gaussian fit algorithm available in Origin. The reported error is expressed at the 95% confidence limit (2σ) from the obtained fits.

Note: Much of the material for this chapter comes directly from a manuscript entitled "Diffusion-Ordered NMR Spectroscopy as a Reliable Alternative to TEM for Determining the size of Gold Nanoparticles in Organic Solution" by Gabriele Canzi, Anthony A. Mrse, and Clifford P. Kubiak, which has been published in *Journal of Physical Chemistry C,* **2011**, *115* (16), 7972-7978. The dissertation author is the primary author of this manuscript.

7.5 References

(1) Pregosin, P. S.; Kumar, P. G. A.; Fernández, I. *Chemical Reviews* **2005**, *105*, 2977.

(2) Daniel, M.-C.; Astruc, D. *Chemical Reviews* **2003**, *104*, 293.

(3) Hu, M.; Chen, J.; Li, Z.-Y.; Au, L.; Hartland, G. V.; Li, X.; Marquez, M.; Xia, Y. *Chemical Society Reviews* **2006**, *35*, 1084.

(4) Sardar, R.; Funston, A. M.; Mulvaney, P.; Murray, R. W. *Langmuir* **2009**, *25*, 13840.

(5) Thomas, K. G.; Kamat, P. V. *Accounts of Chemical Research* **2003**, *36*, 888.

(6) Brust, M.; Walker, M.; Bethell, D.; Schiffrin, D. J.; Whyman, R. *J Chem Soc Chem Comm* **1994**, 801.

(7) Marega, R.; Aroulmoji, V.; Bergamin, M.; Feruglio, L.; Dinon, F.; Bianco, A.; Murano, E.; Prato, M. *ACS Nano* **2010**, *4*, 2051.

(8) Van Lokeren, L.; Maheut, G.; Ribot, F.; Escax, V.; Verbruggen, I.; Sanchez, C.; Martins, J. C.; Biesemans, M.; Willem, R. *Chemistry – A European Journal* **2007**, *13*, 6957.

(9) Kohlmann, O.; Steinmetz, W. E.; Mao, X.-A.; Wuelfing, W. P.; Templeton, A. C.; Murray, R. W.; Johnson, C. S. *The Journal of Physical Chemistry B* **2001**, *105*, 8801.

(10) Barjat, H.; Morris, G. A.; Smart, S.; Swanson, A. G.; Williams, S. C. R. *Journal of Magnetic Resonance, Series B* **1995**, *108*, 170.

(11) Cohen, Y.; Avram, L.; Frish, L. *Angewandte Chemie International Edition* **2005**, *44*, 520.

(12) Delsuc, M. A.; Malliavin, T. E. *Analytical Chemistry* **1998**, *70*, 2146.

(13) Kapur, G. S.; Findeisen, M.; Berger, S. *Fuel* **2000**, *79*, 1347.

(14) Morris, K. F.; Johnson, C. S. *Journal of the American Chemical Society* **1993**, *115*, 4291.

(15) Gomez, M. V.; Guerra, J.; Myers, V. S.; Crooks, R. M.; Velders, A. H. *Journal of the American Chemical Society* **2009**, *131*, 14634.

(16) Lica, G. C.; Zelakiewicz, B. S.; Tong, Y. Y. *Journal of Electroanalytical Chemistry* **2003**, *554–555*, 127.

(17) Link, S.; El-Sayed, M. A. *The Journal of Physical Chemistry B* **1999**, *103*, 4212.

(18) Xu, X.-H. N.; Huang, S.; Brownlow, W.; Salaita, K.; Jeffers, R. B. *The Journal of Physical Chemistry B* **2004**, *108*, 15543.

(19) Lee, K.-C.; Lin, S.-J.; Lin, C.-H.; Tsai, C.-S.; Lu, Y.-J. *Surface and Coatings Technology* **2008**, *202*, 5339.

(20) Bond, A. M.; Henderson, T. L. E.; Mann, D. R.; Mann, T. F.; Thormann, W.; Zoski, C. G. *Analytical Chemistry* **1988**, *60*, 1878.

(21) Reichardt, C. *Solvent Effects in Organic Chemistry*; Verlag Chemie: Weinheim: New York, 1979.

(22) D. Canet, M. D. *Dynamics of Solutions and Fluid Mixtures by NMR*; Wiley: Chichester, 1995.

(23) Zuccaccia, D.; Macchioni, A. *Organometallics* **2005**, *24*, 3476.

(24) Garcia de la Torre, J.; Navarro, S.; Lopez Martinez, M. C.; Diaz, F. G.; Lopez Cascales, J. J. *Biophysical Journal* **1994**, *67*, 530.

(25) Bond, A. M.; Colton, R.; Harvey, J.; Hutton, R. S. *Journal of Electroanalytical Chemistry* **1997**, *426*, 145.

(26) Provencher, S. W. *Computer Physics Communications* **1982**, *27*, 229.

(27) Huo, R.; Wehrens, R.; Duynhoven, J. v.; Buydens, L. M. C. *Analytica Chimica Acta* **2003**, *490*, 231.

(28) Kadish, K. M.; Ding, J. Q.; Malinski, T. *Analytical Chemistry* **1984**, *56*, 1741.